Visualization, Kinetics, and Thermodynamics of DNA–Protein Interactions

Dissertation

for the award of the academic degree of
Doctor of Natural Science
– Dr. rer. nat. –

from the faculty of Biology, Chemistry and Geosciences
University of Bayreuth

submitted by
Frank Schubert
born in Paderborn

Bayreuth, 2005

Visualization, Kinetics, and Thermodynamics of DNA–Protein Interactions

Dissertation

zur Erlangung des akademischen Grades eines
Doktors der Naturwissenschaften
– Dr. rer. nat. –

der Fakultät für Biologie, Chemie und Geowissenschaften
der Universität Bayreuth

vorgelegt von
Frank Schubert
aus Paderborn

Bayreuth, 2005

Die vorliegende Arbeit wurde in der Zeit von September 2001 bis April 2005 am Lehrstuhl für Physikalische Chemie der Universität Bayreuth in der Arbeitsgruppe von Herrn Prof. Dr. Georg Krausch angefertigt.

Vollständiger Abdruck der von der Fakultät für Biologie, Chemie und Geowissenschaften der Universität Bayreuth genehmigten Dissertation zur Erlangung des akademischen Grades eines Doktors der Naturwissenschaften (Dr. rer. nat.).

Datum der Einreichung:	13. April 2005
Datum des wissenschaftlichen Kolloquiums:	25. Juli 2005

Prüfungsausschuss:

Prof. Dr. Georg Krausch (Erstgutachter)

Prof. Dr. Franz Xaver Schmid (Zweitgutachter)

Prof. Dr. Helmut G. Alt

Prof. Dr. Gerhard Krauss (Vorsitzender)

Meinen Eltern

Perché, secondo l'opinion mia,
A chi vuole una cosa ritrovare,
Bisogna adoperar la fantasia.

Galileo Galilei, *Contro il portar la toga*

Contents

Contents

List of Tables

List of Tables

List of Figures

List of Figures

List of Figures

List of Abbreviations

$[X]$	concentration of X
6-4PP	pyrimidine-(6-4)-pyrimidone photoproduct
A	adenine
A_{260}	absorbance at 260 nm
AFM	atomic force microscopy
AOTF	acoustooptical tunable filter
APD	avalanche photodiode
Ar	argon
bp	base pairs
C	cytosine
C	concentration
CEVS	controlled environmental vitrification system
CPD	cyclobutane pyrimidine dimers
cryo-TEM	cryogenic-transmission electron microscopy
CS	Cockayne' syndrome
D	diffusion coefficient
d	diameter
ΔC_p	heat capacity change
ΔG	Gibbs free energy
ΔH	reaction enthalpy
ΔS	reaction entropy
DNA	deoxyribonucleic acid
dNTP	mixture of oligonucleotides
DSC	differential scanning calorimetry
dsDNA	double-stranded DNA
DTT	1,4-Dithiothreitol
E_A	activation energy
E. coli	*Escherichia coli*
η	viscosity
$F(t)$	fluorescence fluctuation function
FCCS	fluorescence cross-correlation spectroscopy
FCS	fluorescence correlation spectroscopy

List of Abbreviations

G	guanine
$G(\tau)$	correlation function
HeNe-laser	helium-neon laser
ITC	isothermal titration calorimetry
K	number of different fluorescent particles
k	Boltzmann constant
K_D	equilibrium constant
k_a, k_d	association and dissociation rate constant
L	length
MCM	mini-chromosome maintenance protein
N	particle number
n	refractive index
NA	numerical aperture
NER	nucleotide excision repair
NIR	near-infrared radiation
nt	nucleotide
PCR	polymerase chain reaction
pH	$-\log[\mathrm{H}^+]$
ϕ_i	fraction of the ith component
PT100	temperature sensor based on platinum
R	gas constant
R_eq	equilibrium response
R_h	hydrodynamic radius
R_max	maximum binding capacity of the sensor chip
r_0	axial distance of the confocal volume
RPA	replication protein A
RU	response units
S	structure parameter
SAM	self-assembled monolayer
SDS	sodium dodecyl sulfate
SPR	surface plasmon resonance
ssDNA	single-stranded DNA
T	thymine
T	temperature
t	time
τ	lag time of the autocorrelation analysis
τ_D	diffusion time
TEM	transmission electron microscopy
θ	degree of binding
TIR	total internal reflection

UV	ultraviolet radiation
UVA	ultraviolet radiation in the 320-400 nm range
UVB	ultraviolet radiation in the 280-320 nm range
UVC	ultraviolet radiation in the 200-280 nm range
V_{eff}	effective confocal volume
XP	*Xeroderma Pigmentosum*
z_0	lateral distance of the confocal volume

List of Abbreviations

1 Introduction

Methods for the characterization of DNA–protein interactions are of great importance in the study of cellular processes, such as DNA replication and repair. Various methods have been developed so far for the detection of biomolecular interactions, all having certain advantages and disadvantages. Surface plasmon resonance (SPR) and fluorescence correlation spectroscopy (FCS) have emerged as a powerful alternative to classical biochemical methods for the characterization of ligand-receptor binding in biomolecular systems. A key advantage of the two methods, as compared to conventional methods, lies in the speed and simplicity of the analysis. Compared to classical thermodynamic methods like isothermal titration calorimetry (ITC) and differential scanning calorimetry (DSC), SPR and FCS only require smallest amounts of DNA and protein.

An interesting phenomenon concerning SPR and FCS is that the two methods often yield different values for the equilibrium constants. In order to explain this, one has to take a closer look at the thermodynamics of biomolecular interactions using SPR and FCS. In this work, SPR and FCS were used to systematically compare the kinetic and thermodynamic data obtained for the interaction between the human replication protein A (RPA) and single stranded DNA. This system is well characterized and therefore seems suitable for a comparative model study.

In order to complete the picture about the binding process of RPA to DNA, the interaction of the protein with dsDNA containing distinct damage sites was also investigated using FCS. The results show that RPA binds with high affinity to damaged DNA, but not to undamaged DNA. This fits nicely into the picture of RPA as a single-stranded DNA binding protein, which is important in the early steps of DNA repair.

FCS experiments were also performed in cross-correlation mode in order to monitor the hybridization kinetics of DNA. The hybridization kinetics strongly depends on the number of hydrogen bonds formed, using different ssDNA fragments therefore should give different kinetics. For the experiments three different ssDNA substrates were used, which form during hybridization a 'normal' dsDNA, a dsDNA containing a bulge defect, and a dsDNA containing a bubble defect. The formation of 'normal' dsDNA exhibits the fastest kinetics, whereas the kinetics of the two damaged dsDNA yield almost the same value. As a side effect, it was shown that the commercially available FCS system is not perfectly suited for cross-correlation analysis.

In addition to quantitative analysis by SPR and FCS, imaging experiments were performed using Atomic Force Microscopy (AFM) and cryogenic-Transmission Electron Microscopy (cryo-TEM) to obtain structural information about the interactions between RPA and dsDNA. One drawback of AFM is the immobilization of the biomolecules to a surface. The interaction with the surface leads to a loss of one degree of freedom, because the deposition onto a surface is a transition from three dimensions to two dimensions, which may lead to conformational changes. To avoid the influence of the surface onto the structure of the biomolecules, the same system was studied using cryo-TEM. Therefore, some of the AFM images taken by M. Lysetska [Lys04] are compared with the images taken in this work.

In a very last part, the interaction between DNA and mini-chromosome maintenance protein expressed by *Methanothermobacter thermoautotrophicum* (MthMCM), a protein essential in both the initiation and elongation phases of DNA replication, was investigated by FCS, AFM and cryo-TEM. Earlier studies revealed that the archaeal enzymes possess a robust and processive 3' to 5' helicase activity, a single- and double-stranded DNA binding function, and ATPase activity. The DNA binding process and the mechanism of the unwinding process are still not fully understood, so the MthMCM activity was followed using FCS, AFM, and cryo-TEM to gain

information about the structure, kinetics, and thermodynamics of this biomolecular interaction. This research project is still ongoing in order to gain more information about the mechanism of the DNA unwinding process.

1.1 Structure and Function of DNA

DNA (deoxyribonucleic acid) is in its primary structure a linear polymer composed of monomers called nucleotides. DNA exists in all eukaryotic and prokaryotic cells and functions to store the complete genetic information required to specify the structure of all the proteins of each species and organism, to program in time and space the orderly biosynthesis of the cell and tissue components, and to determine the individuality of a given organism.

DNA consists of four different nucleotides. All nucleotides contain three characteristic components: a phosphate group, linked by a phosphoester bond to a pentose, that in turn is linked to an organic base. DNA contains four different organic bases: cytosine (C), thymine (T) (pyrimidine bases), adenine (A), and guanine (G) (purine bases). Specific sequences of A, T, G, and C bases encode the genetic information. The successive nucleotides of the DNA are covalently linked to each other through phosphate-group bridges. The 5'-hydroxyl group of the pentose of one nucleotide unit is joined to the 3'-hydroxyl group of the pentose of the next nucleotide by a phosphodiester linkage. The covalent backbone of nucleic acid is highly polar, since the phosphate groups are acidic and are negatively charged at the pH of the cell. However, the organic bases, which are relatively insoluble in water, are hydrophobic. DNA strands have a specific polarity, or direction, because all the internucleotide phosphodiester linkages have the same orientation along the chain. Due to this polarity, each linear nucleic acid strand has a 5' end and a 3' end.

The double-helix secondary structure of the DNA was discovered by James Watson and Francis Crick in 1953 [Wat53], based on x-ray stud-

ies of the structure of DNA fibers. The three-dimensional model of the DNA structure consists of two helical DNA chains coiled around the same axis to form a right-handed double helix. In the helix, the two chains or strands are antiparallel, that is, their 5' to 3' directions are opposite. Their hydrophilic backbones are on the outside of the double-helix, facing the surrounding water, while the hydrophobic organic bases are stacked inside the double helix, so that the nearly planar bases molecules are very close together, and perpendicular to the long axis of the double-helix. The spatial relationship between these strands creates a major groove and a minor groove between the two DNA strands. The bases of one strand are paired in the same planes with the bases of the other strand. Only certain base-pairs fit precisely inside this structure. The allowed pairs are A-T and G-C, and few mismatches do not disturb the helical structure. The complementary bases of each pair form hydrogen bonds to each other, G and C form three hydrogen bonds, while A and T form two. Two main forces hold together the DNA double-helix: hydrogen bonding between complementary base pairs, and hydrophobic interactions, which cause the stacked bases to be largely hidden within the double helix. The usual DNA form found in cells, called the B-form DNA, is characterized by a helical turn every 10 base pairs (every 3.4 nm), vertically stacked bases that are 0.34 nm apart, and a helix diameter of 2 nm.

1.2 DNA Damage

DNA is a rather compact and stable molecule that can withstand a variety of external factors such as drying and low temperatures. However it is not fully inert and can be damaged by a wide range of physical and chemical agents both inside cells and from the environment. UV light and various chemicals can introduce changes in the bases and therefore structural changes within the helix might occur. This affects the function of the DNA and may induce genetic mutations and cell death [Alb03, Ber94, Ich03, Mit89].

1.2.1 UV-induced Damage

UV light is absorbed by the nucleic acid bases, and the resulting influx of energy can induce chemical changes. Photon absorption rapidly (10^{-12} s) converts a base to an excited state. Various pathways are then available for relaxation of this unstable electronic configuration [Wan76]. The major pathway involves rapid dissipation of the energy of the excited base to the ground state (10^{-9} s) by non-radiative transition or by fluorescence, yielding heat or light in the process. Secondly, the excited base can react with other molecules to form unstable intermediates (i.e. free radicals) or stable photoproducts. Finally, there is a low probability that intersystem crossing, a nonradiative pathway, can transfer a base from the excited singlet state to the excited triplet state. The lifetime of the triplet state is several orders of magnitude longer than the excited singlet state (10^{-3} s), increasing the chance of photoproduct formation.

The most frequent photoproducts are cyclobutane pyrimidine dimers (CPD) [Beu60], pyrimidine(6-4)pyrimidone photoproducts (6-4PP) [Lip81, Ryc85], 8,8-adenine dehydrodimers [Gas86], purine photoproducts [Gal89], and photoproducts at A-T sequences [Bos84]. Dimerizations between adjacent pyrimidine bases (CPD and 6-4PP) are by far the most prevalent photoreactions resulting from UVC irradiation of DNA. They form $\sim 95\,\%$ of the DNA UV-damage and are a major source of mutations and cancer [Bou87, Bra88, Cle88, Mit89, Smi93, Spi88].

In contrast to the direct induction of DNA damage by UVC and UVB light, UVA produces damage indirectly through highly reactive chemical intermediates. Similar to ionizing radiation, UVA radiation generates oxygen and hydroxyl radicals by the UV absorption of water [Fol02, Hor01], which in turn react with DNA to form monomeric photoproducts, such as cytosine and thymine photohydrates, as well as strand breaks and cross-links [Cad92].

The damage induced by UV light is distributed irregularly along the DNA chain. At some sites they occur very often (hotspots), while at

other sites they never arise (cold spots) [Ben61, Par94]. The occurrence of a DNA lesion depends on two parameters: the sequence of the DNA in the vicinity of the photoproduct, and the flexibility at the site of the photoproduct [Bec89, Kim95, Tay90].

The relationship between the relative occurrence of all these photoproducts and their biological effect depends on the cytotoxic and mutagenic potential of the individual lesion. Hence, even though a photoproduct may occur at a low frequency, its structure and location may elicit a potent biological effect.

1.3 DNA Repair

DNA damage can be induced by replication errors or by physical and chemical processes both from inside a cell and from the environment. The cell itself has developed different mechanisms for recognition and repairing the damage. The failure of this processes leads to serious diseases like Xeroderma Pigmentosum and Cockayne' syndrome [Boo98]. Moreover most of the human cancer might result from from unrepaired DNA damage [Sar97].

1.3.1 Nucleotide Excision Repair

The importance of Nucleotide Excision Repair (NER) for human health is illustrated by the occurrence of rare autosomal recessive disorder Xeroderma Pigmentosum (XP). Patients characteristically show severe photosensitivity and abnormal pigmentation, often accompanied by mental retardation, and they usually develop skin cancer at very young age [Boo98]. Cells from these patients are also extremely sensitive to UV light and have a defect in NER. Complementation studies revealed that eight genes are involved in XP: XPA through XPG and XPV (XP-Variant). Mutations in the XP genes (except XP-variant) lead to defective NER and hypersensitivity to UV. In addition to XP, other UV sensitive syndromes exist.

Cockayne' syndrome (CS) is a rare disorder that is associated with a wide variety of clinical symptoms. Beside other symptoms, the patients generally show dwarfism, mental retardation and photosensitivity. In contrast to XP, CS is not associated with an enhanced incidence of skin cancer. Cells from CS patients are hypersensitive to the cytotoxic effects of UV and are characterized by the inability to resume UV inhibited DNA and RNA synthesis. The progressive neurological abnormalities associated with CS may be due to the inability of CS cells to repair oxidative DNA lesions [LP00]. PIBIDS (the acronym of the characteristic clinical symptoms of the patients for Photosensitivity, Ichthyosis, Brittle hair, Impaired intelligence, Decreased fertility and Short stature) is a photosensitive variant of Trichothiodystrophy (TTD) and the third syndrome that can be associated with NER defects [Iti01]. Certain mutations in the XPB and XPD genes have been shown to cause the PIBIDS phenotype, but not in combination with the specific XP characteristics like cancer proneness.

NER is a complex process which can be separated in the following steps (see figure 1.1):

1. Damage recognition
2. Binding of a multi-protein complex at the damaged site
3. Double incision of the damaged strand several nucleotides away from the damaged site, on both the 5' and 3' sides
4. removal of the damage-containing oligonucleotide
5. Filling in of the resulting gap by a DNA polymerase
6. Ligation

The initial step of the damage recognition is a rate-limiting step and involves certain proteins: XPC-hHR23B, XPA, RPA, and TFIIH [Bat00, Lee00, San96, Woo00]. It has been shown that all these proteins show a higher affinity to damaged DNA in comparison to undamaged DNA.

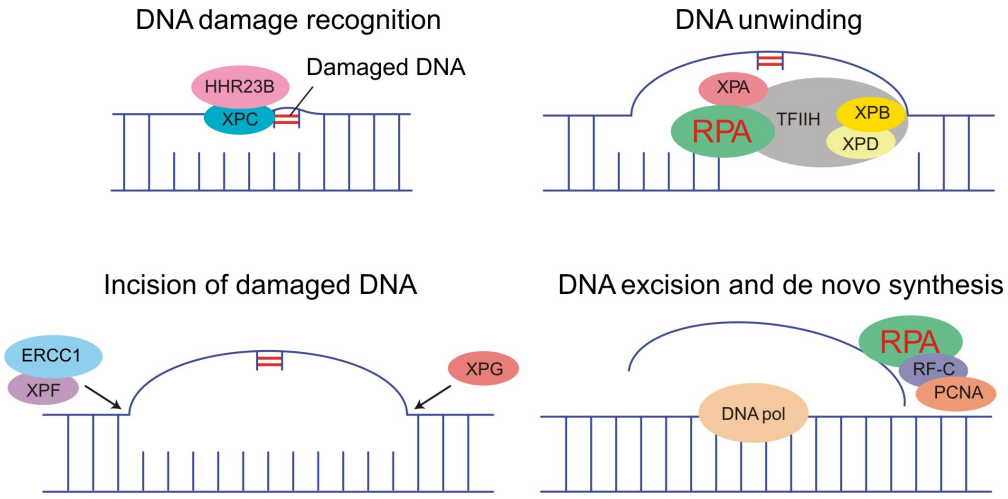

Figure 1.1: Pathway of NER. In the first step, the protein complex XPC / HHR23B binds to the damaged DNA site, recruiting the entire repair protein apparatus to the injury. In the second step, DNA unwinding, the lesions are opened by the concerted action of XPA, RPA, and the bi-directional XPB / XPD helicase subunits of the transcription factor IIH (TFIIH) complex. During incision of the damaged DNA, the exchange repair cross complementing (ERCC1) / XPF complex cuts at the single-strand to double-strand transition on the 5' side of the damage, and XPG cuts at the 3' side of the open complex. Finally, DNA excision and de novo synthesis is accomplished by mammalian DNA replication factors such as RPA, replication factor C (RF-C), proliferating cell nuclear antigen (PCNA), and DNA polymerase [Mat02].

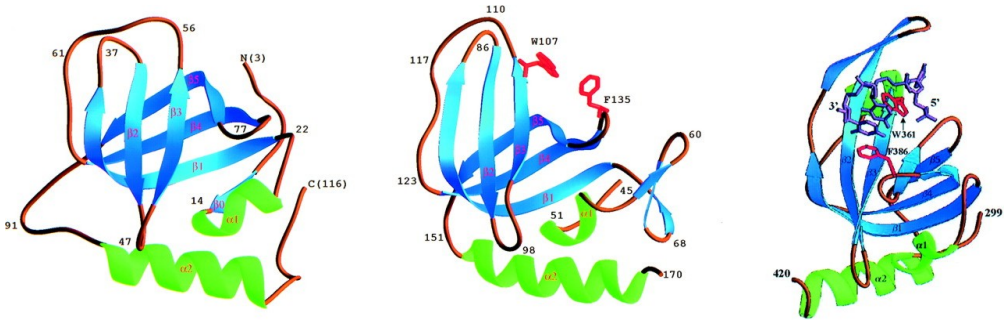

Figure 1.2: Structure of the three subunits of RPA obtained by X-ray crystallography. From left to right are shown the subunits of 14, 32, and 70 kDa [Boc97].

The fact that the NER proteins recognize a variety of DNA lesions suggest that they detect structural distortions, e.g. helix bending, unwinding, or unpaired regions induced by changes in the chemistry of the bases [Bel90, Gun96, Hus88, Tho03, Vas02]. Although many details of this process have been revealed, the mechanisms of DNA damage recognition are still not fully understood [Tho03, You03].

1.3.2 Replication Protein A

Replication protein A (RPA) is a heterotrimeric protein containing subunits of 70, 32 and 14 kDa. The structure of the three subunits has been obtained by NMR and X-ray crystallography (figure 1.2) [Boc97, Boc02, Bri98, Phi96]. RPA is involved in replication and recombination processes and participates in the regulation of transcription [Lao99, Wol97]. An essential role of RPA has been demonstrated for nucleotide excision repair (NER), a pathway which removes a variety of major DNA lesions including photoproducts, adducts of carcinogens and cisplatin [Bur96, Woo99, Pat99, Lao00].

By its DNA binding properties, RPA can be classified as single-stranded DNA binding protein. It binds with high affinity and low sequence specificity to single-stranded DNA [Mit93, Kim94]. DNA binding domains have been identified on the 70 and 32 kDa subunits of RPA, although

most of the DNA contacts appear to be mediated by the 70 kDa subunit. Furthermore, X-ray crystallography of a complex between a fragment of the 70 kDa subunit and $(dC)_8$ has revealed details of the binding site for single-stranded DNA. The DNA is bound in a shallow groove containing several aromatic residues and a surplus of positive charges [Boc97]. Its apparent association constant to ssDNA of 10^9–10^{11} $^1/_M$ is at least three order of magnitude higher than the one to dsDNA. Binding of RPA to ssDNA proceeds in three steps: Initial weak interaction occurs with the 8-10 nt of the 5'-end of ssDNA [Bla94, Kol01]. This is followed by an intermediate 13-14 nt binding step, and finally a more stable binding mode occurs, in which the RPA covers up to 30 nt [Kim92, Kim94, Lav99]. As a consequence of the binding process, the RPA undergoes conformational changes [Gom96, Bla96, Boc01]. This changes can be explained by the participation of RPA trimerization core in DNA binding [Boc01, Boc02].

Transmission electron microscopy experiments have shown that RPA unwinds long regions of linear dsDNA [Eck01, Tre96]. It is suggested that after an initial binding of protein a separation of adjacent base pairs is induced. Moreover it was found that the RPA does not bind at random sites, but preferentially at the end of a dsDNA strand. At low protein concentrations only terminal binding of RPA to linear dsDNA was observed.

A high affinity of RPA to dsDNA lesion suggests that RPA participates in the damage recognition step in NER [Bur96, He95, Hey01, Lao00, Pat99, Woo99]. Its affinity for damaged sites on double-stranded DNA is by more than one order of magnitude higher than for undamaged double-stranded DNA [Hey01]. Cross-linking experiments have identified a binding site for damaged DNA on the 70 kDa subunit [Sch99]. Since the chemical nature of the DNA lesions recognized by RPA is diverse, it is believed that RPA binds to unpaired regions created at the sites of DNA damage.

Additionally, RPA seems to be crucial for the coordination of NER proteins. Interactions of RPA were demonstrated with XPG [Bes97, dL98, He95, Mat96], DNA polymerase [Bra97], and XPA [He95, Mat95]. RPA and XPA have a cooperativity in binding to dsDNA containing photole-

sions [Wan00].

1.4 Mini-Chromosome Maintenance

The eukaryotic mini-chromosome maintenance (MCM) complex consists of six paralog proteins (MCM2–7) that belong to the AAA$^+$ (ATPases with other associated cellular activities) superfamily [Tye99, For04, Neu99]. The *Saccharomyces cerevisiae* MCM genes were all shown to be essential in both the initiation and elongation phases of DNA replication [Lab00]. MCM genes were also identified in other eukaryotic organisms (such as *Schizosaccharomyces pombe*, *Drosophila melanogaster*, *Xenopus laevis*, and *Homo sapiens*), and in several cases the corresponding protein products were purified from cell extracts of the above species as complexes of variable subunit composition (such as MCM2 / 3 / 4 / 5 / 6 / 7, MCM2 / 4 / 6 / 7, MCM4 / 6 / 7, and MCM3 / 5) [Thö97, You99, Lee00a]. Among all of these multimeric assemblies, a hexamer comprising the subunits MCM4, MCM6, and MCM7 of *H. sapiens* [Ish97], *Mus musculus* [You99], and *S. pombe* [Lee00a, Lee01] displayed a weak DNA helicase activity *in vitro*, whereas MCM2 and MCM3 / 5 caused the disassembly of the pre-formed MCM4 / 6 / 7 hexamers and inhibited the helicase activity [You99, Lee00a, Ish97, Sat00, Ish98]. This led to the suggestion that the complex is formed by three active subunits (MCM4, MCM6, and MCM7) and three subunits with a regulatory role (MCM2, MCM3, and MCM5). However, site-directed mutagenesis studies indicated that physical association between specific proteins of the two groups is required for efficient ATPase activity [Sch01, Dav03].

Despite a number of studies suggesting that in eukaryotic organisms the MCM complex could act as the replicative DNA helicase, some concern was caused by the limited processivity of its DNA unwinding activity *in vitro*. The most direct piece of evidence that the MCM complex possesses DNA helicase activity comes from studies of the homologous proteins from Archaea. Whereas eukaryotes possess six paralogs, most archaeal species

examined contain a single MCM homologue [Kel03, Gra03]. To date, the MCM-like complex has been characterized only from three archaeal organisms, namely *Methanothermobacter thermoautotrophicum* (MthMCM) [Kel99, She00, Pop01, Shi03, Kas04], *Sulfolobus solfataricus* (SsoMCM) [Car02], and *Archaeoglobus fulgidus* (AfuMCM) [Gra03a]. These studies revealed that the archaeal enzymes possess a robust and processive 3' to 5' helicase activity, a single- and double-stranded DNA binding function, and ATPase activity. A three-dimensional reconstruction of the full sized MthMCM structure by electron microscopy is shown in figure 1.3 [Pap03]. It was reported that the *S. pombe* MCM4 / 6 / 7 complex is significantly stimulated on forked DNA structures and can unwind duplex molecules up to $\sim$ 600 base pairs on 5'-tailed substrates [Lee01].

The oligomeric structure of the archaeal MCM complex is still not clear. Whereas the MthMCM produced in *Escherichia coli* was reported to form dodecamers [Kel99, Cho00, She00, Pop01], the recombinant SsoMCM [Car02] and *A. fulgidus* MCM [Gra03a] were both shown to behave as homo-hexamers in solutions. Electron microscopy analyses of MthMCM revealed ring-shaped hexameric [Pap03] or heptameric [Yu02] assemblies. A toroidal hexameric structure was also observed for the MCM4 / 6 / 7 [Sat00] and MCM2 / 4 / 6 / 7 [Yab03] complexes purified from HeLa cells. On the other hand, the crystallographic structure of the MthMCM N-terminal portion revealed a dodecameric architecture, with two hexameric rings juxtaposed in a head-to-head configuration [Fle03]. A remarkable feature of this structure is the presence of a long central channel whose surface has a considerably high positive charge. A three-dimensional reconstruction of the full sized MthMCM structure by electron microscopy suggests that this central channel runs throughout the entire MthMCM molecule [Pap03]. The diameter of the positively charged channel (ranging from 2.5 to 4.5 nm) is large enough to accommodate DNA molecules in either single- or double-stranded form [Pap03, Fle03].

Amino acid residues of the SsoMCM protein responsible for binding / remodelling DNA were identified. Structure-aided alignment of MthMCM

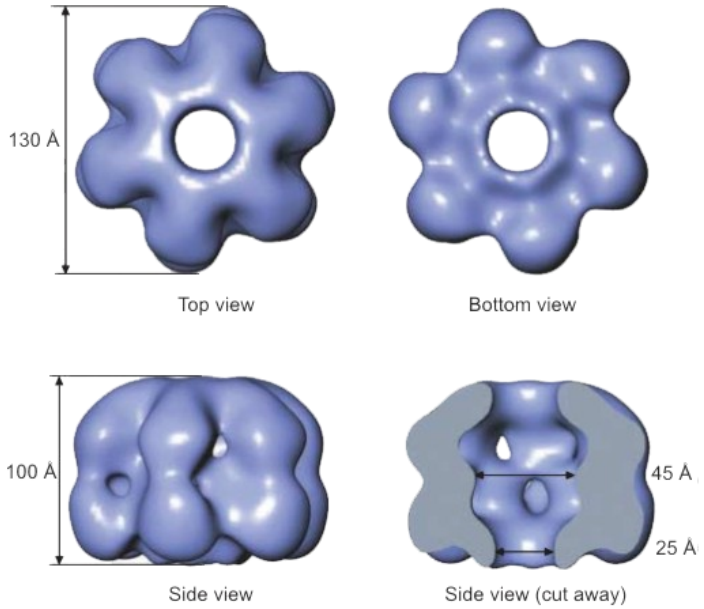

Figure 1.3: Three-dimensional reconstruction of MthMCM at 23 Å resolution. A surface representation obtained from the three-dimensional reconstruction of the MthMCM complex is shown in different orientations. The protein monomers assemble into a hexameric ring around a wide central channel, with a clear asymmetry between the top and bottom views. A side view reveals the large central chamber and the channel spanning the entire length of the molecule [Pap03].

and SsoMCM sequences revealed four positively charged amino acids (Lys-129, Lys-134, His-146, and Lys-194) of the SsoMCM protein potentially pointing to the center of the putative DNA binding channel [Puc04]. It was found that all of the above SsoMCM amino acids participate in DNA binding, and the substitution of Lys-134 to alanine was found to affect only binding to duplex molecules, whereas single-stranded DNA binding and helicase activity were not impaired.

2 Materials and Methods

2.1 Materials

2.1.1 Oligonucleotides and DNA

Biotinylated oligonucleotides were purchased from Interactiva (Ulm, Germany), Cy5-labelled ssDNA from MWG-Biotech (Ebersberg, Germany), and oligonucleotides with Alexa488, DY635 and Atto647 labels from IBA (Göttingen, Germany). The sequences of the different oligonucleotides are given in table 2.1, the labels are attached to the 5'-end. The oligonucleotides Simple, Bulge, Bubble, and Bottom were used for hybridization experiments and form the dsDNA fragments shown in figure 2.1. The dsDNA fragments formed by hybridization were also used for the interaction studies with RPA. Table 2.2 gives a listing of dsDNA fragments used in AFM and cryo-TEM experiments.

2.1.2 Proteins

The proteins used in all parts of this work and their sources are listed in table 2.3.

2.2 Methods

2.2.1 Hybridization of Oligonucleotides

The short dsDNA fragments for FCS experiments were obtained by hybridization of synthetic oligonucleotides. Equimolar solutions of complementary ssDNA strands were mixed in an Eppendorf tube and heated in

Table 2.1: List of oligonucleotides used in SPR and FCS experiments. All labels are attached to the 5'-end.

Name	Sequence	Label
15-mer	5'-AAG-TAT-TAT-AAT-CAC-3'	Biotin
26-mer	5'-AAG-TAT-TAT-AAT-CAC-TAA-ATA-CGA-AA-3'	Biotin, Cy5
Simple	5'-CCG-AAT-TCC-CGG-GGA-GAA-GAA-GAG-TGC-ACA-GAA-GAA-GAG-GCC-CGG-GCG-ACC-TGC-AGG-C-3'	DY635, Atto647
Bulge	5'-CCG-AAT-TCC-CGG-GGA-GAA-GAC-AGA-AGA-AGA-GGC-CCG-GGC-GAC-CTG-CAG-GC-3'	DY635, Atto647
Bubble	5'-CCG-AAT-TCC-CGG-GGA-GAA-GAT-CTC-ACG-TCA-GAA-GAA-GAG-GCC-CGG-GCG-ACC-TGC-AGG-C-3'	DY635, Atto647
Bottom	5'-GCC-TGC-AGG-TCG-CCC-GGG-CCT-CTT-CTT-CTG-TGC-ACT-CTT-CTT-CTC-CCC-GGG-AAT-TCG-G-3'	Alexa488

Figure 2.1: Short dsDNA fragments used in FCS experiments.

Table 2.2: List of DNA fragments used in AFM and cryo-TEM experiments.

Name	Synthesis
538 bp	generated by PCR (2.2.2) using plasmid pUC-pRN1 [Kee96] as a template and the following primers: 5'-CGC-CAC-TTG-GCG-AGA-AAT-TTG-CTC-AAA-G-3' as forward primer and 5'-GGT-TGA-GCT-CGA-GTC-ACA-GGA-GTT-CGT-CAC-GGC-3' as reversed primer.
1574 bp	generated by PCR (2.2.2) using Sulfolobus solfataricus P2 genomic DNA as a template and the following primers: 5'-CCC-CCC-GCT-AGC-CCA-TGG-TTG-AAG-TTG-AGG-CTA-AGG-A-3' as forward primer and 5'-CCC-CGA-ATT-CAA-TAC-ACA-CCA-CCT-ATT-TCA-C-3' as reversed primer.
λ-DNA	purchased from New England BioLabs (N3011). The λ-DNA is 48502 bp in length.

Table 2.3: List of proteins used.

Name	Synthesis
RPA	expressed in *E. coli* BL21 (DE3) using the expression vector pET11d-thRPA (M. S. Wold, University of Iowa) and purified by T. Hey [Hey02]
MCM	expressed in *E. coli* using the expression vector pET-MCM (S. Bell, Hutchison/MRC Research Centre, Cambridge) and purified by G. Lipps

a water bath to 100 °C and then slowly cooled down to room temperature. Fragments with one fluorescent label were obtained by hybridization of the labelled oligonucleotide with a slight excess of the complementary oligonucleotide.

2.2.2 Polymerase Chain Reaction: Amplification of dsDNA

For the synthesis of dsDNA fragments the polymerase chain reaction (PCR) was used. The PCR allows the exponential amplification of a DNA using a thermostable DNA polymerase and a large excess of primers that define the 5'- and 3'-end of the DNA fragment to be amplified.

The PCR consists of the cyclic repetition of three reaction steps. In the first step, the denaturation, the dsDNA template is heated for 5 min to 95 °C in order to separate it into the two single strands. During the annealing process, the second step, the primers bind at 55 °C for 20 s to the complementary sequences on the separated strands that serve as templates for the DNA synthesis. In the last step, the elongation step, the polymerase synthesises 72 °C (30 s) a new double-stranded DNA. The dsDNA fragment formed serve as a template for the next cycle, whereby the DNA is amplified exponentially. After 30 cycles, the mixture is cooled down to 4 °C

The concentrations of the components were as following: 1 μM of both primers, 0.2 mM of dNTPs, 0.2 $^{\mathrm{mg}}/_{\mathrm{L}}$ of the template DNA, and 0.02 $^{\mathrm{U}}/_{\mu\mathrm{L}}$ of DNA polymerase. The Amplification of the DNA was performed in a Personal Cycler (Whatman Biometra, Göttingen).

2.2.3 Purification of dsDNA

Double stranded DNA fragments obtained from PCR were purified using a spin-column technique (MinElute PCR Purification Kit, Quiagen). The adsorption of dsDNA to silica depends on pH; at pH $\leq$ 7.5, the dsDNA adsorption is typically 80 %, it is reduced drastically at higher pH. During

the dsDNA binding process all unwanted components like unused primers, salts, enzymes and excess nucelotides do not bind to the silica and flow through the membrane. After washing with ethanol, the dsDNA was eluted off the silica using an appropriate elution buffer.

2.2.4 Agarose gel electrophoresis

The efficiency of the PCR was checked by agarose gel electrophoresis was used. The migration of DNA fragments in an electric field is based on the negative charges of the phosphate groups. The agarose forms a network, which hinders the migration of larger DNA fragments.

The DNA samples obtained and a molecular weight standard were loaded on an agarose gel with an agarose concentration of 1 % and electrophoresed at 80 mA for 15 min. The detection was performed by ethidium bromide staining; ehtidium bromide binds to DNA by intercalation, and the complexes formed absorb light at 312 nm. The gels were washed in an ethidium bromide solution ($5\,\mu g/mL$) for 10 min, afterwards washed with bidestilled water and visualized using a UV-Transilluminator (Bioblock Scientific, Illrich).

2.2.5 Determination of DNA concentration

The concentration of the PCR product was determined by measuring the absorbance at 260 nm using a UV-VIS spectrometer (Beckmann DU 640). An absorption of $A_{260} = 1$ corresponds to a DNA concentration of $50\,\mu g/mL$. The ratio of the absorbance at 260 nm and 280 nm gives an estimate of the DNA purity with respect to UV absorbing contaminants.

2.2.6 Preparation of UV-damaged dsDNA

UV damages on DNA molecules were induced by exposition of DNA solutions to UV light from four germicidal lamps (G8T8, 15 W, 254 nm, Sankyo, Japan). The Eppendorf tubes with opened lids containing the

solutions were kept on ice and at a distance of 10 cm from the UV-light source. After 15 min, the tubes were removed [Hey02, Lys04].

3 Surface Plasmon Resonance[1]

Various methods have been developed to measure the interactions of biomolecules. However, most of the methods are not generally suitable for the real-time analysis of biomolecular interactions. Surface plasmon resonance (SPR) is an optical technique that uses the evanescent wave phenomenon to measure changes in refractive index close to a sensor surface. The binding between an analyte in solution and a receptor immobilized on the sensor surface results in a change in the refractive index [Mys99]. Continuous monitoring of the SPR signal allows the kinetics of binding to be followed in real time and the amount of bound ligand and the association and dissociation rates can be measured with high precision. The main advantage of SPR is that no particular property (e.g. fluorescence or radioactive label) of either of the interacting molecules is required. It is assumed that the rate constants determined by SPR reflect the true association and dissociation rates of the complex formation. This, however, might not be the case, as the immobilization of one of the reaction partners can influence the kinetics of the binding process.

3.1 The SPR Phenomenon

To describe surface plasmon resonance it is helpful to start with the phenomenon of total internal reflection of light at the interface between two non-absorbing media. When a light beam propagates across such an interface from an optical dense medium to a less dense medium, the light is refracted toward the interface. As the angle of incidence increases, a point is reached where the reflected light beam is parallel to the surface:

[1] Parts of the results presented in this chapter have been published [Sch03].

at larger angles of incidence the entire light is reflected inside the medium of higher refractive index. This is called total internal reflection (TIR).

Although the fully reflected beam does not lose any net energy across the interface under TIR conditions, it does transfer an electric field intensity called an evanescent field wave into the lower refractive index medium. The wavelength of the of the evanescent field wave is the same as that of the incident light. The amplitude of the wave decreases exponentially with increasing distance from the interface, decaying over a distance of about one wavelength. Therefore the decay length of the evanescent wave which is useful for measurements is within $\approx$300 nm of the sensor surface.

If the evanescent field wave can interact with a layer of conducting material such as metal, the electric field component lying in the plane of incidence (the p-polarized component) can penetrate the layer and excite collective motion of electrons at the surface of the layer. These excitations are called surface plasmons. Photon and electron behaviour can only be described when they have both wave and particle properties. In accordance with the quantum theory, a plasmon is the particle name of the electron density waves. Therefore, when in a TIR situation the quantum energy of the photons matches the momentum of the plasmon, the photons are converted to plasmons leaving a 'gap' in the reflected light intensity.

Like all conversions, the photon to plasmon transformation must conserve both momentum and energy in the process. Plasmons have a characteristic momentum defined by factors that include the nature of the conducting film and the properties of the medium on either side of the film. Resonance occurs when the momentum of incoming light is equal to the momentum of the plasmons (momentum resonance). The momentum of the photons and plasmons can be described by a vector function with both magnitude and direction. The relative magnitude of the components changes when the angle or wavelength of the incident light changes. However, plasmons are confined to the plane of the gold film, so for SPR it is only the vector component parallel to the surface that matters. Thus, the energy and the angle of incident light must match to form surface plasmon

resonance.

3.1.1 Conditions affecting SPR

The surface plasmon resonance angle mainly depends on the properties of the metal film, the wavelength of the incident light and the refractive index of the media on either side of the metal film [Bia97]. Because the refractive index is sensitive to temperature, it is important to perform the measurements at defined temperatures. In some cases, this dependency can be exploited [Roo98]. The metal must have conduction band electrons capable of resonating with the incoming light at a suitable wavelength. Metals that satisfy to this condition are silver, gold, copper, aluminium, sodium and indium. The surface exposed to light must be pure metal. Oxides, sulfides and other films formed by atmospheric exposure interfere with SPR. The most suitable metals for generating SPR at the surface of a glass–aqueous solution interface using visible and NIR light are silver, gold, and aluminum. Silver gives the sharpest dip in reflected light intensity, while the dip is broader for gold and even more for aluminum. This is shown in figure 3.1, a calculation based on [Hän01] for aluminum, silver and gold with a layer thickness of 60, 53, and 60 nm, respectively. Gold is most suitable metal. It produces a strong, easy to measure SPR signal in the near infra-red region. It is very resistant to oxidation and other atmospheric contaminants but it is sufficiently reactive to accommodate coating with a wide variety of binding molecules.

The thickness of the metal layer also influences the shape of the dip, as depicted in figure 3.2, a calculation for a gold layer thickness of 50, 60 and 70 nm based on [Hän01]. Above an optimum thickness, the dip become shallower; below the dip becomes broader. The optimum thickness for gold is about 60 nm. The light source should be monochromatic and polarized in the plane of the surface. Light that is polarized perpendicular to the surface does not contribute to SPR and only increases the background intensity of the reflected light.

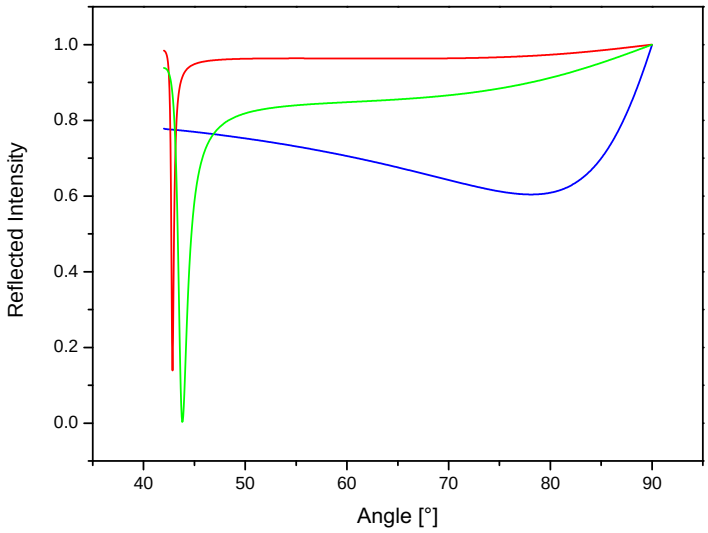

Figure 3.1: Dependency of the reflectance dip on the metal. For a given thickness of metal, silver (—) gives the sharpest dip, while gold (—) gives a somewhat broader profile. Aluminum (—) gives a broad dip with a less defined minimum [Hän01].

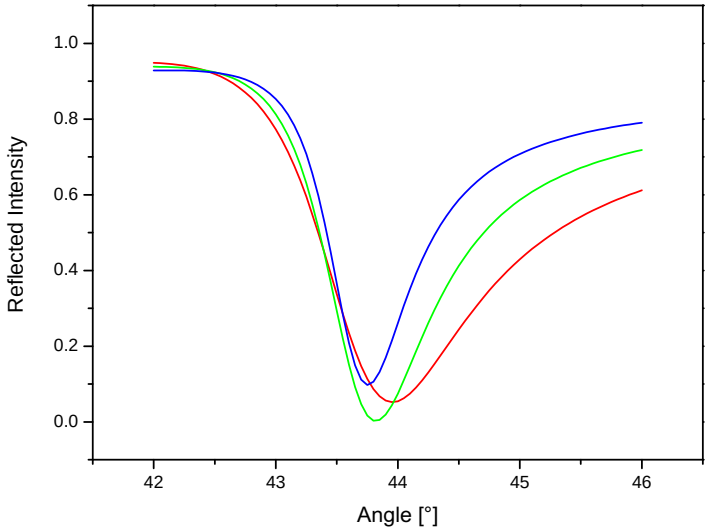

Figure 3.2: Dependency of the reflectance dip on the thickness of the gold layer thickness. Above the optimum metal thickness (—), the dip becomes shallower (—); below this thickness the dip becomes broader (—) [Hän01] .

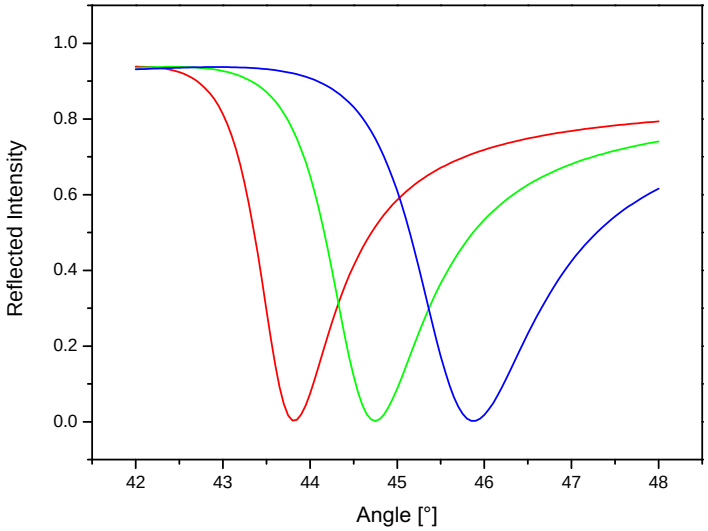

Figure 3.3: Shifting of the dip as function of layer thickness of adsorbed protein. The protein layer thickness is 0 nm (—), 10 nm (—), and 20 nm (—), respectively. A refractive index of 1.4 is assumed for the protein layer. The dip is shifted by ∼2 ° due to a protein layer thickness of 20 nm [Hän01].

Since in experiments the metal film, the incident light, and temperature are kept constant, the SPR signal is solely dependent on changes of the refractive index of the medium on the sensor side of the SPR surface. Depending on the thickness and refractive index of immobilized material, the dip shifts to different angles. This behaviour is shown for different layers of protein (refractive index 1.35–1.50 [Jun98, Ben02]) in figure 3.3. The calculation based on [Hän01] was done for a gold layer thickness of 60 nm, a refractive index of 1.4 and a thickness of 0, 10, and 20 nm for the protein layer. The dip is shifted by ∼ 2 ° due to a protein layer thickness of 20 nm.

3.1.2 The Sensor Chip

The actual sensor chip surface depends on the manufacturer and application to be used. Generally, a glass surface is coated with a thin layer (≈50 nm) of metal. On the metal, a self-assembled monolayer (SAM)

is deposited. This can be hydroxyalkanethiol [Bia97] providing a linker between the metal surface and the next layer. On the SAM a matrix of non-crosslinked carboxymethylated dextran is bound which provides a hydrophilic layer. The dextran is a linear chain of glucose units and provides some advantages: biomolecules can be bound using well defined chemistry, the binding capacity is increased in comparison with a flat surface, the matrix provides a flexible hydrophobic environment, and non-specific binding to the gold surface is reduced. Each glucose unit is modified with one carboxy group [Bia97]. In most cases, the dextran hydrogel is the starting point to covalently bind a ligand to the sensor surface by amine-, thiol- or aldehyde chemistry.

A thiol compound and a gold surface is one of the well established combinations of making a SAM. The n-alkanethiols are the most frequently used compounds in producing SAM surfaces. The sulfur head group generally binds as a thiolate at the three fold hollow site at the Au(111) crystal lattice. A slight mismatch between the pinning distance and the van der Waals diameter of the alkyl chain forces the molecules to assemble in a slightly tilted configuration in order to optimize the lateral interactions [Nag00].

3.1.3 Experimental Setup

Interactions of RPA with ssDNA were monitored using a surface plasmon resonance biosensor instrument, BIACORE X (Biacore AB, Sweden). A schematic drawing of the setup is shown in figure 3.4. Changes in the resonance signal over time are displayed in a graph called sensorgram, which is a direct representation of interaction between molecules in real time. The sensor chip used in all experiments is a BIACORE SA chip (Biacore AB, Sweden) carrying a thin gold film, a dextran layer and a layer of streptavidin attached to the dextran. Streptavidin has a high affinity to biotin ($K_{\mathrm{D}} \approx 10^{-15}$), and can therefore be used for immobilization of biotinylated ssDNA.

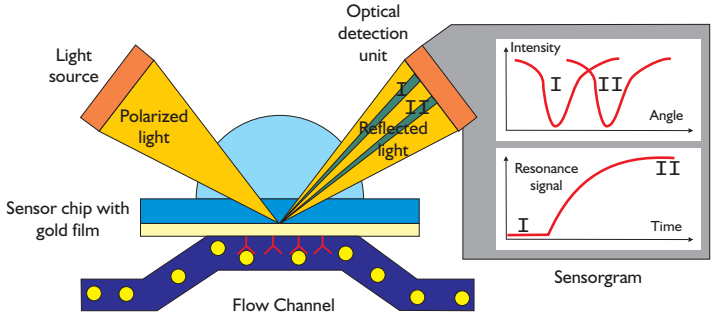

Figure 3.4: Schematic drawing of the BIACORE setup. The light source is a light emitting diode with a wavelength of 760 nm. The polarized light is focused into a wedge-shaped light beam to obtain many angles for the incident light [Nag00].

The BIACORE X system has two flow cells on the sensor chip, which can be used separately or in sequence. Normally the first flow cell is used as a reference cell to correct for refractive index changes, nonspecific binding, and instrument drift.

3.1.4 Data Analysis

Both association and dissociation rate constants can be extrapolated from the data in sensorgrams [Kar91, O'S93]. The ssDNA–RPA interaction data were assumed to follow a simple reversible reaction mechanism

$$A + B \underset{k_\mathrm{d}}{\overset{k_\mathrm{a}}{\rightleftharpoons}} AB. \tag{3.1}$$

A represents the RPA in solution and B the immobilized ssDNA. k_a and k_d are the association and dissociation rate constants, respectively. The rate law is then given by

$$\frac{d\,[AB]}{dt} = k_\mathrm{a}\,[A][B] - k_\mathrm{d}\,[AB] \tag{3.2}$$

The capacity of the chip can be represented by the response units R of the instrument

$$[B] = R_\mathrm{max} - R \tag{3.3}$$

where $R_{\max}$ is the maximum binding capacity of the surface, and R the amount of complex formed ($[AB]$). With this the rate law can be rewritten to

$$\begin{aligned} \frac{d\,R}{dt} &= k_{\mathrm{a}}\,[A]\;(R_{\max} - R) - k_{\mathrm{d}}\,R \\ &= k_{\mathrm{a}}\,[A]\,R_{\max} - (k_{\mathrm{a}}\,[A] + k_{\mathrm{d}})\;R \end{aligned} \tag{3.4}$$

After a certain time the equilibrium between association and dissociation is reached, which can be described by a steady state approximation

$$\frac{d\,R}{dt} = k_{\mathrm{a}}\,[A]\;(R_{\max} - R_{\mathrm{eq}}) - k_{\mathrm{d}}\,R_{\mathrm{eq}} = 0 \tag{3.5}$$

where R_{eq} is the amount of complex formed in equilibrium. This value can be calculated using

$$R_{eq} = \frac{k_{\mathrm{a}}\,[A]\,R_{\max}}{k_{\mathrm{a}}\,[A] + k_{\mathrm{d}}} \tag{3.6}$$

To follow the progress of the reaction, the rate law

$$\frac{d\,R}{dt} = -\,(k_{\mathrm{a}}\,[A] + k_{\mathrm{d}})\;R + k_{\mathrm{a}}\,[A]\,R_{\max} \tag{3.7}$$

has to be integrated. Solving this inhomogeneous differential equation with the boundary condition $R(t=0) = 0$ yields

$$R(t) = \frac{k_{\mathrm{a}}\,[A]\,R_{\max}}{k_{\mathrm{a}}\,[A] + k_{\mathrm{d}}}\left(1 - e^{-(k_{\mathrm{a}}[A] + k_{\mathrm{d}})\,t}\right) \tag{3.8}$$

$$= R_{\mathrm{eq}}\left(1 - e^{-(k_{\mathrm{a}}[A] + k_{\mathrm{d}})\,t}\right) \tag{3.9}$$

All sensorgrams were also analysed for drifting baseline and mass transport influenced kinetics. Baseline drift in the signal comes from many sources: electrical and optical noise, temperature fluctuations, flow rate changes, air bubbles, regeneration solutions and sample dispersion. To correct for baseline drift a linear term depending on time is added to the

integrated rate laws. Mass transport effects become apparent when the binding process is limited by diffusion-controlled supply of analyte from the solution to the surface. When mass transport is slower than the interaction itself, the observed binding will be limited by the mass transport and the measured rate constants will be lower than the true values. The reaction mechanism is now given by

$$A_{\text{bulk}} \xrightarrow{k_{\text{t}}} A_{\text{surface}} + B \underset{k_{\text{d}}}{\overset{k_{\text{a}}}{\rightleftharpoons}} AB. \tag{3.10}$$

From this one obtains the rate laws

$$\frac{d\left[A_{\text{surface}}\right]}{dt} = k_{\text{t}}\ \left(\left[A_{\text{bulk}}\right] - \left[A_{\text{surface}}\right]\right) - \left(k_{\text{a}}\left[A_{\text{surface}}\right]\left[B\right] - k_{\text{d}}\left[AB\right]\right) \tag{3.11}$$

and

$$\frac{d\left[AB\right]}{dt} = k_{\text{a}}\left[A_{\text{surface}}\right][B] - k_{\text{d}}\left[AB\right]. \tag{3.12}$$

Mass transfer is minimized by immobilizing a lower amount of ligand. Mass transfer limitation can be checked by using different flow rates: when the association and dissociation rate constants are the same at different flow rates no mass transfer limitation is to be expected.

The equilibrium constant K_{D} can now be calculated from the ratio of the kinetic rate constants

$$K_{\text{D}} = \frac{k_{\text{d}}}{k_{\text{a}}}. \tag{3.13}$$

Moreover, the equilibrium constants may be determined from biosensor data if the reaction reaches a steady state response R_{eq} during the association phase. The equilibrium constant can be determined from non-linear least squares curve fitting to equation (3.6). The two rate constants and the equilibrium constant were obtained by non-linear fitting using the BIAevaluation 3.0 software supplied by BIACORE [Bia97].

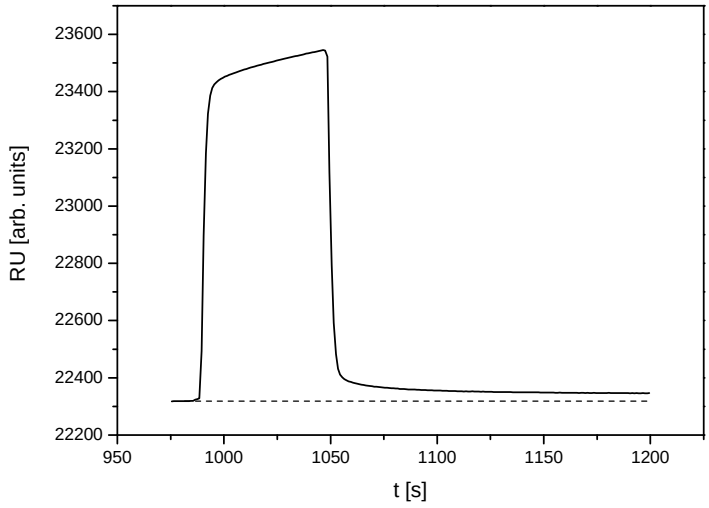

Figure 3.5: Immobilization of a 26-mer oligonucleotide to a streptavidin modified sensor chip. The binding of ssDNA led to an increase of 29 RU, which corresponds to an amount of ssDNA of 2.9 $^{ng}/_{cm^2}$

3.2 Results

3.2.1 Immobilization of biotinylated ssDNA

The biotinylated ssDNA was diluted to 1.5 nM in buffer containing 10 mM sodium acetate, pH 4.8, and 1.0 M NaCl, and manually injected at a flow rate of 5 $^{\mu L}/_{min}$ onto an immobilized streptavidin surface of the BIACORE sensor chip. The first flow cell was left underivatized to correct for refractive index changes, nonspecific binding, and instrument drift.

The progress of DNA immobilization is shown in figure 3.5, the binding led to an increase of 29 RU, which corresponds to an amount of ssDNA of 2.9 $^{ng}/_{cm^2}$. In this graph the increase of the signal is due to both the refractive index change and the binding kinetics, because the reference cell was not used for the immobilization process.

3.2.2 Binding of RPA to ssDNA

Binding to a 26-mer

It is known that RPA binds to ssDNA in different ways, depending on the length of the DNA strand [Bla94]. Only ssDNA molecules longer than 15 to 16 nucleotides are efficiently bound by RPA, and the size of the binding site on the ssDNA strand is between 8 and 10 nucleotides. Therefore we have chosen a 26-mer oligonucleotide in order to avoid binding of more than one RPA per DNA molecule.

Proteins were diluted into running buffer containing 10 mM HEPES, pH 7.4, 150 mM NaCl, 2 mM $MgCl_2$, 0.005 % Polysorbate-20, and 1 mM DTT. The flow rate during the experiments was $10\,{}^{\mu L}/_{min}$. Following RPA binding, regeneration was performed with a 30 s injection of 0.25 % SDS in buffer.

Kinetic analysis of RPA binding required a biosensor surface derivatized with low levels of ssDNA in order to avoid mass-transfer effects and to approach equilibrium binding (figure 3.6). Analysis of the association and dissociation data revealed a dissociation rate constant of $1.31 \pm 0.07 \times 10^{-4}\,{}^{1}/_{s}$ and an association rate constant of $1.25 \pm 0.07 \times 10^{7}\,{}^{1}/_{M\,s}$ at 25 °C. Calculating the equilibrium constant from the kinetic rates yields a value of $K_D = 1.05 \pm 0.08 \times 10^{-11}$ M The value of the equilibrium constant K_D calculated from the dependence of the equilibrium response on the concentration of RPA (equation (3.6)) gave a value of $K_D = 1.08 \pm 0.06 \times 10^{-11}$ M (figure 3.7). The two different ways of analysis gave the same results within the error, showing the consistency of the model.

Binding to a 15-mer

The length of the oligomer for this experiment was chosen to be 15 nucleotides in order to check if the RPA is still able to bind. All other conditions are the same as for the experiments with a 26-mer. As from other biochemical experiments known, the binding of RPA to a shorter DNA should lead to a less stable complex. As it can be seen from figure 3.8, the association

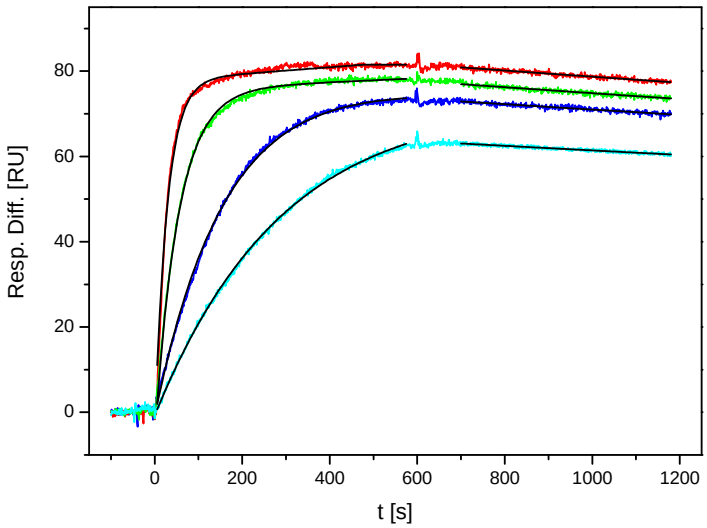

Figure 3.6: SPR sensorgrams showing the interactions between RPA and ssDNA at RPA concentrations of 0.3, 0.5, 1.5, and 3.0 nM at 25 °C. Binding was allowed to proceed for 600 s of association phase followed by 600 s of running buffer injection period for dissociation. All curves are corrected for bulk shift using an underivatized cell. The baseline drift corrected fits for dissociation and association phase are shown in the plot.

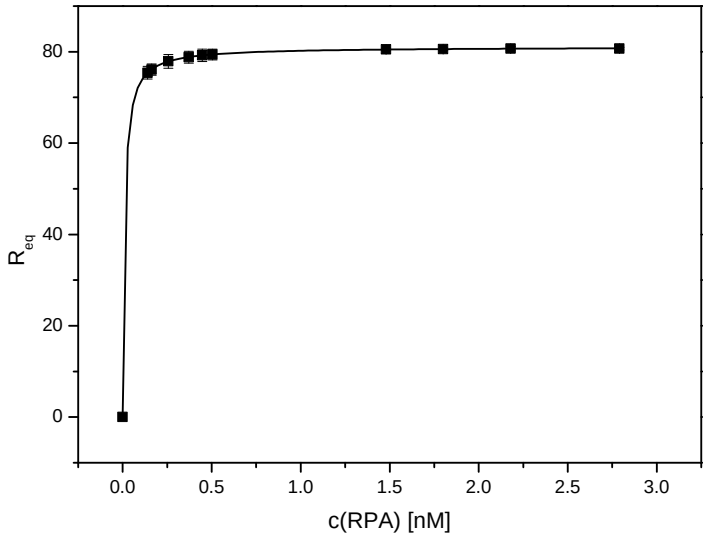

Figure 3.7: Determination of the dissociation constant from equilibrium measurements. The equilibrium response was corrected for bulk refractive index effects.

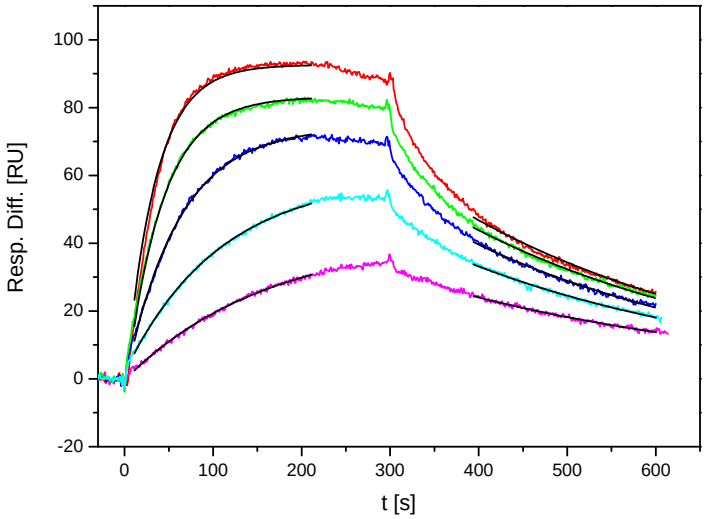

Figure 3.8: SPR sensorgrams showing the interactions between RPA and a 15-mer at RPA concentrations of 0.5, 1.0, 2.0, 3.0, and 4.0 nM at 25 °C. Binding was allowed to proceed for 300 s of association phase followed by 300 s of running buffer injection period for dissociation. All curves are corrected for bulk shift using an underivatized cell. The baseline drift corrected fits for dissociation and association phase are shown in the plot.

kinetics is very similar to the one found for the 26-mer, but the dissociation process is much faster. The analysis of the association and dissociation data revealed a dissociation rate constant of $3.04 \pm 0.17 \times 10^{-3}\,\mathrm{s}^{-1}$ and an association rate constant of $6.62 \pm 0.66 \times 10^{6}\,\mathrm{M}^{-1}\mathrm{s}^{-1}$ at 25 °C. Therefore the association is comparable to the binding process to a 26-mer (by a factor 2 slower), but the dissociation is faster by a factor of 23. The complex is formed, but it is less stable than the complex formed by a 26-mer. Calculating the equilibrium constant from the kinetic rates yields a value of $K_\mathrm{D} = 4.59 \pm 0.38 \times 10^{-10}\,\mathrm{M}$. The value of the equilibrium constant K_D calculated from the dependence of the equilibrium response (figure 3.9) yields consistent results.

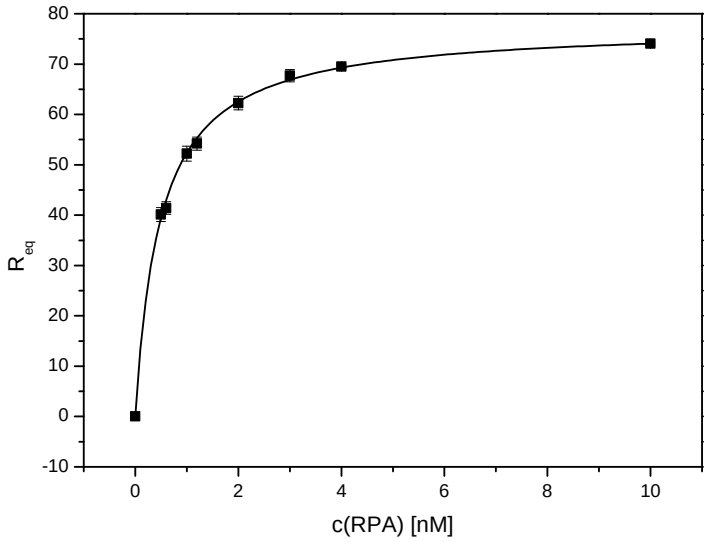

Figure 3.9: Determination of the dissociation constant from equilibrium measurements. The equilibrium response was corrected for bulk refractive index effects.

3.2.3 Temperature-dependent measurements

In order to obtain thermodynamic data of DNA–RPA interactions, temperature dependent measurements were performed. Compared to classical thermodynamic methods like ITC and DSC, SPR requires smallest amounts of DNA and protein.

The temperature was controlled using Peltier elements to maintain a constant temperature at the sensor chip surface, the deviation from the preset temperature was around 0.1 °C. The Gibbs free energy change ΔG for a reaction is related to the equilibrium dissociation constant by

$$\Delta G = -RT \ln K_\mathrm{A} = RT \ln K_\mathrm{D}. \tag{3.14}$$

R is the gas constant and T is the absolute temperature. A noncalorimetric approach to determine the reaction enthalpy ΔH for a binding reaction is the van't Hoff analysis [Hof84]. A key assumption in using the van't Hoff relationship is that the binding reaction involves a single equilibrium throughout the temperature range studied. For protein reactants, it may

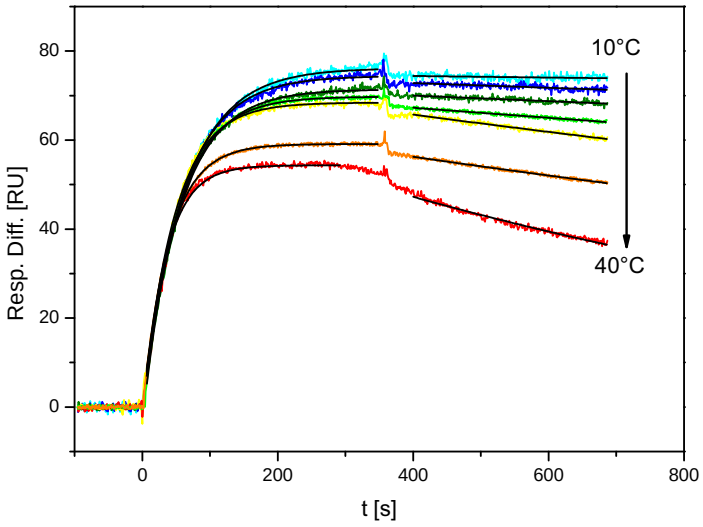

Figure 3.10: Sensorgrams for ssDNA–RPA interactions at 10, 15, 20, 25, 30, 35, and 40 °C. The RPA concentration was 1.7 nM. Binding was allowed to proceed for 360 s of association phase followed by 360 s of running buffer injection period for dissociation. A decrease in the response with increasing temperature is due to the temperature dependence of the refractive index, the rate of dissociation becomes faster with increasing temperature.

Table 3.1: Values of k_a, k_d and K_D for the ssDNA–RPA interactions at various temperatures obtained from SPR experiments.

T [°C]	k_a [$\mathrm{M^{-1}s^{-1}}$]	k_d [$\mathrm{s^{-1}}$]	K_D [M]
10	9.56×10^{6}	2.55×10^{-5}	2.66×10^{-12}
15	1.05×10^{7}	7.27×10^{-5}	6.90×10^{-12}
20	1.08×10^{7}	9.46×10^{-5}	8.78×10^{-12}
25	1.25×10^{7}	1.31×10^{-4}	1.05×10^{-11}
30	1.34×10^{7}	2.82×10^{-4}	2.11×10^{-11}
35	1.52×10^{7}	3.97×10^{-4}	2.61×10^{-11}
40	1.74×10^{7}	8.45×10^{-4}	4.86×10^{-11}

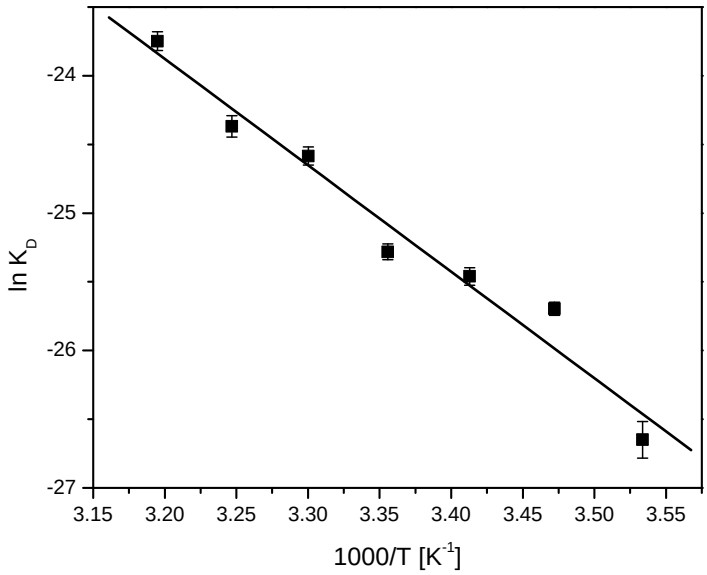

Figure 3.11: van't Hoff plot of the ssDNA–RPA interaction obtained from SPR measurements.

be necessary to establish that they do not aggregate or change conformation over the temperature range studied. For a simple equilibrium reaction, the van't Hoff enthalpy change is calculated from the temperature dependence of a given equilibrium dissociation constant. The relationship between the equilibrium constant and the reaction enthalpy ΔH, and the reaction entropy ΔS, is the van't Hoff expression

$$\ln K_\mathrm{D} = \frac{\Delta H}{R}\frac{1}{T} - \frac{\Delta S}{R}. \tag{3.15}$$

The slope of $\ln K_\mathrm{D}$ vs. $1/T$ provides $\Delta H/R$, from which the enthalpy can be calculated. Evaluating the temperature-dependent measurements (figure 3.10), the values given in table 3.1 were obtained. Performing a van't Hoff analysis (figure 3.11) yielded a value of $\Delta H = -64.4 \pm 5.5\,\mathrm{kJ/mol}$.

To more accurately interpret the thermodynamic parameters, the data were also evaluated using an integrated form of the van't Hoff equation

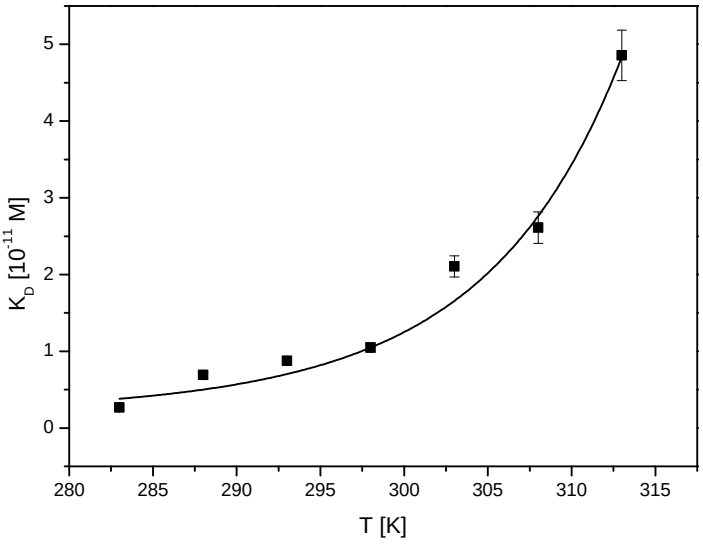

Figure 3.12: Analysis of the temperature dependent data using the integrated form of the van't Hoff equation including a finite, constant heat capacity change.

including a finite, constant heat capacity change ΔC_p

$$K = K^\circ e^{-\frac{\Delta H^\circ}{R}\left(\frac{1}{T}-\frac{1}{T^\circ}\right)} e^{\frac{\Delta C_\mathrm{p} T^\circ}{R}\left(\frac{1}{T}-\frac{1}{T^\circ}\right)} \left(\frac{T}{T^\circ}\right)^{\frac{\Delta C_\mathrm{p}}{R}} \tag{3.16}$$

ΔH° is the reaction enthalpy and K° represents the equilibrium constant for the reaction at a reference temperature T°. The result of the fitting is illustrated in figure 3.12. Evaluating the temperature dependent data using this integrated form gave values of $\Delta H^\circ = -63.5 \pm 9.7\,\mathrm{kJ/mol}$ and $\Delta C_\mathrm{p} = 2.1 \pm 1.4\,\mathrm{kJ/mol\,K}$ at a given $K^\circ(298\,\mathrm{K}) = 1.05 \times 10^{-11}\,\mathrm{M}$. The value of the reaction enthalpy is in good agreement with the value obtained by the van't Hoff analysis (equation (3.15)), but the error of heat capacity change is quite large. Therefore it was assumed that C_p is not changing over the temperature range studied.

The temperature dependent measurements can also be used to obtain the activation energy E_A for the association and dissociation phase using

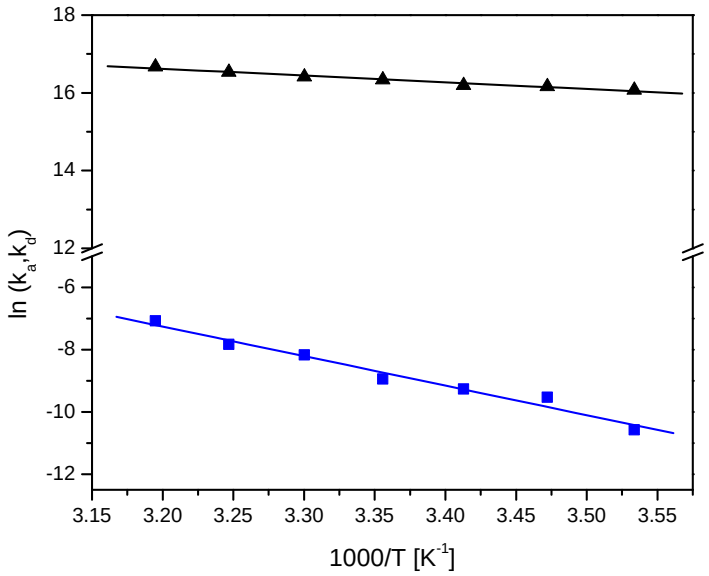

Figure 3.13: Arrhenius plot for the association (▲) and dissociation (■) reaction of RPA with ssDNA obtained from SPR experiments.

the Arrhenius relationship

$$\ln k = \ln k_0 - \frac{E_\mathrm{A}}{R}\frac{1}{T}, \tag{3.17}$$

where k is the apparent rate constant and k_0 is the frequency factor for the given reaction. From the Arrhenius plot shown in figure 3.13 an activation energy $E_A = 14.4 \pm 1.5\,\mathrm{kJ/mol}$ was obtained for the association reaction, indicating that a large amount of energy has to be expended for binding to occur. The activation energy for the dissociation reaction is $78.9 \pm 5.4\,\mathrm{kJ/mol}$. The difference between the activation energies for dissociation and association is equal to the reaction enthalpy. This yields a value for the reaction enthalpy of $-64.5 \pm 5.6\,\mathrm{kJ/mol}$, which is in good agreement with the value of the van't Hoff analysis.

4 Fluorescence Correlation Spectroscopy[1]

Fluorescence Correlation Spectroscopy (FCS), developed in the early 1970s by Elson and Madge [Mag72, Els74, Mag74], is a fluorescence technique for high-resolution spatial and temporal analysis of highly diluted molecules. One is interested in the spontaneous intensity fluctuations of the fluorescence signal caused by minute deviations from the thermal equilibrium (e.g. Brownian motion). In general, all physical parameters that give rise to fluctuations in the fluorescence signal are accessible by FCS. It is possible to determine local concentrations, mobility coefficients or characteristic rate constants of inter- or intramolecular reactions of fluorescently labelled molecules in nanomolar concentration.

4.1 Experimental Setup

The confocal FCS setup is illustrated schematically in figure 4.1. The exciting radiation provided by a laser is directed into a microscope objective via a dichroic mirror and focused onto the sample. For aqueous solutions water immersion objectives with a high numerical aperture (NA > 0.9) are used. The fluorescent light from the sample is collected by the same objective and passed through the dichroic mirror and an emission filter. The pinhole blocks any fluorescent light not originating from the focal region. The light is then focused onto a detector, e.g. an avalanche photodiode or a photomultiplier with single photon sensitivity.

All measurements were made using a ConfoCor 2 FCS instrument (Carl

[1] Parts of the results presented in this chapter have been published [Sch03].

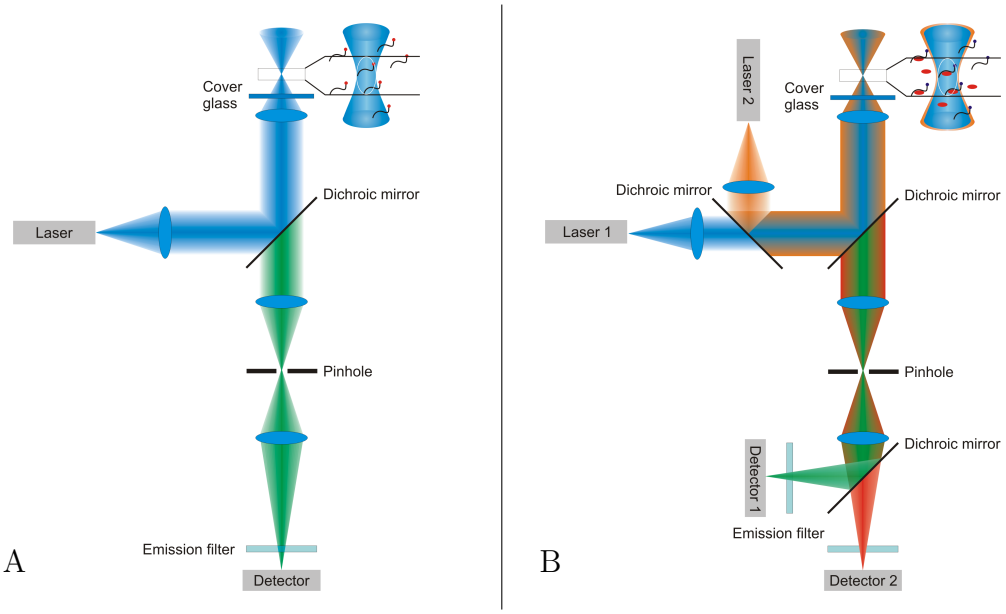

Figure 4.1: Schematical drawing of the confocal FCS setup. (A) One-colour setup. (B) Dual-colour cross-correlation setup.

Zeiss AG, Jena) equipped with an Ar ion laser (458, 488, 514 nm) and two HeNe-lasers (543 and 633 nm). The laser line is selected by an acoustooptical tunable filter (AOTF). Furthermore, the light intensity is modulated by the AOTF for each wavelength independently. The light is delivered to the detection head via optical fibers. The laser light is focussed by the objective into a diffraction-limited spot ($\sim$ 1 fL). Behind the objective, a main dichroic mirror (high transmission for emission light, high reflection for excitation light) in combination with a fluorescence-spectra-adapted bandpass or long-pass filter separates laser light (excitation) and fluorescence light (emission). The emission light passes through a motor-controlled, variable size pinhole, which blocks emission photons produced outside the laser spot. Finally, the photons are detected by a single-photon-counting avalanche photodiode (APD). For the simultaneous registration of two different fluorescent species, additional filters, a second pinhole, and a second APD are used. A software correlator calculates the autocorrela-

tion and, in the two-channel system, the crosscorrelation function of the fluorescence signal in real time. In addition to the software supplied by Zeiss a home-made routine performing least-squares fits was used [Zet01].

4.1.1 Sample Chamber

For test measurements, a simple cover slide (Marienfeld No. 1) was sufficient. For long-term or temperature dependent experiments a homebuilt sample chamber with an 140 μm thick cover slide (Marienfeld No. 1) on the bottom was used. For temperature control we used a Peltier element and two PT100 sensors, one placed close to the Peltier element and the other placed near the sample [Zet02]. The deviation from the preset temperature less than 0.2 °C.

4.1.2 Fluorophores

The requirements imposed on a fluorophore in single molecule techniques are not only high quantum efficiency and large absorption cross section, but also photostability. The photostability of the dye must be high enough to withstand the the enormous power in the laser focus, which may be of the order of several 100 kW/cm^2. Suitable dyes are Alexa dyes (Molecular Probes), rhodamines, cyanines (Amersham Biosciences), Dyomics (Dyomics) and Atto (AttoTec) dyes. Some dyes from these families were used in the experiments of this work; their properties are listed in table 4.1. The major disadvantage of synthetic dyes is that one has to label a biological system (e.g. DNA, proteins). Labelling DNA is straightforward, but labelling of proteins is difficult or almost impossible due to potential changes in functionality or activity induced by the label.

Table 4.1: Properties of dyes used in the studies.

Dye	Absorption [nm]	Emission [nm]	Quantum yield
Cy5	630	670	0.18
Rhodamine 6G	524	552	0.95
Alexa488	495	519	0.52
DY635	647	671	0.2
Atto647	644	669	0.65

4.2 Theoretical Concept

4.2.1 Autocorrelation Analysis

Fluctuations in the fluorescence signal are quantified by temporally autocorrelating the recorded intensity signal. In principle, this autocorrelation routine provides a measure for the self-similarity of a time signal and highlights characteristic time constants of underlying processes.

The number of molecules contained within the focal volume at any time is governed by Poissonian distribution. Therefore, the root mean square fluctuation of the particle number N is given by

$$\frac{\sqrt{\langle(\delta N)^2\rangle}}{\langle N\rangle} = \frac{\sqrt{\langle(N-\langle N\rangle)^2\rangle}}{\langle N\rangle} = \frac{1}{\sqrt{\langle N\rangle}} \tag{4.1}$$

Since the relative fluctuations become smaller with increasing numbers of measured particles, it is important to minimize the number of molecules in the focal volume. The temporal average of the number of particles should be between 0.1 and 1000, in order to obtain a good signal-to-noise ratio. If the focal volume is around one femtoliter, these particle numbers correspond to concentrations between 10^{-6} M and 10^{-9} M.

The fluctuations of the fluorescence signal are defined as the deviations

$\delta F(t)$ from the temporal average of the signal $\langle F(t)\rangle$:

$$F(t) = \langle F(t)\rangle + \delta F(t) \tag{4.2}$$

The fluctuations in the fluorescence signal are due to changes in the local concentration δC caused by diffusion, changes of the photophysics of the fluorophores and chemical reactions like conformational changes and aggregation. The fluorescence fluctuations of a molecule i can be written as

$$\delta F_{\mathrm{i}}(t) = \kappa_{\mathrm{i}} \int_V I_{\mathrm{ex}}(\vec{r}) S_{\mathrm{i}}(\vec{r}) \delta\left(\sigma_{\mathrm{i}} q_{\mathrm{i}} C_{\mathrm{i}}(\vec{r},t)\right) dV \tag{4.3}$$

with the profile of the excitation beam $I_{\mathrm{ex}}(\vec{r})$ and the optical transfer function of the objective-pinhole combination $S_{\mathrm{i}}(\vec{r})$. This function defines the spatial collection efficiency of the setup. κ_{i} represents the overall fluorescence detection efficiency. The dynamics of a single fluorophore is described by the fluctuation term $\delta(\sigma_{\mathrm{i}} q_{\mathrm{i}} C_{\mathrm{i}}(\vec{r},t))$. It includes fluctuations in the molecular absorption cross section $\delta\sigma_{\mathrm{i}}$, in the quantum yield δq_{i} and in the local particle concentration of component i, $\delta C_{\mathrm{i}}(\vec{r},t)$. Because it is impossible to determine all these parameters, the convolution of the two spatial optical functions is often approximated by a three-dimensional Gaussian $W(\vec{r})$, which describes the spatial distribution of the emitted light. This volume is characterised by two lateral and axial distances r_0 and z_0, where the intensity drops to $1/\mathrm{e}^2$:

$$W(\vec{r}) = \frac{I_{\mathrm{ex}}(\vec{r})}{I_0} S(\vec{r}) = e^{\left(-\frac{2(x^2+y^2)}{r_0^2}\right)} e^{\left(-\frac{2z^2}{z_0^2}\right)} \tag{4.4}$$

The remaining parameters κ_{i}, σ_{i}, and q_{i} can be combined with the excitation intensity amplitude I_0 to give the parameter photon count rate per molecule and second:

$$\eta_{\mathrm{i}} = I_0 \kappa_{\mathrm{i}} \sigma_{\mathrm{i}} q_{\mathrm{i}} \tag{4.5}$$

This parameter is a measure for the signal-to-noise ratio of the measurement and can be therefore used for a comparison of the quality of different

adjustments or setups. Equation (4.3) can now be rewritten:

$$\delta F_{\mathrm{i}}(t) = \int_V W(\vec{r})\delta(\eta_{\mathrm{i}} C_{\mathrm{i}}(\vec{r},t))dV \tag{4.6}$$

From this it can be seen that the time dependent fluorescence fluctuations are given by the optical setup, by changes in the optical properties of the dye molecule, and by the concentration fluctuations of the molecules.

The normalized autocorrelation function is defined as:

$$G(\tau) = \frac{\langle F(t)F(t+\tau)\rangle}{\langle F(t)\rangle^2} = \frac{\langle \delta F(t)\delta F(t+\tau)\rangle}{\langle F(t)\rangle^2} + 1 \tag{4.7}$$

This function analyses the signal with respect to its self-similarity after the lag time τ [Sch01a].

Assuming that the fluorescence properties of the fluorophore are not changing within the observation time, i.e. the fluorescence fluctuations are caused by changes in concentration of the fluorescent molecules (Brownian motion).

$$C(\vec{r},t) = \langle C\rangle + \delta C(\vec{r},t) \tag{4.8}$$

The concentration fluctuations $\delta C(\vec{r},t)$ can be described by free diffusion of particles in three dimensions. Using Fick's law then yields:

$$\frac{\partial \delta C_{\mathrm{j}}(\vec{r},t)}{\partial t} = D_{\mathrm{j}} \nabla^2 \delta C_{\mathrm{j}}(\vec{r},t) \tag{4.9}$$

where D_{j} is the diffusion constant of component j and C_{j} is the concentration of this component at $\vec{r}$ at the time t. Now the so called number density autocorrelation term can be calculated:

$$\langle \delta C(\vec{r},0)\delta C(\vec{r'},\tau)\rangle = \langle C\rangle \frac{1}{(4\pi D\tau)^{-3/2}} e^{-\frac{(\vec{r}-\vec{r'})^2}{4D\tau}} \tag{4.10}$$

Inserting equations (4.4), (4.6), and (4.10) into equation (4.7) one obtains

the autocorrelation function for freely diffusing molecules. Using

$$D = \frac{r_0^2}{4\tau_\mathrm{D}} \tag{4.11}$$

yields

$$G(\tau) = \frac{1}{\langle N \rangle} \frac{1}{1 + \frac{\tau 4D}{r_0^2}} \frac{1}{\sqrt{1 + \frac{\tau 4D}{z_0^2}}} + 1 = \frac{1}{\langle N \rangle} \frac{1}{1 + \frac{\tau}{\tau_\mathrm{D}}} \frac{1}{\sqrt{1 + \frac{\tau}{S^2 \tau_\mathrm{D}}}} + 1 \tag{4.12}$$

where $\langle N \rangle$ is the average number of fluorescent molecules in the observation volume, $S = \frac{z_0}{r_0}$ is the structure parameter, which describes the shape of the volume, and τ_D is the average diffusion time of a molecule.

The assumption that the fluorescence properties of the fluorophore are not changing with time is not necessarily true for real dyes. A common behaviour is the flickering in fluorescence intensity, which can be explained by a transition of the dye to the first excited triplet state. This transition is forbidden by quantum mechanics, therefore the relaxation back to the ground state takes longer than the relaxation from the singulet excited state. While the dye is in the triplet state, it cannot emit any fluorescence light and therefore appears dark. Instead of recalculating the autocorrelation function, the triplet dynamics is separated from the diffusion dynamics:

$$G(\tau) = G_\mathrm{diffusion}(\tau) G_\mathrm{triplet}(\tau) \tag{4.13}$$

The triplet blinking can be described by a simple exponential decay.

$$G_\mathrm{triplet}(\tau) = 1 - T + T e^{-\frac{\tau}{\tau_\mathrm{triplet}}} \tag{4.14}$$

where T is the fraction of molecules in the triplet state and τ_triplet is the decay time of the triplet state. Using equations (4.13) and (4.14) gives the autocorrelation function for a freely diffusing particle including triplet

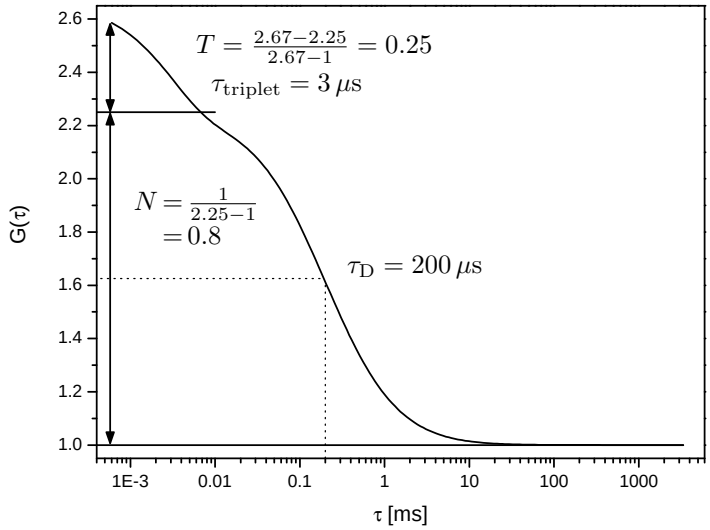

Figure 4.2: Typical autocorrelation curve of a freely diffusing particle including triplet excitation with a diffusion time τ_{D}=200 μs, an average particle number of N =0.8, a triplet fraction of T =0.25 with a triplet lifetime of τ_{triplet}=3 μs.

excitation:

$$G(\tau) = (1 - T + Te^{-\frac{\tau}{\tau_{\mathrm{triplet}}}})\frac{1}{\langle N\rangle}\frac{1}{1+\frac{\tau}{\tau_{\mathrm{D}}}}\frac{1}{\sqrt{1+\frac{\tau}{S^2\tau_{\mathrm{D}}}}} + 1 \tag{4.15}$$

A typical autocorrelation curve including a triplet decay is shown in figure 4.2. From the autocorrelation curve one can obtain the average number of molecules N in the observation volume, the time τ_{D} the molecules need to diffuse through the volume, the fraction T of molecules in the first excited triplet state, and the decay time of the triplet state τ_{triplet}. If the excitation volume is known from calibration measurements, the local concentration of fluorescent particles can be determined. For K different fluorescent particles exhibiting different diffusion times τ_{i} (e.g. ssDNA and ssDNA–RPA complex) the autocorrelation function is given by [Wid95]:

$$G(\tau) = (1 - T + Te^{-\frac{\tau}{\tau_{\mathrm{triplet}}}})\frac{1}{\langle N\rangle}\sum_{i=1}^{K}\frac{\phi_{\mathrm{i}}}{1+\frac{\tau}{\tau_{\mathrm{i}}}}\frac{1}{\sqrt{1+\frac{\tau}{S^2\tau_i}}} + 1 \tag{4.16}$$

where ϕ_i is the fraction of the ith component. In order to distinguish the different particles, the diffusion times have to differ at least by a factor of 1.6. This corresponds to a factor of 4 regarding the molar masses.

4.2.2 Cross-correlation Analysis

An important extension of the FCS is the simultaneous detection of the two colour-channels [Eig94, Ket98, Ric89, Rig98, Sch97]. Two spectrally distinct dyes are excited at two different wavelengths. Their fluorescence light is split subsequently by dichroic mirrors and filters into the respective detection channels. With two-colour FCS, a cross-correlation analysis can be made (FCCS), where the signals of the two channels are time correlated with each other to collect information only about particles that carry both types of dyes. This method of data analysis is useful if the difference in the molecular masses, and therefore in diffusion times, of two binding partners is not large enough for autocorrelation analysis.

The cross-correlation theory can be described in analogy to the autocorrelation theory. Generalizing equation (4.6), the fluctuating signals in the two detection channels (green channel G and red channel R) are given as

$$\delta F_G(t) = \int_V W(\vec{r})\eta_G \delta(C_G(\vec{r},t) + C_{GR}(\vec{r},t))dV \tag{4.17}$$

$$\delta F_R(t) = \int_V W(\vec{r})\eta_R \delta(C_R(\vec{r},t) + C_{GR}(\vec{r},t))dV \tag{4.18}$$

with the concentrations of the single labelled species $C_i(\vec{r},t)$, and the concentration of the double-labelled species $C_{GR}(\vec{r},t)$. Now the number of molecules N_{GR} carrying both fluorophores in the volume is given by

$$N_{GR} = \frac{N_G N_R}{N_{CC}} \tag{4.19}$$

where N_G and N_R represent the particle numbers in the two autocorrelation channels respectively, and N_{CC} is the inverse amplitude of the cross-

correlation. This is only valid if there is no cross-talk, meaning the fluorescent light of the green dye is also detected in the red detection channel.

The effective volume and the diffusion time for the cross-correlation function are given by [Sch97]:

$$V_{\text{eff}} = \frac{\pi^{3/2}\left(r_{\text{G}}^2 + r_{\text{R}}^2\right)\left(z_{\text{G}}^2 + z_{\text{R}}^2\right)^{1/2}}{2^{3/2}} \tag{4.20}$$

$$\tau_{\text{GR}} = \frac{\left(r_{\text{G}}^2 + r_{\text{R}}^2\right)}{8D_{\text{GR}}} \tag{4.21}$$

Therefore, when different laser spot sizes are used, the cross-correlation curve lies between the two autocorrelation curves.

4.2.3 Artefacts

Refractive Index

An important issue when focusing a laser through a high-NA objective and detecting through the same objective is the refractive index of the sample. Focusing and detection will be optimal only if the refractive index of the sample exactly matches that of the immersion medium of the objective. In all experiments a water immersion objective was used, therefore the refractive index of the immersion medium is 1.33. However, when performing FCS in buffer solutions or at various temperatures, the refractive index of the sample may be differ from the refractive index of the immersion medium. The refractive index mismatch introduces slight aberrations into the laser focusing and the confocal fluorescence detection, and leads additionally to a slight offset of center of focus and center of detection along the optical axis. Both effects lead to an apparently larger detection volume and thus to an apparently smaller diffusion coefficient. The effect of the refractive index mismatch on the focus is illustrated in figure 4.3. The calculation was done by J. Enderlein, Jülich. As it can be seen also from this figure, the influence on the focus, and therefore on the volume, is much smaller when setting the focus closer to the surface of the cover

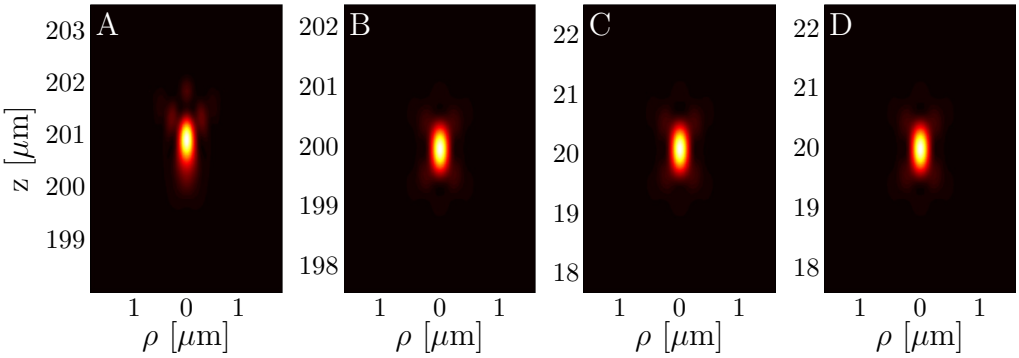

Figure 4.3: The influence of the refractive index mismatch on the focus (by J. Enderlein, Jülich). (A) Calculation for the refractive index of the used buffer at 10 °C (n =1.3360), the focus is placed 200 μm above the surface of the cover slide. The volume is 0.64 fL. (B) Refractive index of the used buffer at 40 °C (n=1.3329), same focus distance. The volume is 0.43 fL. (C) Same as in (A), but the focus is placed 20 μm above the surface of the cover slide. The volume is now 0.43 fL. (D) Same as in (B), same focus distance as in (C). The volume is now 0.42 fL.

slide. Therefore, some of the measurements in this work were performed at a distance of 50 μm instead of 200 μm. Measuring closer to the coverslide surface has one drawback: the diffusion of the particle may be influenced by the surface.

Foci displacement FCCS

In a two-colour setup, additional aspects have to be considered. First, in nonideal systems there can be a considerable amount of cross-talk due to the broad absorption and emission spectra of the dyes. It must be taken into account that both dyes may be excited to some extent by both lasers and emit in both spectral detection ranges. Selecting a proper dye system (although it is hardly possible to find a perfectly separable dyes) the effect of cross-talk can be neglected. Second, the size of the observation volumes is wavelength dependent. The linear dimensions are in first order proportional to the excitation wavelength, resulting in focal volumes differing by a factor of 2.18 for the commonly used laser lines of 488 nm

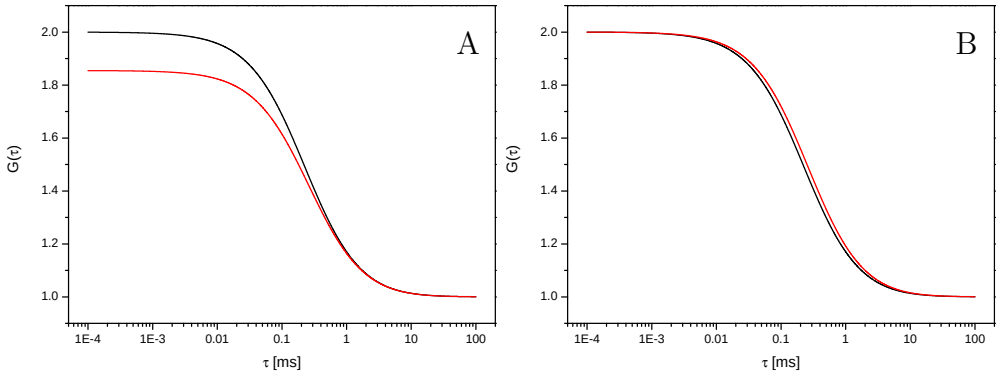

Figure 4.4: Influence of the displacement on the cross-correlation curve. (A) Cross-correlation curve, (B) normalized cross-correlation curve. The diffusion time of a particle with a concentration of ∼10 nM in a perfectly aligned setup would be 218 μs, the lateral and axial distances for the blue and red channel are 160 nm, 800 nm, 208 nm, and 1040 nm, respectively. The lateral and axial displacement of the two foci of 50 nm in x- and y-direction and 100 nm in z-direction leads to a decrease of 15 % in amplitude (A), and an increase in diffusion time to 252 μs (B).

and 633 nm. Third, the centres of the respective foci may show an axial or lateral displacement, due to chromatic aberrations along the optical path. In confocal laser scanning microscopy, values between 50 and 100 nm have been reported [Ede99, Esa00], which is of the order of the beam waist and thus not negligible. The displacement produces a noticeable reduction of the amplitude and a slightly slower decay of the correlation function, corresponding to an apparently longer diffusion time, as shown in figure 4.4 [Wei02]. The calculation was performed for a fluorophore with a concentration of $\sim$ 10 nM and a diffusion time in a perfectly aligned setup of 218 μs. The two lateral and axial distances r_0 and z_0 have a value of 160 nm and 800 nm for the blue channel, and a value of 208 nm and 1040 nm for the red channel, respectively. The centres of the foci are displaced by 50 nm in x and y-direction and by 100 nm in z-direction. This displacement leads to a decrease of 15 %, and the diffusion time is increased to 252 μs.

4.3 Results

4.3.1 Binding of RPA to ssDNA

In addition to the SPR experiments, the binding of RPA to the 26-mer labeled with Cy5 was also studied by FCS. The same system, including the buffer, was used for this study. For the measurements, a HeNe-laser with 5 mW power at 633 nm was focused by a water immersion Zeiss C Apochromat 40 × 1.2 objective. A 90 μm pinhole was used in the confocal detection channel. The focus of the lens was placed 200 μm above the surface of the cover slide.

Normalized autocorrelation curves for the ssDNA–RPA interaction for different RPA concentrations are shown in figure 4.5. For the determination of the diffusion times of ssDNA and ssDNA–RPA complex the structure parameter S is required, which can be obtained from the measurement of Cy5. The diffusion times of free and protein-bound ssDNA were determined from the autocorrelation functions with no protein and excess of protein in the solution from the fit to a one component model, (equation (4.15)). From this a diffusion time $\tau_{\mathrm{DNA}} = 152.1 \pm 2.4\,\mu$s for the free DNA and $\tau_{\mathrm{complex}} = 450.8 \pm 5.2\,\mu$s for the complex could be obtained at 25 °C. The measured diffusion time of the complex can by used to determine the hydrodynamic radius R_{h} by the Stokes-Einstein equation

$$D = \frac{k\,T}{6\pi\eta R_{\mathrm{h}}} \tag{4.22}$$

where η is the viscosity of the solution. Calculations yield a value of ~ 7 nm, which is in good agreement with AFM ([Lys04] and cryo-TEM experiments.

The progress of complex formation as a function of RPA concentration is depicted in figure 4.6, which is obtained by a reverse titration of RPA against ssDNA at a constant concentration. In order to determine the equilibrium constant K_{D}, the measured diffusion time has to be converted into the degree of binding. For that purpose the autocorrelation func-

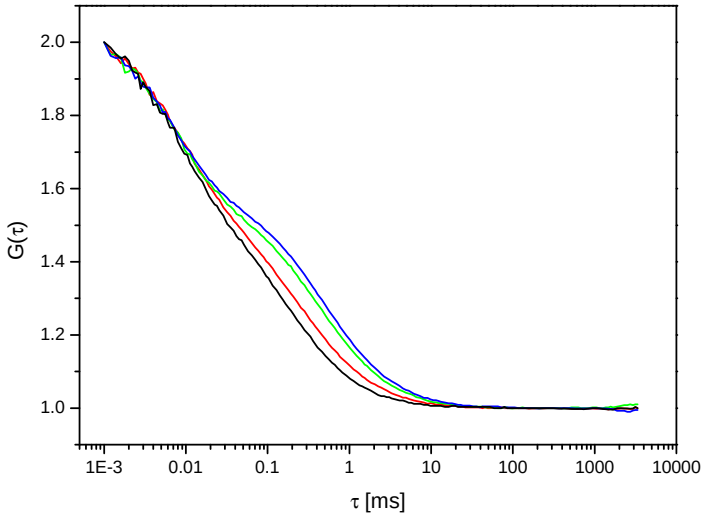

Figure 4.5: Normalized autocorrelation functions for different RPA concentrations at 25 °C. The percentage of complex was determined by a two component fit to each function. Curves for 0 % (—), 40 % (—), 81 % (—) and 100 % (—) ssDNA–RPA complex are shown. An increase in diffusion time with increasing complex fraction can clearly be seen.

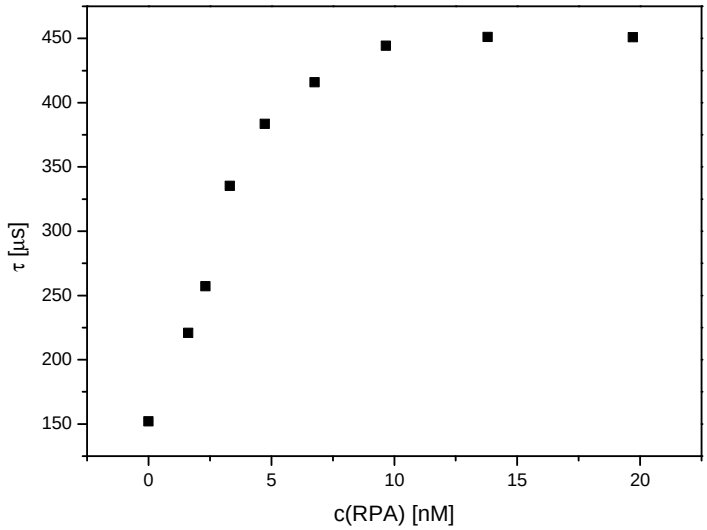

Figure 4.6: Progress of complex formation at 25 °C as a function of RPA concentration.

tions for the complex formation were fitted using equation (4.16) for two particles ($K = 2$), i.e. ssDNA molecules and ssDNA–RPA complexes. The two diffusion times τ_{DNA} and τ_{complex} obtained from measurements of the free ssDNA and at saturating protein concentrations were kept fix for this fitting procedure. The degree of binding $\theta = \phi_2 = 1 - \phi_1$ remained the only unknown parameter and was determined from equation (4.16) at each titration point.

The relationship between the equilibrium constant and the degree of binding θ can be derived from the law of mass action:

$$K_{\mathrm{D}} = \frac{(1-\theta)[B]([A]-\theta[B])}{\theta[B]} \tag{4.23}$$

where $[A]$ is the RPA concentration, $[B]$ is the concentration of ssDNA, and K_{D} is the equilibrium constant for the dissociation. Rearranging this equation and solving the quadratic formula leads to

$$\theta = \frac{[A]+[B]+K_{\mathrm{D}} \pm \sqrt{[B]^2 - 2[A][B] + 2[B]K_{\mathrm{D}} + 2K_{\mathrm{D}}[A] + [B]^2 + K_{\mathrm{D}}^2}}{2[B]} \tag{4.24}$$

Only the solution where $\theta = 1$ for high [RPA] is a meaningful solution, therefore

$$\theta = \frac{[A]+[B]+K_{\mathrm{D}} - \sqrt{[B]^2 - 2[A][B] + 2[B]K_{\mathrm{D}} + 2K_{\mathrm{D}}[A] + [A]^2 + K_{\mathrm{D}}^2}}{2[B]} \tag{4.25}$$

Replacing $\alpha = [A] + [B] + K_{\mathrm{D}}$ and simplifying yields

$$\theta = \frac{\alpha - \sqrt{\alpha^2 - 4[A][B]}}{2[B]} \tag{4.26}$$

The resulting data (degree of binding as a function of RPA concentration) and the corresponding fit using equation (4.26) is shown in figure 4.7. The fit resulted in a value of $2.61 \pm 0.80 \times 10^{-10}\,\mathrm{M}$ for K_{D} at 25 °C. In order to ensure that the dissociation and formation processes are not kinetically

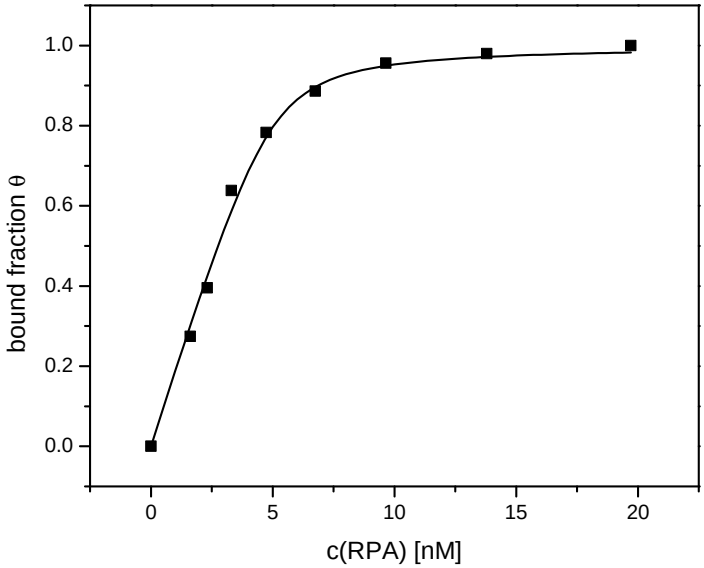

Figure 4.7: Degree of binding at 25 °C as a function of RPA concentration.

hindered, the complex formation was observed also by adding protein to ssDNA, yielding the same value for the equilibrium constant. Comparing this value with the one obtained by SPR, one finds that the equilibrium constant is larger by a factor of 25. In order to explain the difference between the equilibrium constants, one has to take also a closer look at the thermodynamics of biomolecular interactions (see 4.3.3).

In the above FCS experiments the quantum efficiency of the dye was not influenced by the binding process. Previous experiments showed that the binding of DNA to RPA is not altered significantly by attaching a label to the DNA [Hey01]. It was found that the equilibrium constant remained the same within the experimental error for labelled and unlabelled DNA. Moreover, there was no interaction between RPA and free Cy5. Therefore significant deviations due to labelling can be ruled out in the experiments. Photobleaching occurred at laser attenuation above 0.7 %, therefore, the experiments were performed below this threshold value. Photobleaching also occurred at RPA concentrations above a concentration of 50 nM, which indicates that a slowly diffusing complex with

two or more RPA molecules is formed. It is known that RPA forms dimers or trimers upon binding to DNA [Bla94], depending on the length of the DNA.

4.3.2 Binding of RPA to dsDNA

The experiments on the interaction between RPA and DNA were then extended to dsDNA without and with a damage site. For these measurements the ssDNA strands given in table 2.1 were hybridized, and an Ar-laser with 50 mW power at 488 nm was focused into the solution. A 70 μm pinhole was used in the confocal detection channel. The focus of the lens was placed 50 μm above the surface of the cover slide.

The diffusion coefficient for dsDNA with 58bp without any damaged site was determined to be $D = 4.24 \times 10^{-11}\,\mathrm{m^2/s}$ at 20 °C. This value can be compared with an estimated diffusion coefficient of a rod-like molecule, which is defined by [Tir84]:

$$D = \frac{A\,k\,T}{3\pi\eta L} \tag{4.27}$$

where A represents a correction factor given by

$$A = \ln\frac{L}{d} + 0.312 + \frac{0.565}{\frac{L}{d}} - \frac{0.1}{\left(\frac{L}{d}\right)^2} \tag{4.28}$$

where L is the length and d is the diameter of the rod-like molecule. In case of a 58bp dsDNA, L and d have a value of 19.7 nm (0.34 nm rise per bp) and 2.4 nm, respectively. For a 58bp DNA, the estimated diffusion coefficient is then $D = 5.42 \times 10^{-11}\,\mathrm{m^2/s}$ at 20 °C. Therefore the experimental value is in agreement with the estimated value. Deviations may be due to the estimated correction factor A and a not exactly determined lateral radius r_0.

The autocorrelation curve for the interaction of RPA with undamaged DNA is shown in figure 4.8. Although the RPA was added in 380-fold

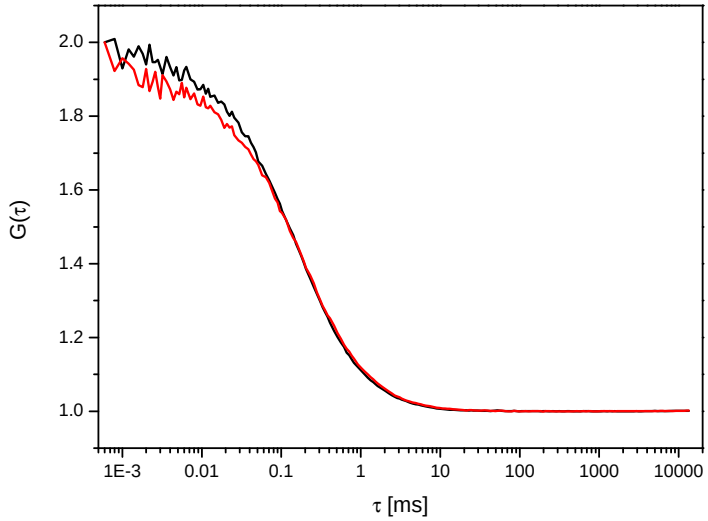

Figure 4.8: Autocorrelation curve for the binding of RPA to undamaged dsDNA (—). As a reference the autocorrelation curve for free undamaged dsDNA is also shown (—). Although the RPA was added in 380-fold excess, only a slight increase of the diffusion time occurred, which corresponds to a complex formation of ∼15 %.

excess, only $\sim 15\,\%$ of complexes are formed. This corresponds well to the results found in AFM experiments [Lys02], where only rarely terminal binding of RPA to undamaged dsDNA occured. Instead of using intact dsDNA, now dsDNA with a distinct damage site was used for the experiment. The same experiment as before was performed using a dsDNA fragment with a bubble damage site (see figure 2.1). In this case the diffusion time increased strongly, as depicted in figure 4.9, showing a complex formation between RPA and damaged DNA. In a next step a titration curve was recorded for this interaction, which is shown in figure 4.10. Evaluating this curve yielded a value of $K_\mathrm{D} = 7.6 \pm 0.6 \times 10^{-9}\,\mathrm{M}$, which is comparable to the value found for a similar bubble-dsDNA using fluorescence anisotropy measurements ($K_\mathrm{D} = 16 \pm 3 \times 10^{-9}\,\mathrm{M}$) [Hey01]. The difference can be explained by different buffers and salt concentrations used.

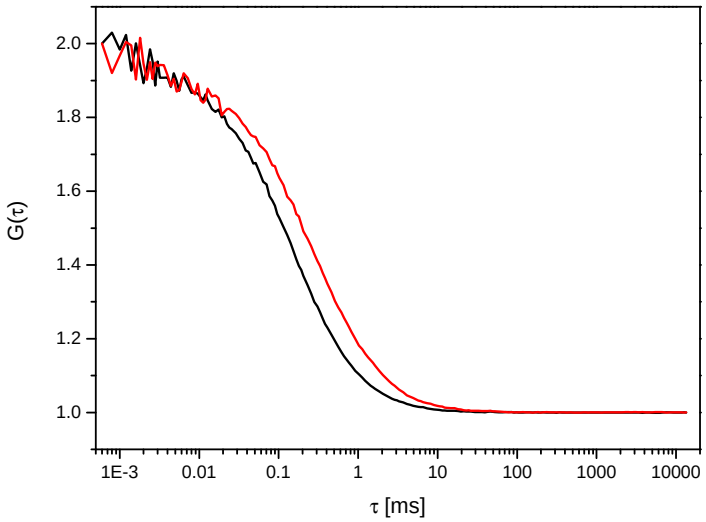

Figure 4.9: Autocorrelation curve for the binding of RPA to dsDNA with a bubble (—). The diffusion time increased strongly due to complex formation. As a reference the autocorrelation curve for free dsDNA with a bubble is also shown (—). The damage site is responsible for the binding of RPA to the DNA.

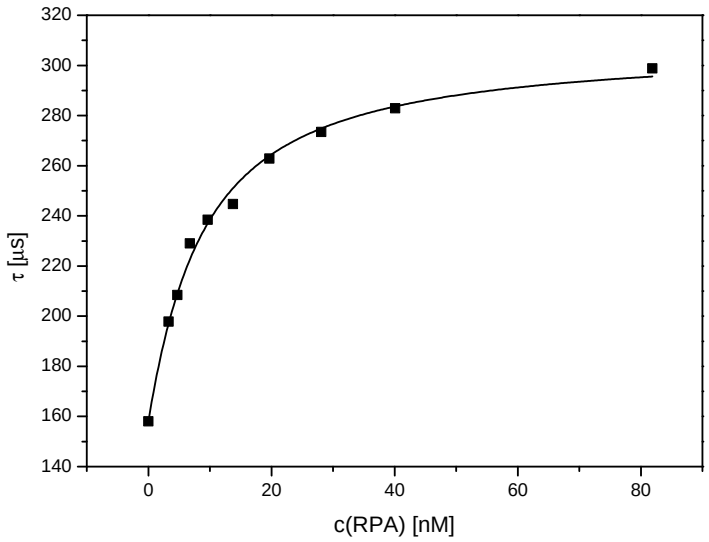

Figure 4.10: Titration curve for the binding of RPA to dsDNA with a bubble. Evaluating this data like the titration curves in section 4.3.1 yielded a value of $K_{\mathrm{D}} = 7.6 \pm 0.6 \times 10^{-9}$ M.

4.3.3 Temperature-dependent measurements

Comparing the FCS data obtained so far with the SPR data shows that the two methods yielded different values for the equilibrium constant. In order to explain the difference between the equilibrium constants, one has to take a closer look at the thermodynamics of biomolecular interactions. Therefore, one has to perform temperature dependent measurements in FCS, which in turn leads to the need of a new setup for FCS. This setup was developed by H. Zettl [Zet02] and used extensively in this work. For all the measurements, a HeNe-laser with 5 mW power at 633 nm was focused into the solution. A 90 μm pinhole was used in the confocal detection channel. The focus of the lens was placed 200 μm above the surface of the cover slide.

As a very first experiment, the temperature dependence of the diffusion coefficients D_i of Cy5, ssDNA and the ssDNA–RPA complex, respectively, were measured. The diffusion coefficients were calculated from the measured diffusion times using equation 4.11, where the radius r_0 can be determined from the diffusion time and the known diffusion coefficient of Cy5 ($D_{\mathrm{Cy5}} = 3.16 \times 10^{-10}\,\mathrm{m^2/s}$) [Zei01].

The dynamics of molecules in liquids are not well understood, numerous theoretical models are found in literature. A simple approach is to assume an Arrhenius behaviour of the temperature dependence of the diffusion coefficient [McC59], i.e.

$$D = D_0 e^{-E_\mathrm{A}/RT} \tag{4.29}$$

with an activation energy E_A which is equal to the enthalpy barrier to molecular migration (figure 4.11). The activation energies found for Cy5, ssDNA and the ssDNA–RPA complex are $12.85 \pm 0.55\,\mathrm{kJ/mol}$, $10.66 \pm 0.66\,\mathrm{kJ/mol}$, and $13.28 \pm 0.57\,\mathrm{kJ/mol}$, respectively. The different activation energies may be explained by the size and the effective charge of the molecules. Cy5 is a small molecule with a low charge density compared to the 26-mer, therefore Cy5 has a smaller hydration shell than the ssDNA. The role of the hydration shell regarding the activation energy is not clear,

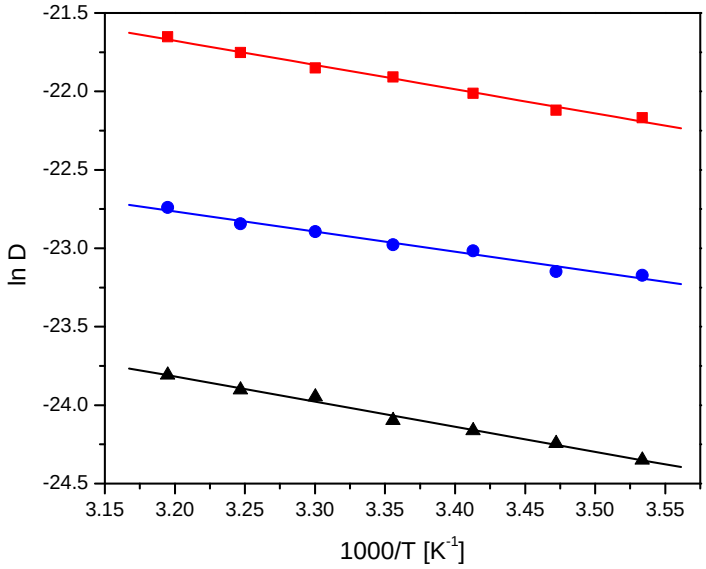

Figure 4.11: Temperature dependence of the diffusion coefficient for Cy5 (■), ssDNA (●) and ssDNA–RPA complex (▲) according to an Arrhenius behaviour. The diffusion coefficients were calculated using eqn. (4.11)

but one may assume that a larger hydration shell might reduce the energy barrier of migration. This might explain the higher activation energy for the diffusion of Cy5 compared to the bigger ssDNA molecule. The ssDNA–RPA complex exhibits the highest barrier for the molecular migration due to the size of the molecule. It has to be stated that the diffusion of molecules is not well understood and here only a very simple model was used for data analysis, therefore the interpretation of the activation energies is very vague.

The fluorescence emission rate per dye molecule increased by approximately 50% when the temperature was decreased from 40 °C to 10 °C. This tendency has also been observed by Widengren *et al.* [Wid00]. It has to be noted, however, that the data analysis described above is not influenced by this effect, as long as the intensity of the signal is sufficiently high and as long as the data set for each temperature is evaluated seperately.

In a second step, the thermodynamics of ssDNA–RPA interactions were

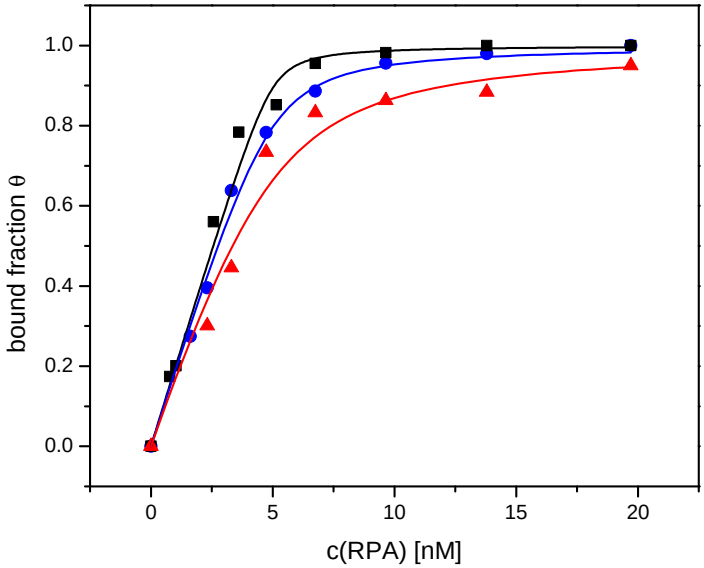

Figure 4.12: Titration curves derived from the autocorrelation functions for a DNA concentration of 5 nM at 10 °C (■), 25 °C (●) and 40 °C (▲).

investigated, in order to obtain more information about the difference between the equilibrium constants found by SPR and FCS. Therefore, titration experiments at various temperatures were performed. The titration curves derived from autocorrelation functions at various temperatures are depicted in figure 4.12. The measurements were performed at DNA concentrations of 1 nM and 5 nM. Unfortunately, it was not possible to obtain reliable data for temperatures above 25 °C at 1 nM DNA (figure 4.13). It can be assumed that this is due to instabilities of the dye and the protein in very dilute solutions. Nevertheless, the equilibrium constants obtained from both experiments are the same within the experimental error. The K_D values obtained from these titration curves ranged from 0.64 to 8.52×10^{-10} M in the temperature range studied. Performing a van't Hoff analysis (figure 4.14, a value for the enthalpy of the reaction ΔH of $-66.5 \pm 8.9\,{}^{\mathrm{kJ}}/_{\mathrm{mol}}$ was obtained.

The equilibrium constants and thermodynamic parameters of ssDNA–RPA interactions at 25 °C obtained by SPR and FCS are summarized in

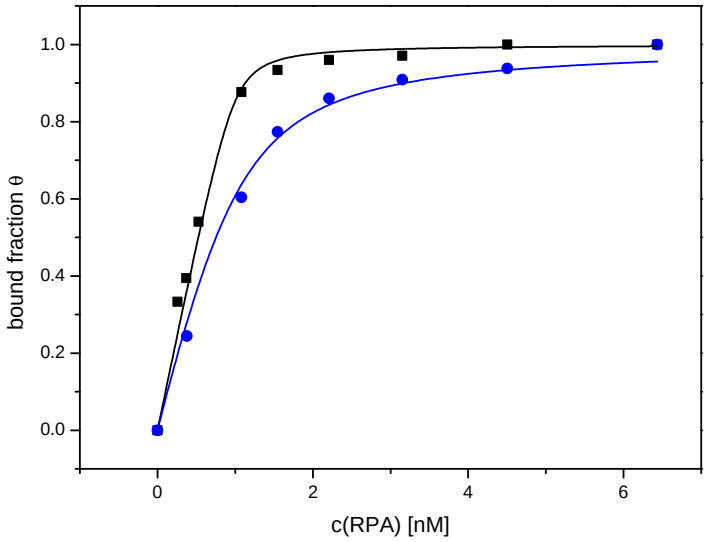

Figure 4.13: Titration curves derived from the autocorrelation functions for a DNA concentration of 1 nM at 10 °C (■) and 25 °C (●).

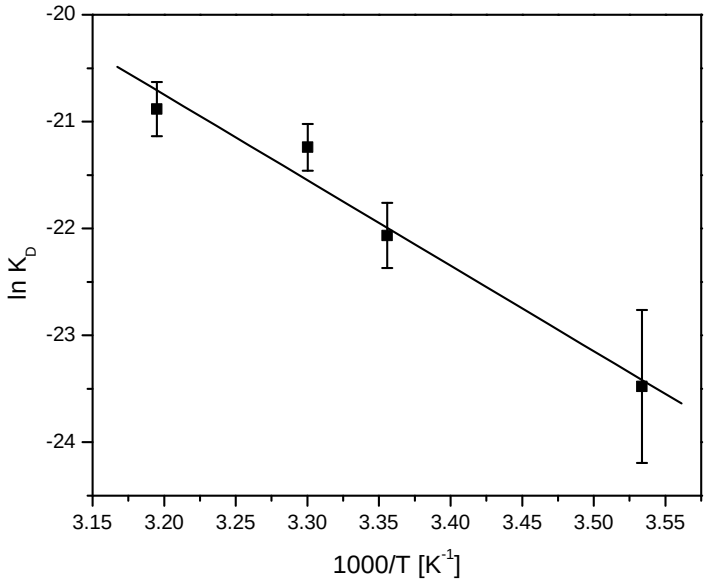

Figure 4.14: van't Hoff plot of the ssDNA–RPA interaction obtained from titration curves at 5 nM DNA concentration.

Table 4.2: Equilibrium constants and thermodynamic parameters of ssDNA–RPA interactions at 25 °C obtained from SPR and FCS experiments.

Method	K_D [M]	ΔG [kJ/mol]	ΔH [kJ/mol]	ΔS [J/mol K]
SPR	1.05×10^{-11}	−62.6	−64.2	−5.4
FCS	2.61×10^{-10}	−54.7	−66.5	−39.6

table 4.2. Within the experimental error, both methods yield the same values for the reaction enthalpy, but different values for the Gibbs free energy. There are clear evidences that the difference in K_D and therefore in Gibbs free energy measured by the two methods is due to different reaction entropies. In SPR the reaction is restricted to two dimensions due to immobilization of the DNA molecules to the sensor surface. In contrast, FCS is able to follow complex formation without spatial restrictions. In consequence, the reaction in three dimensions is entropically less favourable than the reaction at the solid liquid interface. This might be due to differences in the cratic entropy between the two geometries, however, the role of hydration can not be assessed by this experiments.

4.3.4 FCCS: DNA Hybridization

The kinetics of the hybridization of different ssDNA to dsDNA depends on the amount of hydrogen bonds formed during the hybridization process. Therefore, the binding kinetics is supposed to be substrate dependent. Using the oligonucleotides given in table 2.1, it was tested if the damage sites formed during the hybridization has any influence on the kinetics. This process was followed using FCCS. For the cross-correlation experiments an Ar-laser with 50 mW power at 488 nm and a HeNe-laser with 5 mW power at 633 nm were focused into the solution. A 70 μm pinhole was used in the blue and a 90 μm pinhole was used in the red confocal detection channel. The focus of the lens was placed 50 μm above the surface of the cover slide of the sample chamber.

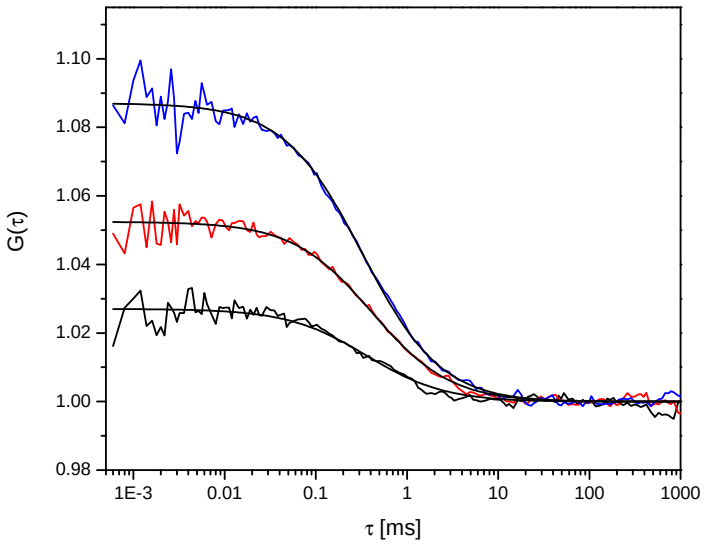

Figure 4.15: Cross-correlation curves and fits for the hybridization of simple dsDNA with a length of 58 bp. Curves are shown for 5 min (—), 30 min (—), and 192 min (—).

The cross-correlation curves at various times at 20 °C for the hybridization of ssDNA strands forming the simple dsDNA are shown in figure 4.15. The amplitude is increasing over time, showing an increase of particle numbers N_{GR} carrying both fluorophores (Alexa488 and Atto647), hence indicating the formation of dsDNA. The obtained curves are rather noisy, due to a low signal-to-noise ration in the cross-correlation channel. The signal quality may be increased by longer integration times. Taking a closer look at the two autocorrelation channels and the cross-correlation channel (figure 4.16), it has to be noted that the diffusion time in the cross-correlation channel is higher than the diffusion time in the red autocorrelation channel. The theory states that for a perfectly aligned system the diffusion time of the cross-correlation curve is the average of the two diffusion times of the autocorrelation curves. The observation therefore points to a not perfectly aligned setup (see section 4.2.3). In the case of foci displacement, not only the diffusion time is increased but also the amplitude is decreased. The measured number of double-labelled particles

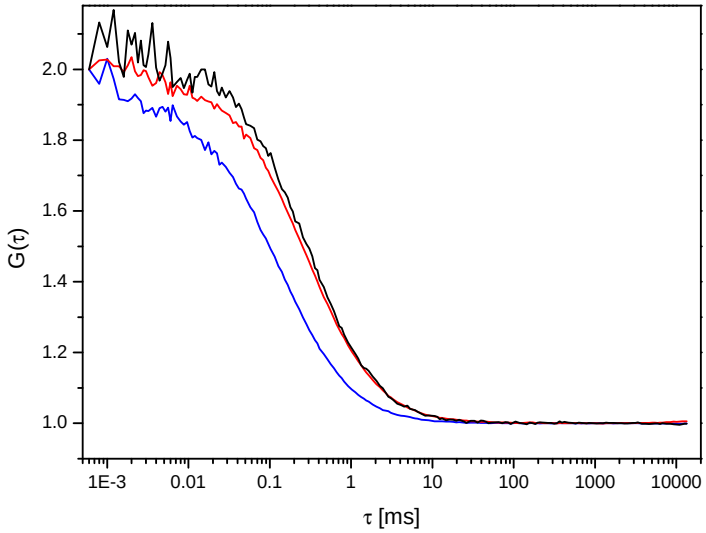

Figure 4.16: Comparison of the two autocorrelation channels and the cross-correlation channel. Blue autocorrelation channel (—), red autocorrelation channel (—), and the cross-correlation channel (—). It has to be noted that the diffusion time in the cross-correlation channel is higher than the diffusion time in the red autocorrelation channel.

does not correspond to the true number of particles. But as long as the setup is not changing during the experiment, the amplitude is still a measure for the relative change in particle numbers. Therefore, the binding kinetics is still accessible by cross-correlation analysis. It is not possible to get any information about the absolute concentration of dsDNA, so the efficiency of the hybridization process is not known.

The hybridization kinetics for three different dsDNA fragments (figure 2.1) are depicted in figure 4.17. The increase in particle numbers in the cross-correlation channel can be evaluated using a second order kinetics with the same starting concentration of the two ssDNA strands

$$[P] = \frac{[A]_0^2\, k\, t}{1 + [A]_0\, k\, t} \tag{4.30}$$

where $[P]$ is the concentration of the dsDNA, $[A]_0$ is the starting concentration of both ssDNA strands, and k represents the rate constant

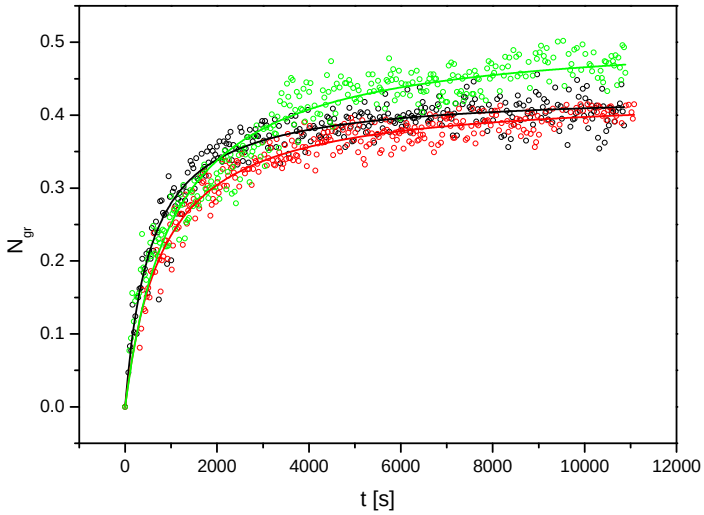

Figure 4.17: Increase of the number of particles during the hybridization of three different dsDNA fragments, Simple (○), Bulge (○), and Bubble (○). The obtained data were evaluated using a second order kinetics fit (equation (4.30)).

for the hybridization process. The evaluation of the hybridization processes of the three dsDNA fragments yielded the following rate constants: $k_{\text{Simple}} = 4.24 \pm 0.17 \times 10^{-3}\,{}^{1}/_{\text{Ms}}$, $k_{\text{Bulge}} = 2.80 \pm 0.12 \times 10^{-3}\,{}^{1}/_{\text{Ms}}$, and $k_{\text{Bubble}} = 1.86 \pm 0.06 \times 10^{-3}\,{}^{1}/_{\text{Ms}}$. The rate of the reaction decrease, the more mismatches are occurring in the dsDNA fragment. This gives evidence that the formation of dsDNA depends strongly on the amount of hydrogen bonds formed.

If one wants to check if the assumed second order kinetics is correct, the data can be evaluated using

$$\frac{1}{[A]_0 - [P]} = k\,t + \frac{[A]}{[A]_0\,([A]_0 - [P])} \tag{4.31}$$

Plotting $\frac{1}{[A]_0-[P]}$ versus t should therefore lead to a linear behaviour. As it can be seen in figure 4.18 the data (taken from figure 4.17) follow a linear behaviour, so the assumption of a second order kinetics with same concentrations of the two ssDNA strands seems to be valid. The scattering of data points for long time scales is due to the very small difference

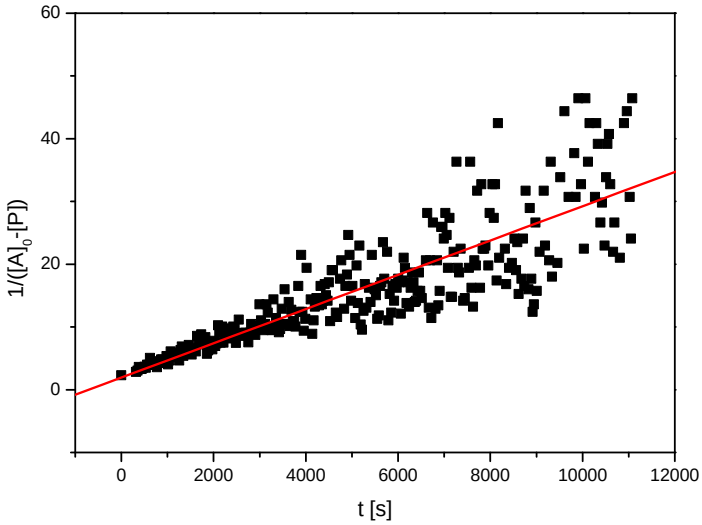

Figure 4.18: Linear fit for the data of the hybridization of dsDNA with a bulge. The data follow a linear behaviour, therefore the assumption of a second order kinetics is valid. The scattering of data points for long time scales is due to the very small difference between the concentration of dsDNA $[P]$ and the starting concentration of the ssDNA $[A]_0$.

between the concentration of dsDNA $[P]$ and the starting concentration of the ssDNA $[A]_0$. The value of $k_{\text{Bulge}} = 2.73 \pm 0.1 \times 10^{-3}\,{}^{1}/_{\text{Ms}}$ is in very good agreement with the result obtained by the non-linear evaluation.

The results of the hybridization experiments clearly show that the two foci are not perfectly adjusted, but reveal a displacement as discussed in section 4.2.3. The displacement leads to an increase in the diffusion time, and a decrease of amplitude, which directly correlates to a decrease of observed particle numbers. As a consequence, the ConfoCor 2 does not seem to be suitable for cross-correlation experiments, although relative changes can still be evaluated.

4.3.5 MCM

The last part of the FCS studies covers the binding process of MCM to DNA. It is not known if the structure of the DNA substrate has any influ-

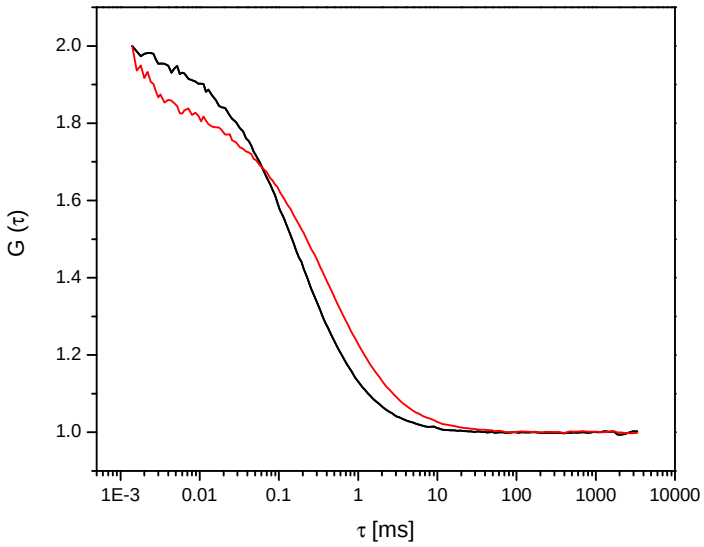

Figure 4.19: Normalized autocorrelation curve for the binding of MCM to simple dsDNA (—). The MCM concentration was 1.5 μM. Due to the complex formation the diffusion time increases from 180 μs for free dsDNA (—) to 450 μs. The theoretical diffusion time for a 1:1 complex would be 430 μs. The same behaviour was found for bubble dsDNA and dsDNA with a tail.

ence on the binding process, therefore different DNA strands were used: a 58-mer, simple and bubble dsDNA and dsDNA with a tail. As it is illustrated in figure 4.19, the diffusion time increases from 180 μs for the free simple dsDNA to 450 μs due to complex formation. The theoretical diffusion time for a 1:1 complex consisting of an MCM hexamer and dsDNA would be 430 μs. Complex formation was also observed for the 58-mer, bubble dsDNA and dsDNA with a tail. From the diffusion time one can not tell if the complex is formed by a hexamer or by 6 to 8 monomeric MCM subunits. In order to gain information about the structure one has to perform AFM or cryo-TEM experiments (see section 5.2.4).

5 cryo-Transmission Electron Microscopy

Transmission Electron Microscopy (TEM) is potentially one of the most useful techniques in the study of microstructured fluid systems like biomolecules in solution. The technique provides high-resolution (of the order of 1 nm) direct images [Tal96a], thus data interpretation is not model-dependent, although it does require full understanding of the mechanism of image formation and the physics of the interaction between the electron beam and the specimen. Direct images can also be recorded by other techniques like Atomic Force Microscopy (AFM). However, this technique does not produce real images in the sense of optics. The TEM is an 'optical microscope', meaning that it produces images as a result of an electron beam passing trough an optical system (consisting of electromagnetic lenses), which produces a Fourier transform of the object (a diffraction pattern) and an inverse Fourier transform, the image. Another drawback of AFM in contrast to cryo-TEM is the immobilization of the biomolecules to a surface. The interaction with the surface leads to a loss of one degree of freedom, because the deposition onto a surface is a transition from three dimensions to two dimensions. This can lead to conformational changes.

5.1 Experimental Setup

5.1.1 Fixation Techniques

The use of transmission electron microscopy in the study of liquid systems is not straightforward. The TEM operates at high vacuum, typically

better than 10^{-5} Pa (necessary for preventing electron scattering in the gas phase). Also, any motion on the supramolecular level, which results in blurred images, must be avoided. As a result any fluid system to be examined in the TEM requires fixation to reduce its vapour pressure and arrest motion.

Fixation may be achieved by either chemical or physical means. In chemical fixation, a chemical compound is added to the original samples. Such compound may selectively adsorb to certain parts of the specimen, thus stabilizing them. In some cases a true chemical reaction takes place between the fixative and the specimen. The fixative can also act as a stain to improve image contrast due to its heavy elements. Frequently used stains are uranyl acetate and phosphotungstic acid. The addition of alien compounds to the investigated system may lead to the formation of a new material system, thus the implications of adding a fixative or a stain to the system should be taken into consideration. Drying the specimen to rid it of volatiles usually follows the addition of the chemical. Drying obviously may also alter the investigated system. Staining and drying have been shown to induce artefacts, and cause microstructural rearrangement in electron microscopy samples of complex liquids [Tal83].

Instead of chemical fixation, one can use physical fixation. Practically this means thermal fixation, namely, ultra-fast cooling (rate 10^6 K/s) of the liquid to a solid or a quasi-solid (vitreous) state. Thermal fixation eliminates the need for addition of chemicals. When thermal fixation is sufficiently rapid, the sample is vitrified, and its original microstructure is preserved. Water molecules, which have high tendency to rearrange into hexagonal crystalline solid, serve in effect as built-in indicator to the success of thermal fixation and vitrification of the sample: if the water is vitrified, then, in all probability, the heavier molecules of other components in the solution have not rearranged [Tal96].

5.1.2 Sample Preparation and Imaging

Samples for direct-imaging cryo-TEM were prepared at room temperature and a humidity of $\sim 45\,\%$. A drop of liquid solution was applied onto a TEM copper grid (bare grid G600HH and lacey grid, Science Services, München; quantifoils R2/2 Quantifoil, Jena), held by tweezers. The drop is then blotted with filter paper to form a thin liquid film (to a thickness of 50-300 nm), and immediately plunged into liquid ethane at its freezing temperature (-183 °C). The vitrified specimen is then stored under liquid nitrogen (-196 °C), until it is transferred to the microscope. The vitrified specimens were observed in a Gatan sample holder in a Zeiss 922 transmission electron microscope, operated at 200 kV, equipped with an in-column Ω-filter for energy filtering. Specimens were first tempered in the microscope at about -180 °C for 30 min, and examined in the low-dose imaging mode. Images were digitally recorded with a Gatan UltraScan 1000 CCD camera using the Gatan Microscopy Suite 1.4 software package. Image processing (background subtraction, filtering) was performed using the Digital Micrograph 3.6 package.

A part of this work was performed in the group of Prof. Talmon at the Technion, Haifa, Israel. The sample preparation followed a different protocol and the imaging was performed on a different instrument. To avoid water loss from the specimen during preparation the specimens were prepared in the controlled environmental vitrification system (CEVS) [Bel88], at 25 °C and relative humidity of 100%. The vitrified specimens were observed in an Oxford CT3500 cooling holder in a Philips CM120 transmission electron microscope, operated at 120 kV. Specimens were first equilibrated in the microscope at about -180 °C for 30 min, and examined in the low-dose imaging mode. Images were digitally recorded with a Gatan 791 MultiScan CCD camera using the Digital Micrograph 3.1 software package. Image processing was performed by the Adobe Photoshop 5.0 package.

Difficulties

There are several difficulties associated with the cryo-TEM technique and sample preparation:

Ice Although the described specimen preparation method produces vitreous water, occasionally reduced cooling rates may lead to formation of cubic or hexagonal ice. These forms of crystalline ice may lead to optical artefacts, and mechanical damage to the microstructure due to the effect of the moving freezing front, and the forming of the ice matrix. Also, in many cases defects in crystalline ice obscure the microstructures to be visualized [Tal99]. Another advantage of vitreous water relative to crystalline ice is that electron beam radiation damage is more severe at the interface of organic material with crystalline ice than with vitreous water [Tal87].

Contrast Contrast is defined as the relative difference in intensity between two adjacent areas [Wil96]. Two main types of contrast may arise in transmission electron microscope image: amplitude contrast and phase contrast. Amplitude contrast, also called mass-thickness contrast, results from density and thickness differences from one sample area to another, which leads to loss of electrons, scattered outside of the objective aperture. It can be improved by staining. Phase contrast is produced by the interference of the scattered electrons, which passes through the objective aperture, and the unscattered electron wave. Phase contrast becomes dominant for very small or thin objects with light atomic number. Changing the objective lens defocus changes the phase contrast enhancement for structural features with different spacing. Thus, it is possible to choose a certain defocus, to obtain maximum phase contrast for a spacing in the specimen. However, changing the defocus may lead to filtering out certain spatial frequencies (details of certain sizes), while overemphasising others, leading to loss of resolution and possible overall distortion of the true microstructure. To avoid focus related artefacts one needs to

record a series of images at increasing underfocus to assess its effect on the recorded images.

Specimen Thickness TEM specimens of liquid systems have to be quite thin. Thin films are required due to limited penetration power of the electron beam and in order to prevent multiple scattering, which blurs the image. Another reason for thickness limitation is that a large surface-to-volume ratio is essential for high cooling rates necessary. Thick specimens also make image interpretation more difficult because of superposition of information. To obtain thin film specimen, the drop of sample is blotted with filter paper. However, this blotting step applies very high shear and elongation stress on the specimen microstructures.

Shear and Elongation High shear rates applied on the specimen film may cause changes in the microstructures like alignment of structures [Cla92], and distortion of aggregates into their components.

Radiolysis Electron beam radiation damage, or radiolysis, is an inevitable consequence of electron beam-specimen interaction. It is the result of radical chain reactions started by ionization of specimen molecules and ice molecules by the high-energy electron beam. Because ice is a good source of small, very mobile, free radicals, radical chain reactions are much faster in its presence than in the case of dry specimens. Free radical reactions cause mass loss, scission and some mass rearrangement in both ice and sample molecules. This is especially severe when the sample contains organic molecules, such as biological specimen. In some cases one can take advantage of this effect by careful contrast enhancement through selective etching. Radiolysis can be reduced by using vitrified specimens, and low-dose operation mode (less then 10 electrons per $\mathrm{\AA}^2$).

Surface Contamination Cryo-specimen artefacts can arise from surface contamination, which can occur by water vapour deposition during

specimen transfer from the liquid nitrogen to the microscope or by condensibles in the microscope column.

In summary when preparing direct imaging cryo-TEM specimen, one has to take into account rapid cooling for artefact-free thermal fixation, thin enough specimens, and careful but rapid specimen transfer to the microscope. When the specimen contrast is low, proper defocus may carefully be used.

5.2 Results

In contrast to AFM, cryo-TEM offers the opportunity to image biomolecules without the influence of a surface. In the case of cryo-TEM the biomolecules drying and staining can also be avoided. Therefore conformational changes, as they might occur in AFM experiments due to the influence of the surface, are not introduced.

5.2.1 λ-DNA

The imaging of small DNA molecules is very difficult, finding the right conditions (concentration, electron dose, defocus) is very tedious. In order to simplify finding these conditions, in a first step larger DNA molecules (λ-DNA) were imaged. Long and thin structures can be percepted much easier by the human eye than short and thin structures. Figure 5.1 A shows cryo-TEM micrographs of unstained λ-DNA on a lacey grid. The uncondensed DNA tertiary structure, at a highly elongated state, can be observed. From the images one finds a DNA diameter of 2 nm, as expected from AFM experiments. A very interesting feature is that the DNA bundles on the perforated carbon support film. These bundles were observed whenever the DNA crosses the carbon film. In 'free solution' (no perforated carbon film) and without shear forces, the DNA can be imaged in a spaghetti-like structure, e.g. the DNA molecules are entangled (figure 5.1 B).

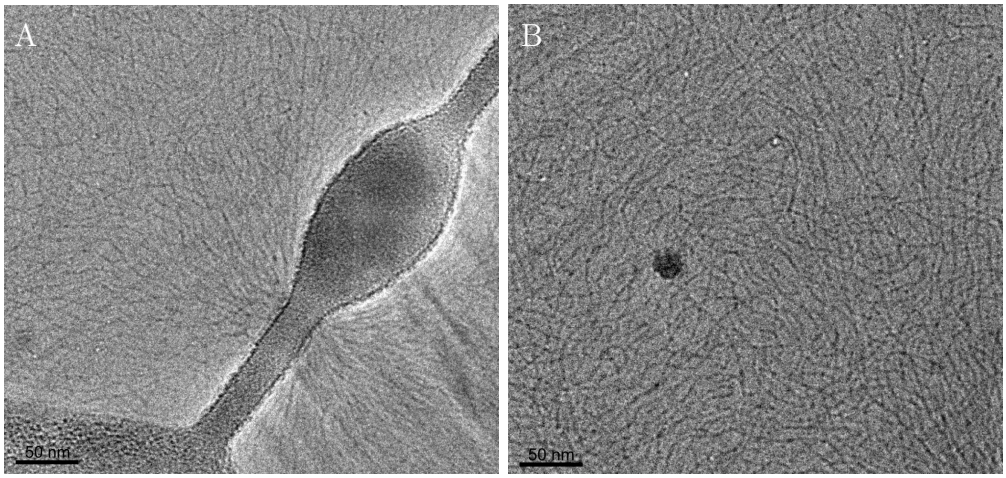

Figure 5.1: Cryo-TEM image of λ-DNA. (A) DNA bundles formed on the perforated carbon film are clearly visible. (B) In 'free solution' (no perforated carbon film) and without shear forces, the DNA can be imaged in a spaghetti-like structure, e.g. the DNA molecules are entangled. The scale bar corresponds to 50 nm.

As mentioned in section 5.1.2, shear forces occur during the blotting process. High shear rates applied on the specimen film may cause changes in the microstructures like alignment or elongation. Large persistence lengths, clearly larger than 50 nm, have been observed for λ-DNA (figure 5.2). This may be a result of the blotting, used in the sample preparation, which can apply high shear and elongational stress on the specimen microstructures, and as a result increase their persistence length. In addition, the DNA molecules are confined to a thin layer of solution approximately 50-250 nm in thickness. As the length of the molecule exceeds the thickness of the thin layer (such as in the case of λ-DNA) this confinement may cause the molecules to be partially flattened and stretched.

Because DNA is made mostly of relatively light atoms, its mass-thickness contrast is low. As a result it can be clearly visualized only when the vitrified sample is clean, thin, and by using optimal objective lens underfocus. A different way of overcoming DNA low contrast is enhancing its mass-thickness contrast with stains. Uranyl acetate and phosphotungstic acid

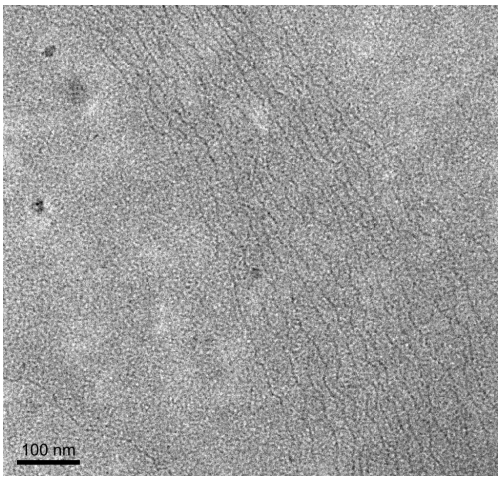

Figure 5.2: Cryo-TEM image of λ-DNA under shear. As mentioned above, shear forces lead to an alignment and increase of the persistence length of the DNA molecules. The scale bar corresponds to 100 nm.

were used in some experiments (images not shown). A major disadvantage of staining the DNA is a change in structure and therefore in biological activity. Stained DNA strands have clearly a shorter persistence length than unstained strands [Kon04]. For the interactions of DNA with RPA, staining is not the ideal method for increasing the contrast, because the staining agent may have an influence on the binding process.

5.2.2 Influence of UV-light on undamaged DNA

As seen in the previous section, it is, with some difficulties, possible to image long DNA fragments using cryo-TEM. In order to compare the AFM results obtained by M. Lysetska [Lys02, Lys04], now shorter DNA fragments with a length of 538 bp are used. This is even more difficult, due to a much lower mass contrast compared to the λ-DNA. Therefore, the image quality is worse.

It is know from AFM experiments that the DNA forms kinks and globular structures upon UV irradiation. Irradiating dsDNA with UV light leads, depending on the dose of irradiation, to structural changes of the

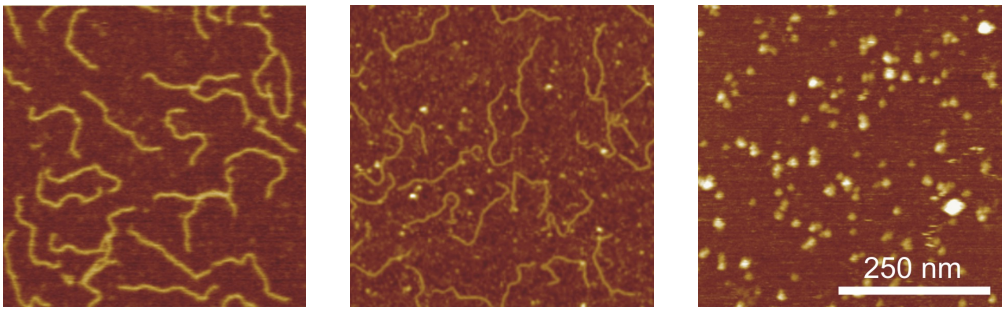

Figure 5.3: Influence of UV-light on 538 bp DNA. AFM images of DNA after 0 min, 20 min, and 40 min of UV light exposure. Knot like structures appear on the DNA as a result of UV-damage. After 40 min of UV light exposure the rod like molecules are vanished [Lys02].

DNA. Very frequent globular structures along the DNA strand and sharp kinks in the DNA chain are observed (figure 5.3), which are not present prior to UV treatment. Both findings could correspond to the presence of single-stranded regions within the dsDNA strand [Riv98].The formation of globular objects suggest that the ssDNA regions tend to coil.

A typical consequence of direct UV absorption is dimerization of the rings of adjacent thymines. This cannot explain the presence of ssDNA. The breakage of the dsDNA into ssDNA can therefore only be explained by the reaction of hydroxyl radicals formed from water by UV irradiation [Fol02, Hor01].

In order to check whether the kinks are resulting from the UV-damage of the DNA or are induced by the interaction of DNA with the mica surface, the DNA was imaged in 'free solution' by the means of cryo-TEM. It was expected to see kinks also in the cryo-TEM experiments, but they occurred only rarely. There might be two reasons for this: First, the kinks in the AFM experiments are induced by the mica surface and therefore do not occur in cryo-TEM experiments. Second, the resolution of the TEM is not as good as in AFM, therefore, the kinks can not be seen in the TEM. In Fig. 5.4 an example for damaged DNA is shown. The DNA has no tendency to stick to the edges of the grid.

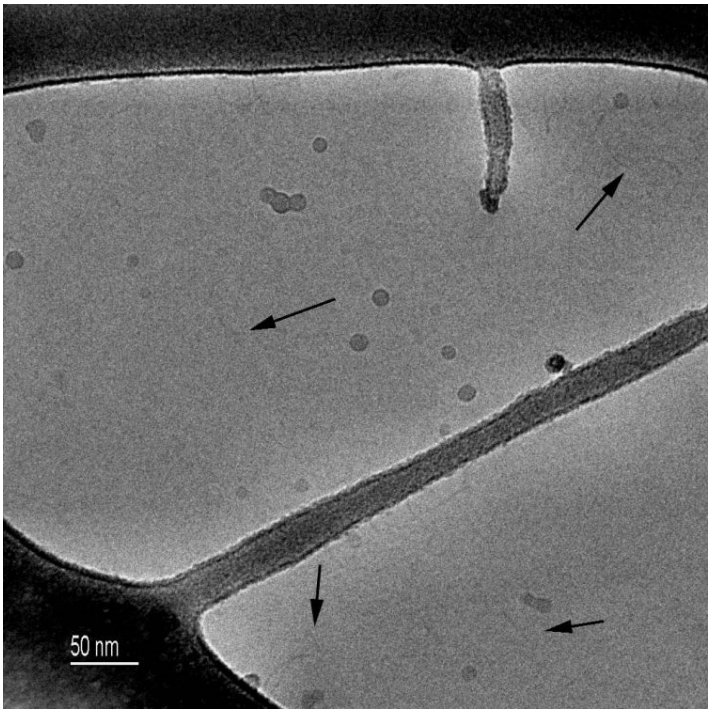

Figure 5.4: Micrograph of UV-damaged DNA. From the AFM experiments it was expected to see kinks, but they occurred only rarely. There might be two reasons for this: First, the kinks in the AFM experiments are induced by the mica surface and therefore do not occur in cryo-TEM experiments. Second, the resolution of the TEM is not as good as in AFM, therefore, the kinks can not be seen in the TEM. The scale bar corresponds to 50 nm.

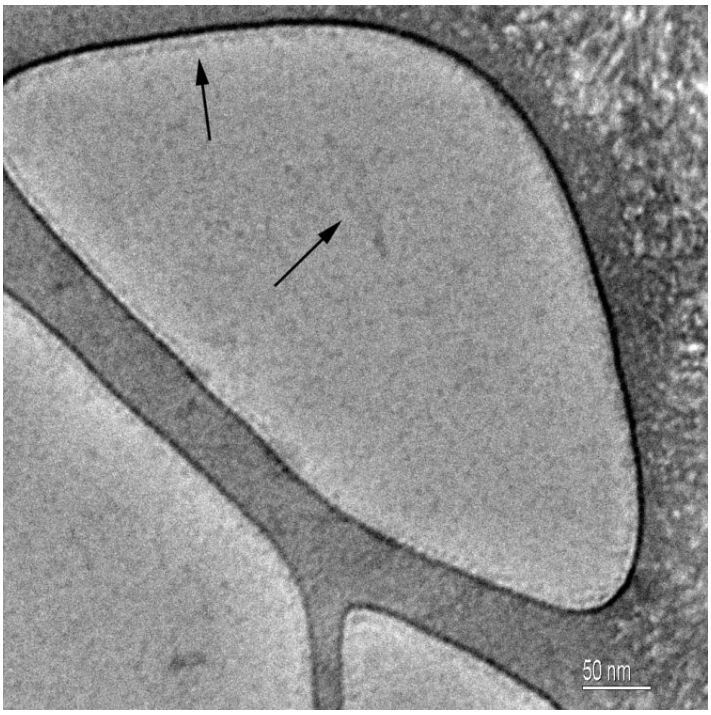

Figure 5.5: RPA imaged by cryo-TEM. The RPA is found to attach strongly to the carbon film. This may be due to hydrophobic interactions between the protein and the polymer. The scale bar corresponds to 50 nm.

5.2.3 Interaction between DNA and RPA

In order to see how the RPA behaves in a vitrified sample, only the protein is imaged on a perforated carbon film. The RPA is found to attach to the edges of the carbon film (see Fig. 5.5). This is due to hydrophobic interactions of the protein with the polymer. Using bare grids one can avoid this behaviour (data not shown).

Complexes of RPA with undamaged DNA

Complexes between undamaged DNA and RPA occurred very rarely (only at higher RPA concentrations), as expected from the AFM experiments. The addition of RPA to undamaged DNA did not lead to any structural change. Only in very few cases terminal binding of RPA to DNA could be

observed (figure 5.6). Since RPA is known to have a high affinity to single-stranded DNA [Wol97], this finding may be explained by the binding of RPA to unpaired nucleotides at the end of the dsDNA.

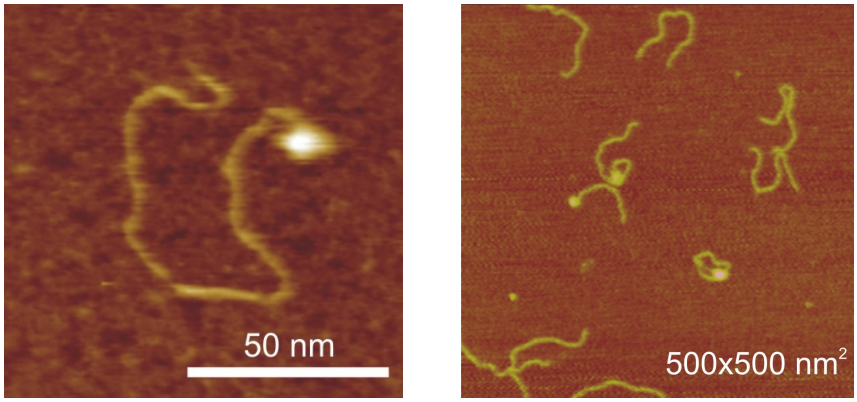

Figure 5.6: Interaction of RPA with undamaged DNA. The AFM images do not show any distinct complex formation. Randomly cases of terminal binding occurred [Lys02, Lys04].

In cryo-TEM experiments complexes with the protein bound along the chain were not observed. One complex is seen in Fig. 5.7. In this case, both ends of the DNA are split up and the protein connects both ends of the DNA. This behaviour was also found in AFM experiments. In figure 5.8, another interesting feature is illustrated: it seems as if the DNA grafts from the carbon film. Reason for this is, that the DNA binds to the protein attached to the edges of the carbon film. When using bare grids, the DNA is not found to stick to the the grid.

Complexes of RPA with UV-damaged DNA

The addition of RPA to undamaged DNA leads to almost no change in the appearance of the DNA molecules, as shown by the means of AFM and cryo-TEM. However, the situation is quite different for UV-damaged DNA. When adding RPA to damaged DNA in 40-fold excess, the mass contrast of the specimen increased. Globular objects are sitting on the

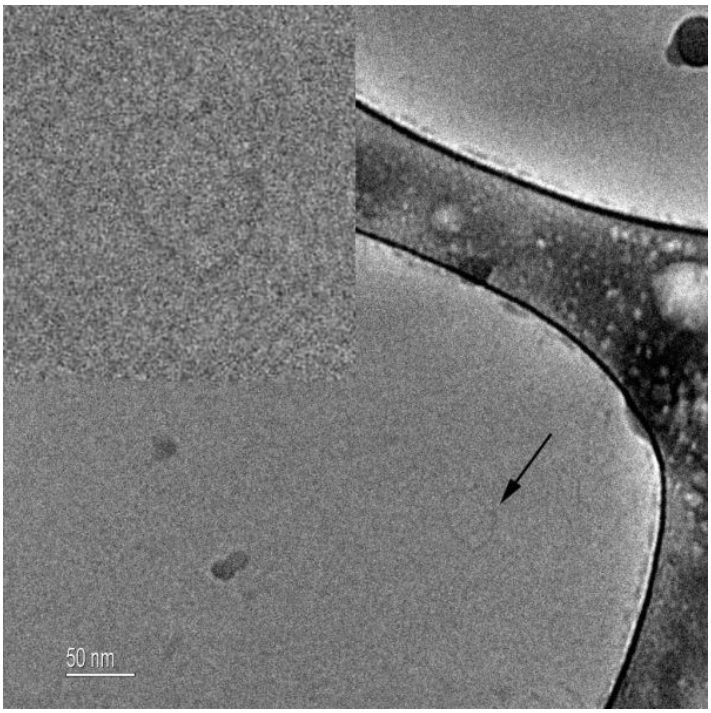

Figure 5.7: Interaction of RPA with undamaged DNA as obtained by cryo-TEM. The micrograph does not show any distinct complex formation. Randomly cases of terminal binding occurred. In this case both ends of the DNA are split up and the protein connects both ends of the DNA. The scale bar corresponds to 50 nm.

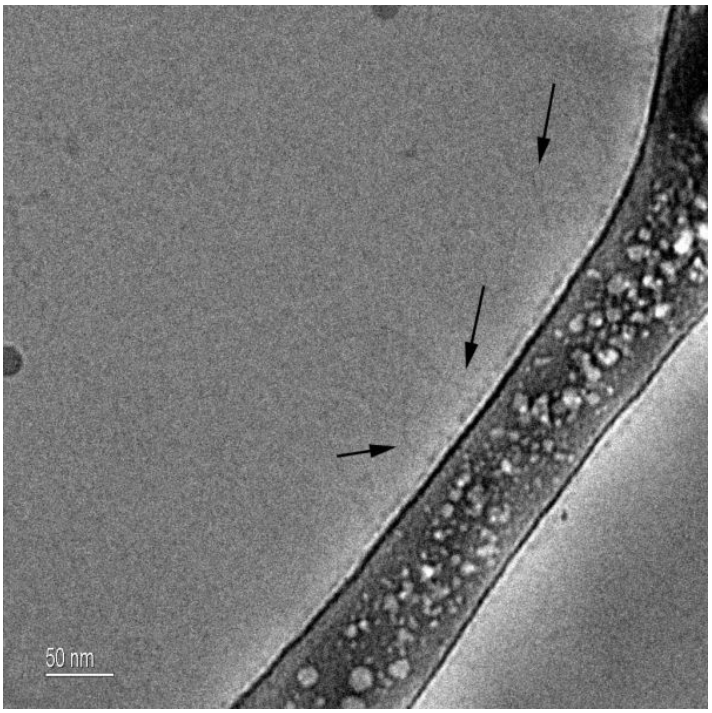

Figure 5.8: Interaction of RPA with undamaged DNA as obtained by cryo-TEM, showing the interaction of the DNA strands with RPA attached to the edges of the carbon film. The scale bar corresponds to 50 nm.

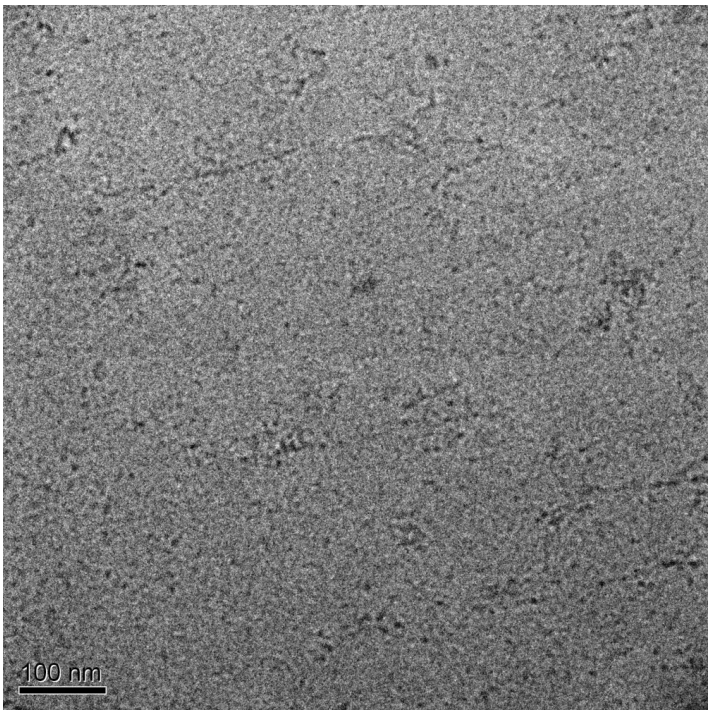

Figure 5.9: DNA–RPA complexes obtained from UV-damaged DNA. The mass contrast of the specimen is increased, thus RPA can be used as a biological stain in cryo-TEM when imaging damaged DNA. The scale bar corresponds to 100 nm.

rod-like DNA molecules and can also be found as free particles in the vitrified sample, as illustrated in figure 5.9. Thus RPA can be used as a biological stain in cryo-TEM samples to visualize damaged DNA.

During the preparation of a thin film thickness gradients may occur. This thickness gradient results in a size exclusion of particles. Therefore proteins and DNA–protein complexes can be sorted. In thin film regions, the protein alone can be observed, in thicker regions the protein and complex can be found. This behaviour is nicely illustrated in figure 5.10. One can even find areas, where the film is so thin, that even the small protein is not found. One can use these images containing a thickness gradient for the determination of the size of the RPA. By measuring the diameter of many RPA molecules, one receives a diameter of 5.7 nm.

In AFM experiments globular objects sitting on DNA molecules can be

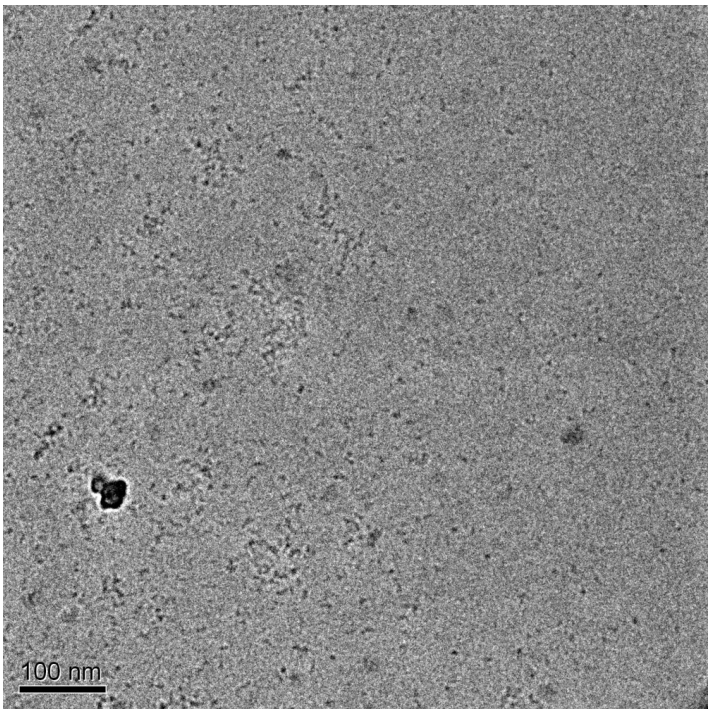

Figure 5.10: DNA–RPA complexes in a vitrified film with a thickness gradient. In thin film regions (right part of the image), only the RPA or even no molecule can be observed. In areas with a thicker film, both RPA and DNA–RPA complexes are found. The scale bar corresponds to 100 nm.

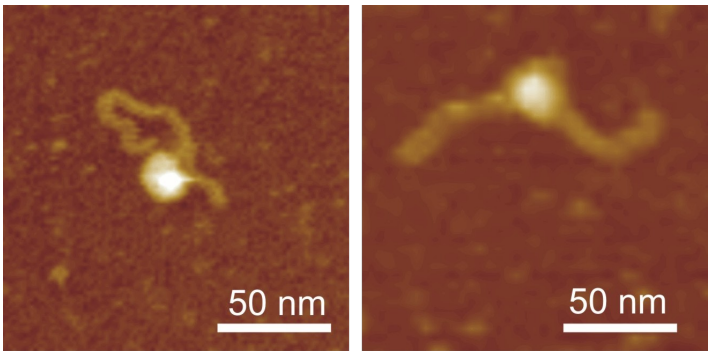

Figure 5.11: Interaction of RPA with UV-damaged DNA. The DNA shows a shortening of the DNA contour length, and it seems as if the DNA makes a distinct turn around the protein [Lys02].

observed (figure 5.11). It is suggested that the DNA molecules form loop-like structures around the globular protein. Comparing the contour length of free DNA and DNA in DNA–RPA complexes, one finds a significant decrease in the apparent contour length. The contour length distributions and the mean values of the Gaussian fit are depicted in figure 5.12. After complex formation, the apparent DNA contour length is decreased by approximately 28 nm compared to the contour length of UV-damaged DNA under the same conditions. This phenomenon can be explained by a model where the DNA is wrapping around the RPA [Lys02]. Coiling around the protein would require $\Delta L = \pi(d_{\mathrm{RPA}}+d_{\mathrm{DNA}}) = 27\,\mathrm{nm}$, when $d_{\mathrm{RPA}} = 6.5\,\mathrm{nm}$, and $d_{\mathrm{DNA}} = 2\,\mathrm{nm}$. The diameter of RPA found by cryo-TEM and AFM are in good agreement.

Quantitative results on the stoichiometry of the complex could not be achieved from the cryo-TEM micrographs, as it is not possible to distinguish between RPA subunits and protein molecules. It can not be excluded, that the complexes are composed of more than one RPA molecule, due to the cooperativity of the binding [Kim94, Kim95]. Some studies revealed a binding of a single RPA heterotrimer to a damaged site [Hey01], and it is therefore assumed that the globular objects seen in cryo-TEM images represent single RPA molecules.

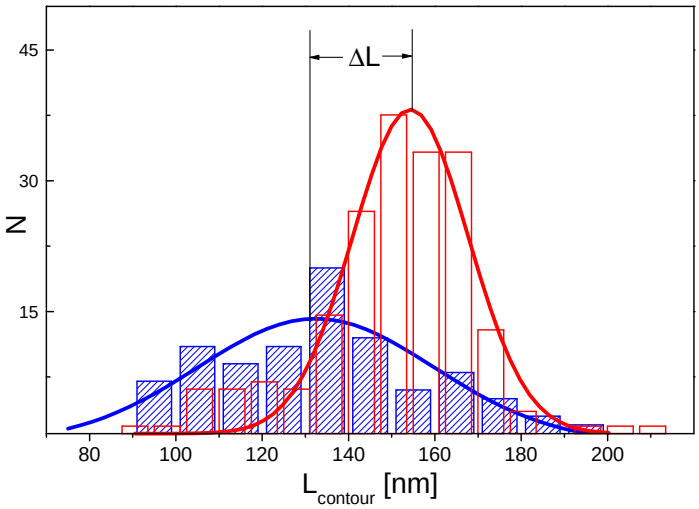

Figure 5.12: Contour length distributions evaluated from AFM images. Empty bars correspond to DNA exposed to UV light for 30 min; filled bars correspond to the same DNA measured in DNA–RPA complexes. The lines represent a Gaussian fit for the distribution. A decrease in contour length ΔL occurs upon binding to RPA [Lys02].

From AFM experiments a model was stated where the DNA forms loop-like structures around the RPA. Unfortunately, this model could not be verified, due to the much lower resolution of cryo-TEM compared to AFM.

5.2.4 Mini-Chromosome Maintenance

The Mini-Chromosome Maintenance protein was also imaged using cryo-TEM. In the images a structure as expected from previous TEM experiments can be seen (figure 5.13. The protein has a diameter of $\sim$ 13 nm, showing a hole in the middle. Some of the molecules are open rings, even a dimer can be observed. The opening is probably due to the shear forces applied to the molecules during the blotting process. So far it is not known, if the MCM binds as a dimer to DNA, therefore the dimer found may not only an artefact, but can also be the binding conformation. Unfortunately, micrographs of MCM–dsDNA complexes could not be obtained so far. The

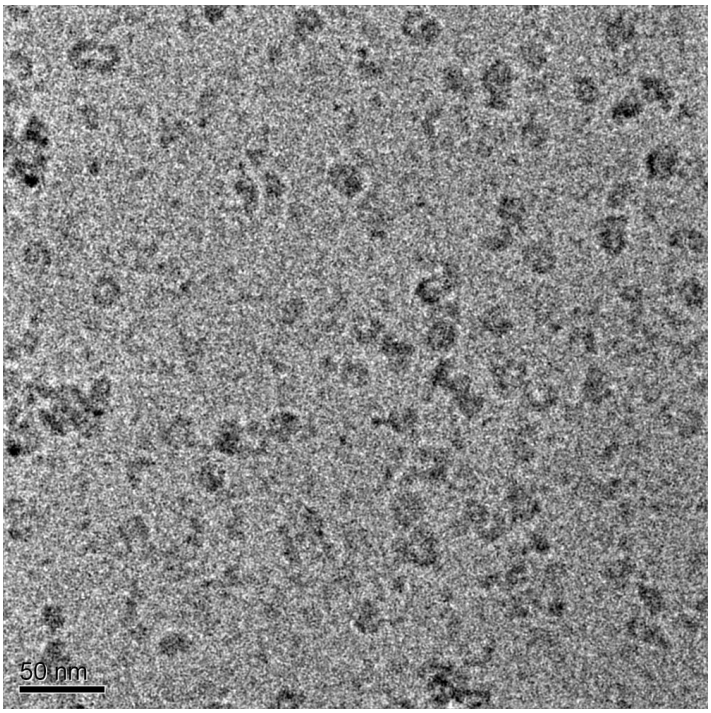

Figure 5.13: cryo-TEM image of the Mini Chromosome Maintenance protein. The protein has a diameter of ~ 13 nm, showing a hole in the middle. The scale bar corresponds to 50 nm.

question about the structure of the complex is therefore still not answered.

6 Summary

In this work the two spectroscopic techniques surface plasmon resonance (SPR) and fluorescence correlation spectroscopy (FCS) as well as the imaging technique cryo-transmission electron microscopy (cryo-TEM) were used to gain kinetic, thermodynamic and structural information about DNA–protein interactions. Furthermore, the micrographs obtained by cryo-TEM were compared to AFM images taken in a previous work [Lys02, Lys04]. The main goal of this work was to investigate the influence of surfaces on DNA–protein interactions, therefore the methods mentioned above were chosen. Both SPR and AFM deal with molecules attached to a surface, whereas FCS and cryo-TEM monitor the molecules in free solution. As a suitable model system the well characterized interaction between the human replication protein A (RPA) and DNA was chosen.

The application of SPR and FCS to analysing the binding of RPA to ssDNA yields information about the kinetics and thermodynamics. No modification of the protein is required and biotinylated and fluorescently labelled DNA strands are available from commercial sources. Salt concentration, pH and temperature can be varied over a wide range. This has been demonstrated here by measuring the kinetics and thermodynamics in a temperature range from 10 °C to 40 °C.

A number of studies have been published utilizing SPR to reveal the kinetics and thermodynamics of interactions between various proteins, including RPA, and DNA [Wan00, Sei96, Buc01, Chu01, Ima02, Rüf02, Yan02]. The kinetic data obtained by SPR for the formation of a ssDNA–RPA complex are comparable to values reported in literature [Wan00]. The values found for the rate constants and the equilibrium constant are slightly deviating from the reported values for a 70-mer ssDNA. This length dif-

ference may well be the reason for the discrepancy, as the binding process is known to depend on the length of the DNA. To best of our knowledge, FCS has not been used previously to obtain equilibrium constants at different temperatures. In this work it was demonstrated how temperature dependent SPR and FCS measurements can be performed and evaluated to determine thermodynamic data of DNA–protein interactions.

Astonishingly, the equilibrium constant K_D for the binding of RPA to ssDNA obtained by FCS is larger than the value obtained by SPR by a factor of 20–25, depending on the temperature. Therefore the values found for the Gibbs free energy were different, whereas the values for the reaction enthalpy were nearly the same for the two methods used. There are clear evidences that the difference in K_D and therefore in Gibbs free energy measured by the two methods is due to different reaction entropies. In SPR the reaction is restricted to two dimensions due to immobilization of the DNA molecules to the sensor surface, thus the rate constants obtained might not be the true association and dissociation rates. As a main result, the data obtained by SPR differ from the data gained from the free solution experiments. The reason for this is a loss of one degree of freedom, which in turn results in different entropic terms for the surface and the free solution techniques. In contrast, FCS is able to follow complex formation without spatial restrictions. In consequence, the reaction in three dimensions is entropically less favourable than the reaction at the solid-liquid interface. This might be due to differences in the cratic entropy between the two geometries, however, the role of hydration can not be assessed by our experiments.

The picture of the DNA–RPA interaction was completed by further FCS measurements using various dsDNA fragments containing damage sites. The binding of RPA to undamaged dsDNA fragments showed a low affinity to dsDNA ($\sim 15\,\%$), as expected from previous AFM experiments [Lys02, Lys04]. Since RPA is known to have a high affinity to single-stranded DNA, this finding may be explained by the binding of RPA to unpaired nucleotides at the end of the dsDNA.

The FCS cross-correlation experiments clearly showed that the kinetics of the DNA hybridization strongly depends on the number of hydrogen bonds formed during the hybridization process. Using three different ssDNA fragments forming undamaged dsDNA and dsDNA with distinct damage sites (bulge and bubble damage), it was found that the formation of undamaged dsDNA exhibits the fastest kinetics, whereas the kinetics of the two damaged dsDNA yield almost the same value. As a side effect, it was shown that the commercially available FCS system is not perfectly suited for cross-correlation analysis.

Comparing the two imaging techniques AFM and cryo-TEM one does not find a strong influence of the surface on the DNA–RPA interaction. The kinks formed by UV-damaged DNA observed in AFM experiments [Lys02, Lys04] could not be verified by the cryo-TEM experiments. There might be two reasons for this: First, the kinks in the AFM experiments are induced by the mica surface and therefore do not occur in cryo-TEM experiments. Second, the resolution of the TEM is not as good as in AFM, therefore, the kinks can not be seen in the TEM.

The question if the DNA is wrapping around the RPA as stated in earlier works [Lys02, Lys04] can not be answered using cryo-TEM. The resolution of this method is not as good as in AFM. In order to get micrographs with a better resolution one has to perform simple TEM experiments including staining of the molecules. The drawback of this procedure is that the molecules are influenced by the staining chemicals and therefore not in their natural state.

Using cryo-TEM micrographs for statistical analysis with reasonable effort on DNA and DNA–RPA complexes as was done with AFM [Lys02, Lys04] is not possible. To perform a statistical analysis, one has to image at least 100–200 molecules in 3D, which means tilting the sample and taking 5–10 high-resolution images per molecule. In a next step, the obtained images have to be analysed using the appropriate software (e.g. SPIDER [Fra81] or IMAGIC5 [vH81, vH96]) to gain three-dimensional images.

In a very last part of this work the mini-chromosome maintenance com-

plex was investigated using FCS and cryo-TEM. It was shown that the protein exhibits a medium affinity to ssDNA and dsDNA. The structure of the DNA substrate does not play an important role, the interaction was the same for simple and bubble dsDNA and dsDNA containing a ssDNA tail. The research on MCM has to be continued, in order to gain more information about the mechanism of the DNA unwinding process. Again, cryo-TEM can be applied to get 3-D images of the MCM, in order to confirm the proposed structure of the protein [Pap03] in its natural state.

7 Zusammenfassung

In der vorliegenden Arbeit wurden die beiden spektroskopische Methoden Oberflächenplasmonenresonanz (SPR) und Fluoreszenzkorrelationsspektroskopie (FCS) sowie die abbildende Methode cryo-Transmissionselektronenmikroskopie (cryo-TEM) verwendet, um kinetische, thermodynamische und strukturelle Informationen über DNA-Protein-Wechselwirkungen zu gewinnen. Des weiteren wurden die mittels cryo-TEM erhaltenen Bilder mit AFM-Bildern einer früheren Arbeit [Lys02, Lys04] verglichen. Das Hauptziel dieser Arbeit war, den Einfluss von Oberflächen auf DNA-Protein-Wechselwirkungen zu untersuchen, daher wurden die oben genannten Methoden gewählt. SPR und AFM sind oberflächengebundene Techniken, im Gegensatz dazu kann man mit FCS und cryo-TEM die Moleküle in freier Lösung untersuchen. Als Modellsystem wurde die sehr gut charakterisierte Wechselwirkung zwischen dem Replikationsprotein A (RPA) und DNA ausgewählt.

Durch die Anwendung von SPR und FCS für die Analyse der Bindung von RPA und ssDNA erhält man Informationen über die Kinetik und Thermodynamik. Das Protein muss nicht modifiziert werden, biotinylierte und fluoreszenzgelabelte DNA ist kommerziell erhältlich. Die Bedingungen, wie z. B. Konzentration, pH-Wert und Temperatur können über einen weiten Bereich variiert werden, wie die in dieser Arbeit durchgeführten Messungen zeigen. Durch Variation der Temperatur in einem Bereich von 10 °C bis 40 °C konnten die Kinetik und Thermodynamik der Bindung von RPA an ssDNA bestimmt werden.

In einer Vielzahl von Veröffentlichungen findet man die Anwendung von SPR zur Bestimmung von kinetischen und thermodynamischen Parametern für biomolekulare Wechselwirkungen [Wan00, Sei96, Buc01, Chu01,

Ima02, Rüf02, Yan02]. Die kinetischen Daten, die in dieser Arbeit für die Wechselwirkung zwischen RPA und ssDNA gefunden wurden, sind vergleichbar mit den schon veröffentlichten Werten [Wan00]. Die Abweichungen von diesen Literaturwerten lassen sich durch Unterschiede in den verwendeten DNA-Fragmenten (70-mer im Vergleich zu 26-mer) und den Puffern erklären. Besonders die DNA-Länge scheint ein wichtiger Parameter zu sein, da die Bindungskinetik von RPA an ssDNA von der Länge des DNA-Substrats abhängt. Nach dem bisherigen Wissensstand ist FCS noch nicht genutzt worden, um die Gleichgewichtskonstante bei verschiedenen Temperaturen zu bestimmen. In der vorliegenden Arbeit ist es gelungen, die ersten temperaturabhängigen FCS-Messungen durchzuführen. Es wurde gezeigt, wie man SPR- und FCS-Untersuchungen bei verschiedenen Temperaturen durchführen und auswerten kann, um kinetische und thermodynamische Daten von DNA-Protein-Wechselwirkungen zu bestimmen.

Die mittels FCS bestimmte Gleichgewichtskonstante K_D ist überraschenderweise um einen Faktor 20–25 (abhängig von der Temperatur) größer als der mittels SPR erhaltene Wert. Die Werte für die Gibbs-Energie sind für die beiden Methoden unterschiedlich, allerdings finden sich sehr ähnliche Werte für die Reaktionsenthalpie. Der Unterschied, der für K_D und daher auch für die Gibbs-Energie für beide Methoden gefunden wird, lässt sich nur durch unterschiedliche Reaktionsentropien erklären. Im SPR-Experiment sind die DNA-Moleküle an eine Oberfläche gebunden, die Reaktion ist auf zwei Dimensionen beschränkt. Somit kann es vorkommen, dass die erhaltenen Geschwindigkeitskonstanten nicht den wahren Werten entsprechen. Als wichtiges Ergebnis findet man, dass die Daten der SPR-Experimente sich deutlich von den Daten der FCS-Messungen unterscheiden. Der Hauptgrund ist im Verlust eines Freiheitsgrades durch die Immobilisierung zu suchen, daher findet man unterschiedliche Entropie-Anteile für die oberflächengebundene und die oberflächenfreie Methode. Im FCS-Experiment kann die Komplexbildung in freier Lösung untersucht werden, d. h. ohne räumliche Begrenzung. Als Konsequenz ist die Reaktion in drei Dimensionen entropisch ungünstiger als die Reaktion an der Flüssig-

Fest-Grenzfläche. Möglicherweise ist dies durch unterschiedliche kratische Entropien der beiden Geometrien zu erklären, allerdings kann der Einfluss der Hydratation nicht mit diesen Experimenten bestimmt werden.

Das Bild zur DNA-RPA-Wechselwirkung ist durch weitere FCS-Untersuchungen vervollständigt worden, bei denen verschiedene dsDNA-Fragmente mit Schädigungen verwendet wurden. Die Bindung von RPA an ungeschädigte DNA zeigt, dass das Protein nur eine geringe Affinität zu dsDNA hat ($\sim 15\,\%$), wie es von den AFM-Experimenten bekannt ist [Lys02, Lys04]. Da RPA eine hohe Affinität zu Einzelstrang-DNA aufweist, kann man diese Beobachtung durch eine Bindung des Proteins an ungepaarte Nukleotide am Ende der DNA erklären.

Die Messungen mittels FCS-Kreuzkorrelation haben deutlich gezeigt, dass die Kinetik der DNA-Hybridisierung sehr stark von der Anzahl der Wasserstoffbrücken abhängt, die während der Hybridisierung gebildet werden. Bei der Verwendung verschiedener Einzelstrang-DNA-Fragmente, die durch die Hybridisierung ungeschädigte und geschädigte dsDNA erzeugen, zeigte sich, dass die Bildung eines ungeschädigten Doppelstrangs die schnellste Kinetik aufweist; im Gegensatz dazu sind die Hybridisierungskinetiken der beiden geschädigten DNA-Fragmente langsamer. Als weiteres Ergebnis dieser Untersuchungen hat sich herausgestellt, dass das verwendete, kommerziell erhältliche FCS-System für Kreuzkorrelationsexperimente nicht besonders gut geeignet ist.

Vergleicht man die beiden abbildenden Methoden AFM und cryo-TEM, findet man keinen starken Einfluss der Oberfläche auf die DNA-RPA-Wechselwirkung. Das Auftreten von Knicken bei UV-geschädigter DNA in den AFM-Experimenten [Lys02, Lys04], konnten nicht durch cryo-TEM-Untersuchungen bestätigt werden. Dies kann zwei Ursachen haben: Erstens können die Knicke in den AFM-Experimenten durch die Oberfläche hervorgerufen werden. Zweitens ist die Auflösung bei den TEM-Abbildungen nicht so gut wie in den AFM-Abbildungen, so dass die Knicke nicht beobachtbar sind.

Die Aussage der AFM-Experimente von M. Lysetska [Lys02, Lys04],

dass die DNA eine Schleife um das RPA bildet, konnte leider durch cryo-TEM-Messungen nicht bestätigt werden. Die Auflösung dieser Methode ist bei weitem nicht so gut wie in den AFM-Experimenten. Einfache TEM-Messungen könnten helfen, diese Frage zu beantworten, allerdings darf man dabei nicht vergessen, dass die Biomoleküle durch Kontrastfärben mit diversen Chemikalien in ihrer Struktur und daher in ihrer Funktion beeinflusst werden.

Statistische Aussagen über DNA-RPA-Komplexe aus den cryo-TEM Experimenten zu erhalten, so wie es in den AFM-Experimenten [Lys02, Lys04] durchgeführt worden ist, ist mit einem vertretbaren Aufwand nicht möglich. Für eine vernünftige Statistik sollten mindestens 100–200 Moleküle in mehreren Dimensionen abgebildet werden, was ein mehrfaches Verkippen der Probe bedeutet. Es müssten also mindestens 500–1000 Moleküle mit einer hinreichend hohen Auflösung abgebildet werden. In einem nächsten Schritt müssten die so erhaltenen Bilder mit einer geeigneten Software weiter ausgewertet werden (z. B. SPIDER [Fra81] oder IMAGIC5 [vH81, vH96]), um dreidimensionale Bilder zu erhalten.

Im letzten Teil dieser Arbeit wurden Untersuchungen mittels FCS und cryo-TEM zum Minichromosome-Maintenance-Protein durchgeführt. Es konnte gezeigt werden, dass dieses Protein eine Affinität zu Einzelstrang- und Doppelstrang-DNA besitzt. Die Struktur des DNA-Substrats spielt keine entscheidende Rolle, die Wechselwirkung war ähnlich für einfache dsDNA, Bubble-dsDNA oder dsDNA mit Einzelstrang-Überhängen. Die Forschungsarbeit zu MCM wird momentan fortgesetzt, um weitere Informationen zur Kinetik und zum Mechanismus der Helikase-Aktivität gewinnen zu können. Auch hier kann cryo-TEM zur Erstellung dreidimensionaler Bilder herangezogen werden, um die in der Literatur vorgeschlagene Struktur des Proteins [Pap03] im quasi-natürlichen Zustand zu bestätigen.

8 Bibliography

[Alb03] B. Alberts. *Nature*, **421**(6921), 431–435 (2003)

[Bat00] D. P. Batty and R. D. Wood. *Gene*, **241**(2), 193–204 (2000)

[Bec89] M. M. Becker and Z. Wang. *J. Mol. Biol.*, **210**(3), 429–438 (1989)

[Bel88] J. R. Bellare, H. T. Davis, L. E. Scriven, and Y. Talmon. *J. Electron. Micr. Tech.*, **10**(1), 87–111 (1988)

[Bel90] S. F. Bellon and S. J. Lippard. *Biophys. Chem.*, **35**(2-3), 179–188 (1990)

[Ben61] S. Benzer. *Proc. Natl. Acad. Sci. U. S. A.*, **47**, 403–416 (1961)

[Ben02] J. Benesch, A. Askendal, and P. Tengvall. *J. Colloid Interface Sci.*, **249**(1), 84–90 (2002)

[Ber94] R. J. W. Berg. *UV-induced damage in relation to skin cancer induction in hairless mice:implications for molecular dosimetryin man*. Ph.D. thesis, Universiteit Utrecht (1994)

[Bes97] T. Bessho, A. Sancar, L. H. Thompson, and M. P. Thelen. *J. Biol. Chem.*, **272**(6), 3833–3837 (1997)

[Beu60] R. Beukers and W. Berends. *Biochim. Biophys. Acta*, **41**(3), 550–551 (1960)

[Bia97] Biacore. *BIAevaluation 3.0 Software Handbook*. Biacore AB (1997)

8 Bibliography

[Bla94] L. J. Blackwell and J. A. Borowiec. *Mol. Cell. Biol.*, **14**(6), 3993–4001 (1994)

[Bla96] L. J. Blackwell, J. A. Borowiec, and I. A. Masrangelo. *Mol. Cell. Biol.*, **16**(9), 4798–4807 (1996)

[Boc97] A. Bochkarev, R. A. Pfuetzner, A. M. Edwards, and L. Frappier. *Nature*, **385**(6612), 176–181 (1997)

[Boc01] E. Bochkareva, V. Belegu, S. Korolev, and A. Bochkarev. *EMBO J.*, **20**(3), 612–618 (2001)

[Boc02] E. Bochkareva, S. Korolev, S. P. Lees-Miller, and A. Bochkarev. *EMBO J.*, **21**(7), 1855–1863 (2002)

[Boo98] D. Bootsma, K. H. Kraemer, J. Cleaver, and J. H. J. Hoeijmakers. In V. B and K. K. W, editors, "The Genetic Basis of Human Cancer", pp. 245–274. McGraw-Hill, New York (1998)

[Bos84] S. Bose and R. Davies. *Nucleic Acids Res.*, **12**(20), 7903 (1984)

[Bou87] F. Bourre, G. Renault, and A. Sarasin. *Nucleic Acids Res.*, **15**(21), 8861–8875 (1987)

[Bra88] D. E. Brash. *Photochem. Photobiol.*, **48**(1), 59–66 (1988)

[Bra97] K. Braun, Y. Lao, Z. He, C. Ingles, and M. Wold. *Biochemistry*, **36**(28), 8443–8454 (1997)

[Bri98] S. J. Brill and S. Bastin-Shanower. *Mol. Cell. Biol.*, **18**(12), 7225–7234 (1998)

[Buc01] M. Buckle. *Methods Mol. Biol.*, **148**, 535–546 (2001)

[Bur96] J. L. Burns, S. N. Guzder, P. Sung, S. Prakash, and L. Prakash. *J. Biol. Chem.*, **271**(20), 11607–11610 (1996)

[Cad92] J. Cadet, C. Anselmino, T. Douki, and L. Voituriez. *J. Photochem. Photobiol., B*, **15**(4), 277–298 (1992)

[Car02] F. Carpentieri, M. De Felice, M. De Falco, M. Rossi, and F. M. Pisani. *J. Biol. Chem.*, **277**(14), 12118–12127 (2002)

[Cho00] J. P. J. Chong, M. K. Hayashi, M. N. Simon, R. M. Xu, and B. Stillman. *Proc. Natl. Acad. Sci. U. S. A.*, **97**(4), 1530–1535 (2000)

[Chu01] Y. L. Chua, K. H. Pwee, R. M. Kini, C. Y. Leng, and P. K. Hock. *Plant Mol. Biol.*, **46**(2), 193–204 (2001)

[Cla92] T. M. Clausen, P. K. Vinson, J. R. Minter, H. T. Davis, Y. Talmon, and W. G. Miller. *J. Phys. Chem.*, **96**(1), 474–484 (1992)

[Cle88] J. E. Cleaver, F. Cortes, D. Karentz, L. H. Lutze, W. F. Morgan, A. N. Player, L. Vuksanovic, and D. L. Mitchell. *Photochem. Photobiol.*, **48**(1), 41–49 (1988)

[Dav03] M. J. Davey, C. Indiani, and M. O'Donnell. *J. Biol. Chem.*, **278**(7), 4491–4499 (2003)

[dL98] W. L. de Laat, E. Appeldoorn, K. Sugasawa, E. Weterings, N. G. Jaspers, and J. H. U. h.-J.-V. Hoeijmakers. *Genes Dev.*, **12**(16), 2598–2609 (1998)

[Eck01] C. Eckerich, F. O. Fackelmayer, and R. Knippers. *Biochim. Biophys. Acta*, **1538**(1), 67–75 (2001)

[Ede99] P. Edelmann, A. Esa, M. Hausmann, and C. Cremer. *Optik*, **110**(4), 194–198 (1999)

[Eig94] M. Eigen and R. Rigler. *Proc. Natl. Acad. Sci. U. S. A.*, **91**(13), 5740–5747 (1994)

[Els74] E. L. Elson and D. Magde. *Biopolymers*, **13**(1), 1–27 (1974)

8 Bibliography

[Esa00] A. Esa, P. Edelmann, G. Kreth, L. Trakhtenbrot, N. Amariglio, G. Rechavi, M. Hausmann, and C. Cremer. *J Microsc-Oxford*, **199**, 96–105 (2000)

[Fle03] R. J. Fletcher, B. E. Bishop, R. P. Leon, R. A. Sclafani, C. M. Ogata, and X. J. S. Chen. *Nat Struct Biol*, **10**(3), 160–167 (2003)

[Fol02] M. Folkard, K. M. Prise, C. J. Turner, and B. D. Michael. *Radiat. Prot. Dosim.*, **99**(1-4), 147–149 (2002)

[For04] S. L. Forsburg. *Microbiol. Mol. Biol. R.*, **68**(1), 109–+ (2004)

[Fra81] J. Frank, B. Shimkin, and H. Dowse. *Ultramicroscopy*, **6**(4), 343–357 (1981)

[Gal89] P. E. Gallagher and N. J. Duker. *Photochem Photobiol*, **49**(5), 599–605 (1989)

[Gas86] F. Gasparro and J. Fresco. *Nucleic Acids Res.*, **14**(10), 4239 (1986)

[Gom96] X. V. Gomes and M. S. Wold. *Biochemistry*, **35**(32), 10558–10568 (1996)

[Gra03] B. Grabowski and Z. Kelman. *Annu Rev Microbiol*, **57**, 487–516 (2003)

[Gra03a] I. Grainge, S. Scaife, and D. B. Wigley. *Nucleic Acids Res.*, **31**(16), 4888–4898 (2003)

[Gun96] D. Gunz, M. T. Hess, and H. Naegeli. *J. Biol. Chem.*, **271**(41), 25089–25098 (1996)

[He95] Z. He, L. A. Henricksen, M. S. Wold, and C. J. Ingles. *Nature*, **374**(6522), 566–569 (1995)

[Hey01] T. Hey, G. Lipps, and G. Krauss. *Biochemistry*, **40**(9), 2901–2910 (2001)

[Hey02] T. Hey. *Das Problem der Erkennung von DNA-Schäden bei der humanen Nukleotid-Exzisions-Reparatur.* Ph.D. thesis, University of Bayreuth (2002)

[Hän01] H. Hänsel. "Mathematica program for ellipsometric calculations" (2001)

[Hof84] J. H. v. Hoff. *Etudes de dynamique chimique.* Frederik Muller, Amsterdam (1884)

[Hor01] M. Horiguchi, K. Masumura, H. Ikehata, T. Ono, Y. Kanke, and T. Nohmi. *Cancer Res.*, **61**(10), 3913–3918 (2001)

[Hus88] I. Husain, J. Griffith, and A. Sancar. *Proc Natl Acad Sci U S A*, **85**(8), 2558–62 (1988)

[Ich03] M. Ichihashi, M. Ueda, A. Budiyanto, T. Bito, M. Oka, M. Fukunaga, K. Tsuru, and T. Horikawa. *Toxicology*, **189**(1-2), 21–39 (2003)

[Ima02] M. Imanishi and Y. Sugiura. *Biochemistry*, **41**(4), 1328–1334 (2002)

[Ish97] Y. Ishimi. *J. Biol. Chem.*, **272**(39), 24508–24513 (1997)

[Ish98] Y. Ishimi, Y. Komamura, Z. Y. You, and H. Kimura. *J. Biol. Chem.*, **273**(14), 8369–8375 (1998)

[Iti01] P. H. Itin, A. Sarasin, and M. R. Pittelkow. *J Am Acad Dermatol*, **44**(6), 891–920 (2001)

[Jun98] L. S. Jung, C. T. Campbell, T. M. Chinowsky, M. N. Mar, and S. S. Yee. *Langmuir*, **14**(19), 5636–5648 (1998)

[Kar91] R. Karlsson, A. Michaelsson, and L. Mattsson. *J. Immunol. Methods*, **145**(1-2), 229–240 (1991)

8 Bibliography

[Kas04] R. Kasiviswanathan, J. H. Shin, E. Melamud, and Z. Kelman. *J. Biol. Chem.*, **279**(27), 28358–28366 (2004)

[Kee96] P. J. Keeling, H. P. Klenk, R. K. Singh, O. Feeley, C. Schleper, W. Zillig, W. F. Doolittle, and C. W. Sensen. *Plasmid*, **35**(2), 141–144 (1996)

[Kel99] Z. Kelman, J. K. Lee, and J. Hurwitz. *Proc. Natl. Acad. Sci. U. S. A.*, **96**(26), 14783–14788 (1999)

[Kel03] L. M. Kelman and Z. Kelman. *Mol. Microbiol.*, **48**(3), 605–615 (2003)

[Ket98] U. Kettling, A. Koltermann, P. Schwille, and M. Eigen. *Proc. Natl. Acad. Sci. U. S. A.*, **95**(4), 1416–1420 (1998)

[Kim92] C. Kim, R. O. Snyder, and M. S. Wold. *Mol. Cell. Biol.*, **12**(7), 3050–3059 (1992)

[Kim94] C. Kim, B. F. Paulus, and M. S. Wold. *Biochemistry*, **33**(47), 14197–14206 (1994)

[Kim95] J. K. Kim and B. S. Choi. *Eur. J. Biochem.*, **228**(3), 849–854 (1995)

[Kol01] D. M. Kolpashchikov, S. N. Khodyreva, D. Y. Khlimankov, M. S. Wold, A. Favre, and O. I. Lavrik. *Nucleic Acids Res.*, **29**(2), 373–379 (2001)

[Kon04] M. Konorty. *Microstructural Aspects of Complexation between DNA and Positively Charged Colloids*. Master's thesis, Technion, Israel Institute of Technology (2004)

[Lab00] K. Labib, J. A. Tercero, and J. F. X. Diffley. *Science*, **288**(5471), 1643–1647 (2000)

[Lao99] Y. Lao, L. Chang Geun, and M. S. Wold. *Biochemistry*, **38**(13), 3974–3984 (1999)

[Lao00] Y. Lao, X. V. Gomes, Y. Ren, J. S. Taylor, and M. S. Wold. *Biochemistry*, **39**(5), 850–859 (2000)

[Lav99] O. Lavrik, D. Kolpashchikov, K. Weisshart, H.-P. Nasheuer, S. Khodyreva, and A. Favre. *Nucleic Acids Res.*, **27**(21), 4235–4240 (1999)

[Lee00] B.-S. Lee, L. Bi, D. Garfinkel, and A. U. h.-P.-J. Bailis. *Mol. Cell. Biol.*, **20**(7), 2436–2445 (2000)

[Lee00a] J. K. Lee and J. Hurwitz. *J. Biol. Chem.*, **275**(25), 18871–18878 (2000)

[Lee01] J. K. Lee and J. Hurwitz. *Proc. Natl. Acad. Sci. U. S. A.*, **98**(1), 54–59 (2001)

[Lip81] J. A. Lippke, L. K. Gordon, D. E. Brash, and W. A. Haseltine. *Proc Natl Acad Sci U S A* (1981)

[LP00] F. Le Page, E. E. Kwoh, A. Avrutskaya, A. Gentil, S. A. Leadon, A. Sarasin, and P. K. Cooper. *Cell (Cambridge, Mass.)*, **101**(2), 159–171 (2000)

[Lys02] M. Lysetska, A. Knoll, D. Boehringer, T. Hey, G. Krauss, and G. Krausch. *Nucleic Acids Res.*, **30**(12), 2686–2691 (2002)

[Lys04] M. Lysetska. *Intact and Damaged DNA and their Interaction with DNA-Binding Proteins: a Single Molecule Approach*. Ph.D. thesis, University of Bayreuth (2004)

[Mag72] D. Magde, W. W. Webb, and E. Elson. *Phys. Rev. Lett.*, **29**(11), 705–708 (1972)

[Mag74] D. Magde, E. L. Elson, and W. W. Webb. *Biopolymers*, **13**(1), 29–61 (1974)

8 Bibliography

[Mat95] T. Matsuda, M. Saijo, I. Kuraoka, T. Kobayashi, Y. Nakatsu, A. Nagai, T. Enjoji, C. Masutani, K. Sugasawa, and a. Hanaoka et. *J. Biol. Chem.*, **270**(8), 4152–4157 (1995)

[Mat96] T. Matsunaga, C. H. Park, T. Bessho, D. Mu, and A. Sancar. *J. Biol. Chem.*, **271**(19), 11047–11050 (1996)

[Mat02] Y. Matsumura and H. N. Ananthaswamy. *Front. Biosci.*, **7**, D765–D783 (2002)

[McC59] D. W. McCall, D. C. Douglass, and E. W. Anderson. *J. Chem. Phys.*, **31**(6), 1555–1557 (1959)

[Mit89] D. L. Mitchell and R. S. Nairn. *Photochem. Photobiol.*, **49**(6), 805–819 (1989)

[Mit93] P. G. Mitsis, S. C. Kowalczykowski, and I. R. Lehman. *Biochemistry*, **32**(19), 5257–5266 (1993)

[Mys99] D. G. Myszka. *J. Mol. Recognit.*, **12**(5), 279–284 (1999)

[Nag00] K. Nagata and H. Handa, editors. *Real-Time Analysis of Biomolecular Interactions*. Springer-Verlag, Tokyo (2000)

[Neu99] A. F. Neuwald, L. Aravind, J. L. Spouge, and E. V. Koonin. *Genome Res*, **9**(1), 27–43 (1999)

[O'S93] D. J. O'Shannessy, M. Brigham-Burke, K. K. Soneson, P. Hensley, and I. Brooks. *Anal. Biochem.*, **212**(2), 457–468 (1993)

[Pap03] T. Pape, H. Meka, S. X. Chen, G. Vicentini, M. van Heel, and S. Onesti. *Embo. Rep.*, **4**(11), 1079–1083 (2003)

[Par94] C. N. Parris, D. D. Levy, J. Jessee, and M. M. Seidman. *J. Mol. Biol.*, **236**(2), 491–502 (1994)

[Pat99] S. M. Patrick and J. J. Turchi. *J. Biol. Chem.*, **274**(21), 14972–14978 (1999)

[Phi96] D. Philipova, J. R. Mullen, H. S. Maniar, J. Lu, C. Gu, and S. J. Brill. *Genes Dev.*, **10**(17), 2222–2233 (1996)

[Pop01] A. Poplawski, B. Grabowski, S. F. Long, and Z. Kelman. *J. Biol. Chem.*, **276**(52), 49371–49377 (2001)

[Puc04] B. Pucci, M. De Felice, M. Rossi, S. Onesti, and F. M. Pisani. *J. Biol. Chem.*, **279**(47), 49222–49228 (2004)

[Rüf02] A. Rüfer, P. F. Neuenschwander, and B. Sauer. *Anal. Biochem.*, **308**(1), 90–99 (2002)

[Ric89] J. Ricka and T. Binkert. *Phys. Rev. A*, **39**(5), 2646–2652 (1989)

[Rig98] R. Rigler, Z. Foldes-Papp, F. J. Meyer-Almes, C. Sammet, M. Volcker, and A. Schnetz. *J. Biotechnol.*, **63**(2), 97–109 (1998)

[Riv98] C. Rivetti, C. Walker, and C. Bustamante. *J. Mol. Biol.*, **280**(1), 41–59 (1998)

[Roo98] H. Roos, R. Karlsson, H. Nilshans, and A. Persson. *J. Mol. Recognit.*, **11**(1-6), 204–210 (1998)

[Ryc85] R. E. Rycyna and J. L. Alderfer. *Nucleic Acids Res*, **13**(16), 5949–5963 (1985)

[San96] A. Sancar. *Annu. Rev. Biochem.*, **65**, 43–81 (1996)

[Sar97] A. Sarasin and A. Stary. *Cancer Detect. Prev.*, **21**(5), 406–411 (1997)

[Sat00] M. Sato, T. Gotow, Z. Y. You, Y. Komamura-Kohno, Y. Uchiyama, N. Yabuta, H. Nojima, and Y. Ishimi. *J. Mol. Biol.*, **300**(3), 421–431 (2000)

[Sch97] P. Schwille, F. J. MeyerAlmes, and R. Rigler. *Biophys. J.*, **72**(4), 1878–1886 (1997)

8 Bibliography

[Sch99] U. Schweizer, T. Hey, G. Lipps, and G. Krauss. *Nucleic Acids Res.*, **27**(15), 3183–3189 (1999)

[Sch01] A. Schwacha and S. P. Bell. *Mol Cell*, **8**(5), 1093–1104 (2001)

[Sch01a] P. Schwille and U. Kettling. *Curr. Opin. Biotechnol.*, **12**(4), 382–386 (2001)

[Sch03] F. Schubert, H. Zettl, W. Hafner, G. Krauss, and G. Krausch. *Biochemistry*, **42**(34), 10288–10294 (2003)

[Sei96] M. Seimiya and Y. Kurosawa. *FEBS Lett.*, **398**(2-3), 279–284 (1996)

[She00] D. F. Shechter, C. Y. Ying, and J. Gautier. *J. Biol. Chem.*, **275**(20), 15049–15059 (2000)

[Shi03] J. H. Shin, Y. Jiang, B. Grabowski, J. Hurwitz, and Z. Kelman. *J. Biol. Chem.*, **278**(49), 49053–49062 (2003)

[Smi93] C. A. Smith and J. S. Taylor. *J. Biol. Chem.*, **268**(15), 11143–11151 (1993)

[Spi88] G. Spivak, S. A. Leadon, J. M. Vos, S. Meade, P. C. Hanawalt, and A. K. Ganesan. *Mutat. Res.*, **193**(2), 97–108 (1988)

[Tal83] Y. Talmon. *J. Colloid Interface Sci.*, **93**(2), 366–382 (1983)

[Tal87] Y. Talmon. In R. A. Steinbrecht and K. Zierold, editors, "Cryotechniques in Biological Electron Microscopy", Springer Verlag, Berlin (1987)

[Tal96] Y. Talmon. *Ber Bunsen Phys Chem*, **100**(3), 364–372 (1996)

[Tal96a] Y. Talmon and H. Mohwald. *Curr Opin Colloid In*, **1**(2), 241–242 (1996)

[Tal99] Y. Talmon. In B. T. Binks, editor, "Modern Characterization Methods of Surfactant Systems", pp. 147–176. Marcel Dekker, New York (1999)

[Tay90] J.-S. Taylor, D. Garrett, I. Brockie, D. Svoboda, and J. Telser. *Biochemistry*, **29**(37), 8858–8866 (1990)

[Thö97] P. Thömmes, Y. Kubota, H. Takisawa, and J. J. Blow. *EMBO J.*, **16**(11), 3312–3319 (1997)

[Tho03] B. S. Thoma and K. M. Vasquez. *Mol Carcinogen*, **38**(1), 1–13 (2003)

[Tir84] M. M. Tirado, C. L. Martinez, and J. G. Delatorre. *J. Chem. Phys.*, **81**(4), 2047–2052 (1984)

[Tre96] K. Treuner, U. Ramsperger, and R. Knippers. *J. Mol. Biol.*, **259**(1), 104–112 (1996)

[Tye99] B. K. Tye. *Annu. Rev. Biochem.*, **68**, 649–686 (1999)

[Vas02] K. M. Vasquez, J. Christensen, L. Li, R. A. Finch, and P. M. Glazer. *Proc. Natl. Acad. Sci. U. S. A.*, **99**(9), 5848–5853 (2002)

[vH81] M. van Heel and W. Keegstra. *Ultramicroscopy*, **7**(2), 113–130 (1981)

[vH96] M. van Heel, G. Harauz, E. V. Orlova, R. Schmidt, and M. Schatz. *J. Struct. Biol.*, **116**(1), 17–24 (1996)

[Wan76] S. Y. Wang. *Photochemistry and Photobiology of Nucleic Acids*. Academic Press, New York (1976)

[Wan00] M. Wang, A. Mahrenholz, and S. H. Lee. *Biochemistry*, **39**(21), 6433–6439 (2000)

[Wat53] J. D. Watson and F. H. C. Crick. *Nature*, **171**, 737–8 (1953)

8 Bibliography

[Wei02] T. Weidemann, M. Wachsmuth, M. Tewes, K. Rippe, and J. Langowski. *Single Mol*, **3**(1), 49–61 (2002)

[Wid95] J. Widengren, U. Mets, and R. Rigler. *J. Phys. Chem.*, **99**(36), 13368–13379 (1995)

[Wid00] J. Widengren and P. Schwille. *J. Phys. Chem. A*, **104**(27), 6416–6428 (2000)

[Wil96] D. B. Williams and C. B. Carter. *Transmission Electron Microscopy: A Textbook for Material Science*. Plenum Press, New York (1996)

[Wol97] M. S. Wold. *Annu. Rev. Biochem.*, **66**, 61–92 (1997)

[Woo99] R. D. Wood. *Biochimie*, **81**(1-2), 39–44 (1999)

[Woo00] R. Wood, S. Araujo, R. Ariza, D. Batty, M. Biggerstaff, E. Evans, P.-H. Gaillard, D. Gunz, B. Koberle, I. Kuraoka, J. Moggs, J. Sandall, and M. U. h.-C.-S. Shivji. *Cold Spring Harbor Symp. Quant. Biol.*, **65**, 173–182 (2000)

[Yab03] N. Yabuta, N. Kajimura, K. Mayanagi, M. Sato, T. Gotow, Y. Uchiyama, Y. Ishimi, and H. Nojima. *Genes Cells*, **8**(5), 413–421 (2003)

[Yan02] W. Yang, W. Zeng, D. Zhou, and Y. Shi. *Biochim. Biophys. Acta Protein Struct. Mol. Enzymol.*, **1598**(1-2), 147–155 (2002)

[You99] Z. Y. You, Y. Komamura, and Y. Ishimi. *Mol. Cell. Biol.*, **19**(12), 8003–8015 (1999)

[You03] J. S. You, M. Wang, and S. H. Lee. *J. Biol. Chem.*, **278**(9), 7476–7485 (2003)

[Yu02] X. Yu, M. S. VanLoock, A. Poplawski, Z. Kelman, T. Xiang, B. K. Tye, and E. H. Egelman. *Embo. Rep.*, **3**(8), 792–797 (2002)

[Zei01] Zeiss. *Confocor 2 Applications Handbook*. Carl Zeiss, Advanced Imaging Microscopy, Jena (2001)

[Zet01] H. Zettl. "LabView program for FCS analysis" (2001)

[Zet02] H. Zettl. "Setup for temperature dependent FCS measurements" (2002)

8 Bibliography

Danksagung

Das Gelingen dieser Arbeit wäre ohne das passende Umfeld mit vielen hilfsbereiten Personen nicht möglich gewesen. Mein besonderer Dank gebührt:

Prof. Georg Krausch, der es mir ermöglichte, ein interessantes und interdisziplinäres Thema in seinem Arbeitskreis zu bearbeiten. Seine zahlreichen Ratschläge und sein Optimismus waren eine große Unterstützung. Besonders möchte ich ihm danken für die Freiräume, die er mir gelassen hat, um eigene Ideen umzusetzen.

Prof. Gerhard Krauss für das Wagnis, mit mir eine schon bestehende fruchtbare Kooperation zwischen Biochemie und Physikalischer Chemie II fortzusetzen.

Prof. Ishi Talmon, der mich in die Geheimnisse der cryo-Transmissionselektronenmikroskopie einweihte und mir die Möglichkeit gab, in seiner Arbeitsgruppe in Haifa zu arbeiten.

Prof. Franz Xaver Schmid für die Übernahme des Koreferats.

Dr. Georg Lipps für die Möglichkeit, biochemische Experimente in seinem Labor durchführen und Diskussionen über die Ergebnisse führen zu können.

Dr. Markus Drechsler, mit dem ich stundenlang am TEM auf der Suche nach DNA und Proteinen war, für seine Geduld mit mir und meinen Pro-

ben.

Dr. Jörg Enderlein für die FCS-Berechnungen, die mir gezeigt haben, dass FCS-Experimente durch viele kleine Details stark beeinflusst werden.

Ganz besonderer Dank gilt der Arbeitsgruppe PC II für das sehr anregende und zuweilen unterhaltsame Arbeitsklima:

Dr. Wolfgang Häfner für seine Hilfe und Diskussionsfreudigkeit bei mathematischen, physikalischen und TEXnischen Problemen. Weiterhin gebührt ihm mein Dank für die Einführung in die Lehrtätigkeit.

Heiko Zettl, dem Mann mit den magischen Fingern, für die großartige Hilfe bei allen FCS-Experimenten. Häufig hatte er die zündende Idee, ein Problem zu lösen. Ganz nebenbei: die Organisation des Laborbestands und der Kaffeekasse war auch seine Aufgabe.

Kristin Schmidt, die mir durch viele gemeinsame Stunden, sei es in Grenoble oder beim Tanzen, eine sehr gute Freundin geworden ist. Ich konnte viele wissenschaftliche und nicht-wissenschaftliche Themen mit ihr diskutieren.

Dr. Helmut Hänsel für seine Hilfsbereitschaft und Diskussionsbereitschaft besonders in programmiertechnischer und theoretischer Hinsicht. Außerdem habe ich durch ihn eine sehr gute Einführung in die Systemadministrator-Tätigkeit erhalten.

Alexandra Sperschneider für ihren unermüdlichen Einsatz am FCS, AFM und TEM und in der Biochemie. Um meine Nachfolge im Bereich Biologische Systeme am Lehrstuhl muss ich mir wohl keine Gedanken machen. Weiter so!

Dr. Alexander Böker für die immer sehr unterhaltsamen langen Wochenenden in Grenoble. Ich habe dadurch viele neue und interessante Einblicke

in einen völlig anderen Forschungsbereich erhalten.

Dr. Arnaud Chiche, unserem frischen Franzosen, für die Gelegenheit, kritisch über die deutsche Sprache nachzudenken.

Dr. Marina Lysetska für ihre Unterstützung während meiner Anfangszeit am Lehrstuhl PC II und ihre Hilfe und Diskussionsbereitschaft bei meinen Fragen zu den Themen DNA und RPA.

Dr. Rasa Beinoraviciute-Kellner für ihre Hilfe bei vielen biochemischen Fragen. Die zahlreichen Diskussionen haben mir zu Beginn meiner Arbeit in Bayreuth einen tiefen Einblick in die Biochemie gegeben.

Und natürlich allen anderen, auch ehemaligen, Mitgliedern der PC II-Arbeitsgruppe: Michaela Hoffmann, Andriana Horvat, Sven Hüttner, Markus Hund, Günther Jutz, Dr. Armin Knoll, Sergej Koutouzov, Martin Kreis, Carmen Kunert, Ute Lippert, Sabine Ludwigs, Robert Magerle, Sabine Marr, Violetta Olszowka, Dr. Nicolaus Rehse, Gustav Sauer, John Bosco Stanislaus, Dr. Larisa Tsarkova, Dr. Andrej Voronov, Dr. Chun Wang, Dr. Denys Zimin für die gute Zusammenarbeit.

Ein ganz besonderer Dank gilt Sybille Zimmermann für die Hilfsbereitschaft in bürokratischen und organisatorischen Belangen sowie für die gute Versorgung mit Nervennahrung.

Meiner Familie danke ich für die große Unterstützung während des Studiums und der Promotion.

Erklärung

Die vorliegende Arbeit wurde von mir selbstständig verfasst, und ich habe dabei keine anderen als die angegebenen Hilfsmittel und Quellen benutzt.

Ferner habe ich nicht versucht, anderweitig mit oder ohne Erfolg eine Dissertation einzureichen oder mich der Doktorprüfung zu unterziehen.

Bayreuth, 13. April 2005

Frank Schubert